Electronic Thesis and Dissertation Repository

4-24-2013 12:00 AM

Robotics-Assisted Needle Steering for Percutaneous Interventions: Modeling and Experiments

Ali Asadian
The University of Western Ontario

Supervisor
Dr. Rajni V. Patel
The University of Western Ontario Joint Supervisor
Dr. Mehrdad R. Kermani
The University of Western Ontario

© Ali Asadian 2013

Recommended Citation

Robotics-Assisted Needle Steering for Percutaneous Interventions: Modeling and Experiments

(Thesis Format: Integrated Article)

by

Ali <u>Asadian</u>

Graduate Program in Engineering Science
Department of Electrical and Computer Engineering

A thesis submitted in partial fulfillment
of the requirements for the degree of
Doctor of philosophy

The School of Graduate and Postdoctoral Studies
Western University (The University of Western Ontario)
London, Ontario, Canada

Abstract

Needle insertion and guidance plays an important role in medical procedures such as brachytherapy and biopsy. Flexible needles have the potential to facilitate precise targeting and avoid collisions during medical interventions while reducing trauma to the patient and post-puncture issues. Nevertheless, error introduced during guidance degrades the effectiveness of the planned therapy or diagnosis. Although steering using flexible bevel-tip needles provides great mobility and dexterity, a major barrier is the complexity of needle-tissue interaction that does not lend itself to intuitive control. To overcome this problem, a robotic system can be employed to perform trajectory planning and tracking by manipulation of the needle base.

This research project focuses on a control-theoretic approach and draws on the rich literature from control and systems theory to model needle-tissue interaction and needle flexion and then design a robotics-based strategy for needle insertion/steering. The resulting solutions will directly benefit a wide range of needle-based interventions. The outcome of this computer-assisted approach will not only enable us to perform efficient preoperative trajectory planning, but will also provide more insight into needle-tissue interaction that will be helpful in developing advanced intraoperative algorithms for needle steering.

Experimental validation of the proposed methodologies was carried out on a state of-the-art 5-DOF robotic system designed and constructed in-house primarily for prostate brachytherapy. The system is equipped with a Nano43 6-DOF force/torque sensor (ATI Industrial Automation) to measure forces and torques acting on the needle shaft. In our setup, an Aurora electromagnetic tracker (Northern Digital Inc.) is the sensing device used for measuring needle deflection. A multi-threaded application for control, sensor readings, data logging and communication over the ethernet was developed using Microsoft® Visual C 2005, MATLAB® 2007 and the QuaRC® Toolbox (Quanser Inc.). Various artificial phantoms were developed so as to create a realistic medium in terms of elasticity and insertion force ranges; however, they simulated a uniform environment without exhibiting complexities of organic tissues. Experiments were also conducted on beef liver and fresh chicken breast, beef, and ham, to investigate the behavior of a variety biological tissues.

KEYWORDS: Robotics-Assisted Needle Insertion, Needle-Tissue Interaction, Needle-Tissue Friction, Needle Steering, Needle Deflection, Percutaneous Interventions, Computer-Assisted Surgery.

Co-Authorship Statement

The thesis presented here has been written by Ali Asadian under supervision of Dr. Rajni V. Patel and Dr. Mehrdad R. Kermani. Part of the materials in this thesis have been published in peer-reviewed journal papers and refereed conference proceedings, or are under review for publication. The research published in each paper has been conducted by the principal author, and guided and supported by the co-authors who are the research supervisors.

The material presented in chapter 2 has been published in

- Ali Asadian, Mehrdad R. Kermani, and Rajni V. Patel, "A Novel Force Modeling Scheme for Needle Insertion Using Multiple Kalman Filters," IEEE Transactions on Instrumentation and Measurement, vol. 61, no. 2, 2012, pp. 429-438.

- Ali Asadian, Mehrdad R. Kermani, and Rajni V. Patel, "A Compact Dynamic Force Model for Needle-Tissue Interaction," In Proceeding of the 32nd Annual International Conference of IEEE Engineering in Medicine and Biology Society (EMBS), pp. 2292-2295, Argentina, 2010.

The material presented in chapter 3 is currently under peer review for publication in

- Ali Asadian, Rajni V. Patel, and Mehrdad R. Kermani, "Dynamics of Translational Friction in Needle-Tissue Interaction During Needle Insertion," Submitted to the Annals in Biomedical Engineering (Springer Verlag), 2013.

This work has been published in part in

- Ali Asadian, Rajni V. Patel, and Mehrdad R. Kermani, "A Distributed Model for Needle-Tissue Friction in Percutaneous Interventions," In Proceeding of IEEE International Conference on Robotics and Automation (ICRA), pp. 1896-1901, China, 2011.

The material presented in chapter 4 has been published in

- Ali Asadian, Rajni V. Patel, and Mehrdad R. Kermani, "Compensation for Relative Velocity between Needle and Soft Tissue for Friction Modeling in Needle Insertion," In Proceeding of the 34th Annual International Conference of IEEE Engineering in Medicine and Biology Society (EMBS), pp. 960-963, USA, 2012.

The material presented in chapter 5 has been published in

- Ali Asadian, Mehrdad R. Kermani, and Rajni V. Patel, "An Analytical Model for Deflection of Flexible Needles During Needle Insertion," In Proceeding of IEEE/RSJ International Conference on Intelligent Robots and Systems (IROS), pp. 2551-2556, USA, 2011.

The material presented in chapter 6 has been published in

- Ali Asadian, Mehrdad R. Kermani, and Rajni V. Patel, "Robot-Assisted Needle Steering Using a Control Theoretic Approach," Journal of Intelligent and Robotic Systems (Springer Verlag), vol. 62, no. 3-4, 2011, pp. 397-418.

- Ali Asadian, Mehrdad R. Kermani, and Rajni V. Patel, "Accelerated Needle Steering Using Partitioned Value Iteration," In Proceeding of IEEE American Control Conference (ACC), pp. 2785-2790, USA, 2010.

Acknowledgement

First and foremost, I wish to express my sincere gratitude and appreciation to my supervisors Dr. Rajni Patel and Dr. Mehrdad R. Kermani for giving me the opportunity to accomplish this project at CSTAR. I would like to thank them for their patience, encouragement, and constructive advices during my PhD studies. They have always been understanding of my situation and compassionate to me during the ups and downs of my life in the past few years. I would also appreciate the time and efforts spent by the members of the examining committee, Dr. Kenneth A. McIsaac, Dr. Ilia Polushin, and Dr. Shaun Salisbury as well as Dr. Gabor Fichtinger as the external examiner.

Special thanks to my dear friend Dr. Ali Talasaz for his continuous companionship and help during my stay in London. My gratitude goes to all the past and present members of CSTAR, especially Dr. Harman Bassan, Dr. Mahdi Azizian, Chris Ward and Abelardo Escoto for their technical assistance in the beginning of this project. Sincere thanks also belongs to my wonderful friends at Western, Mahta, Mahya, Farrokh, Mostafa, Iman, Amir, Mohsen, Nima, Sahar, Maysam and my close friend, Peyman, for encouraging me and making me feel welcome all the time.

I would like to thank Afrooz. Although we are not together now, I will never forget your support and your struggle against the hardships in the past. Above all, I am grateful to a special and dear friend, Mahnoosh, who triggered me to stand up and be back to myself.

Last but by no means least, I am thankful to my kind parents and sisters who means a lot to me. My parents provided me unconditional care and support since my childhood, and I am deeply indebted to them and love them from the bottom of my heart.

Table of Contents

List of Tables

List of Figures

Nomenclature

2D	2 Dimensional
3D	3 Dimensional
BMI	Body Mass Index
CAMI	Computer-Assisted Medical Interventions
CCD	Charge-Coupled Device
CIHR	Canadian Institutes of Health Research
CMOS	Complementary Metal Oxide Semiconductor
CPU	Central Processor Unit
CREATE	Collaborative Research and Training Experience
CSTAR	Canadian Surgical Technologies and Advanced Robotics
CT	Computed Tomography
CVS	Chorionic Villus Sampling
DOF	Degree of Freedom
DP	Dynamic Programming
DRE	Digital Rectal Exam
EBRT	External Beam Radiation Therapy
EKF	Extended Kalman Filtering
EM	Electromagnetic
FEM	Finite Element Method
GUI	Graphical User Interface
HDR	High-Dose Rate
KV	Kelvin-Voigt
LDR	Low-Dose Rate
LSBP	Linear Segments with Parabolic Blends
LuGre	Lund-Grenoble

MATLAB	MATrix LABoratory
MDP	Markov Decision Process
MIS	Minimally Invasive Surgery
MR	Magnetic Resonance
MRI	Magnetic Resonance Imaging
NSERC	Natural Sciences and Engineering Research Council
ODE	Ordinary Differential Equations
PDE	Partial Differential Equation
PDP	Partition Dependents of a Partition
PDS	Partition Dependents of a State
PDPH	Post-Dural Puncture Headache
PC	Personal Computer
PID	Proportional Integral Derivative
PIF	Potential Information Flow
PMP	Pontryagin's Maximum Principle
PPVI	Prioritized-Partitioned Value Iteration
PSA	Prostate-Specific Antigen
PVC	Polyvinyl Chloride
QuaRC	Quanser Real-Time Control
RAM	Random Access Memory
RCM	Remote Center of Motion
RF	Radio Frequency
RMS	Root Mean Squared
RMSE	Root Mean Squared Error
RP	Radical Prostatectomy
RRT	Rapidly Random Tree
SDP	State Dependents of a Partition
SDS	State Dependents of a State
SMR	Stochastic Motion Roadmap
STD	Standard Deviation
TRUS	Transrectal Ultrasound
UDP	User Datagram Protocol
US	Ultrasound

Chapter 1

Introduction

1.1 Minimally Invasive Surgery

Minimally Invasive Surgery (MIS), or Laparoscopic Surgery is a modern technique in which operations are performed through small incisions (0.5-1.5cm). This procedure does not require the surgeon to make a large incision as required by traditional open surgery. There are a number of advantages to the patient with laparoscopic surgery versus an open procedure:

- Less postoperative pain
- Less blood loss during surgery
- Shorter hospital stay
- Smaller and less visible scars
- Faster recovery
- Fewer risks such as infection and incisional hernias compared with traditional open surgery

Laparoscopic MIS involves the use of long slender instruments and a camera (called an endoscope) introduced into the body through small incisions about 1cm across to view and perform surgery in the abdominal and pelvic areas as shown in Fig. 1.1. During this procedure, the surgeon makes several small incisions about 1cm in length at the site of the surgery. The surgeon then inserts specially designed plastic tubes (called trocars), through

Figure 1.1: Minimally invasive surgery using laparoscopic instruments [1].

which the laparoscope and surgical instruments are introduced. The endoscope transmits live video images of the patient's organs to a high-definition monitor which allows the surgeon to successfully operate without the use of large incisions.

While laparoscopic surgery is clearly beneficial in terms of patient outcomes, the procedure is more difficult from the surgeon's perspective in contrast to traditional open surgery in the following sense:

- The surgeon has limited range of motion at the surgical site resulting in a loss of dexterity.

- Depth perception is poor while no three-dimensional (3D) visualization is available.

- Surgeons must use hand-held tools or robotic instruments to interact with tissue rather than manipulation directly with their hands. In the absence of force reflection which is the case in many situations, this results in an inability to accurately judge how much force is being applied to tissue as well as a risk of damaging tissue by applying excessive force or pressure. This limitation also reduces tactile sensation, making it more difficult for the surgeon to feel tissue and thereby turning a delicate operation such as tying sutures into a complicated task.

- The tool endpoints move in the opposite direction to the surgeon's hands due to the pivot point making laparoscopic surgery a non-intuitive motor skill that is not very straightforward to learn.

1.2 Needle-based Interventions

Medical intervention using surgical needles is a common minimally invasive procedure. Many forms of routine treatment and diagnosis employed in modern clinical practice involve percutaneous insertion of a needle to place the tip of the needle safely and accurately in a lesion, organ, or vessel. By accuracy of tip placement, we mean the degree of closeness of its actual or true value to the measured quantity. This notion is distinct from precision (also called repeatability) that is associated with the degree to which repeated measurements under unchanged conditions generate the same results.

The placement for percutaneous intervention is usually performed using a straight-line trajectory primarily due to the absence of sufficient feedback and the lack of the ability for steering the needle. In manual prostate brachytherapy, one hand advances the needle through a rigid template in a visual-servo-based fashion. If the needle fails to reach its goal, then it must be retracted and reinserted, and several attempts may be required before precise placement is achieved. In many procedures, the precision of diagnosis or effectiveness of therapy is limited by the amount of steering that can be done once the needle is inserted, and usually, the needle divergence from its desired path degrades the effectiveness of the diagnosis or treatment. It has also been reported that needle misplacement may be due to imaging limitations, image misalignments, target uncertainty, target movement, and human errors [2]. Thus, more caution is required to avoid any damage or spread of a disease which in turn may lead to subsequent complications.

Recent advances in all areas of medicine and technology provides alternatives to regular rigid needles and conventional intervention methods. Facilitating curved trajectories, flexible needles can be utilized for localized drug delivery, radioactive seed placement or brachytherapy, ablation, neurosurgery, deep brain stimulation, and tissue biopsy especially in dealing with deep zones or target points that are difficult to access. Therefore, **robotics-assisted needle steering**, which is intended to guide the needle to specific targets inside soft tissue, has become an active research area.

Thinner needles cause less damage, trauma and morbidity to the tissue; for instance, they reduce the chance of Post-Dural Puncture Headache (PDPH) in case of spinal anesthesia. As another example, during a C-arm guided operation, the surgeon is not necessarily exposed to X-ray radiation. But, it should be noted that a major obstacle to using thin flexible needles is that, although they have greater mobility than straight rigid needles, they are very
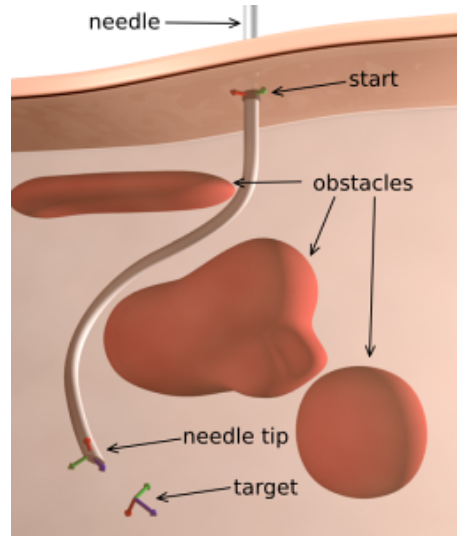
Figure 1.2: A steerable needle setup in 3D [50] (© Copyright 2010, IEEE).

difficult to control and do not lend themselves to intuitive steering. To this end, a robot can be used to control a bevel-tip flexible needle inside soft tissue. Fig. 1.2 depicts the concept of steering and obstacle avoidance using a flexible needle.

The desired trajectory for the needle tip is planned such that it does not penetrate delicate structures for example nerves and blood vessels or collide with bones, which might lie between feasible entry points and potential targets. From this point of view, a flexible needle can be utilized to hit target points in areas where there is (1) no direct visibility; (2) no direct access (deep zones), or (3) no room to maneuver. Generally speaking, targeting inaccuracy stems from a variety of complex factors including (1) organ deformation; (2) asymmetric needle bending as a result of needle-tissue interaction forces; (3) inhomogeneity, nonlinear viscoelasticity, and anisotropy of real tissue; (4) target movement due to respiration, heartbeat or similar artifacts, and (5) small anatomic structures that cannot be easily identified with common imaging modalities, such as Ultrasound (US), Computed Tomography (CT) or Magnetic Resonance Imaging (MRI).

In case of percutaneous interventions, a thorough understanding of the interaction between the needle and living tissue is a complex task [3, 4]. Discussion and review of the technical details are left to section 1.4. Indeed, environmental features including soft tissue dynamics are important to design the robotics-assisted control strategy [5, 6], and characterization of needle-tissue interaction remains challenging for the following reasons:

- The layers crossed by the needle, e.g., skin, fat, muscles, and organs, are inhomo-

geneous; so mechanical properties of each layer cannot be described by constant parameters.

- The parameter values are patient-dependent, and are linked to a particular needle type or geometry. Mechanical properties also depend on age and gender, and vary between healthy, damaged and diseased tissues.

- When the needle is inserted into a body, the elementary contributions of the various tissues are intermixed.

- Since the needle penetrates various types of tissue, the interaction is expected to be nonlinear.

Therefore, finding a general solution to the problem of needle steering is very complex. It is not yet apparent how best to transfer engineering skills and theoretical concepts into clinical practice, as it will certainly depend on the application. To integrate engineering and clinical knowledge, the critical questions that have to be answered are as follows [24]:

- What are the sources of motion artifacts, and to what extent are they predictable?

- How is the needle guided, and is it possible to make fine adjustments at the needle base or near the point of entry intraoperatively?

- What is the desired placement accuracy, and what are the risks of misplacement?

- Is high-resolution real-time intraoperative imaging available, or are only preoperative images available for the procedure?

- Is it possible to have pre-planning using *a priori* information?

Clinically, the prostate, liver, and brain provide specific examples of human organs where treatments may be improved by the use of fine needle-based procedures. However, diagnosis or treatment of prostate cancer has been historically the main and first application of robotics-assisted systems in needle-based interventions, so it is reviewed as a relevant case study in the next section.

1.3 Prostate Brachytherapy: The Initial Motivation for Robotics-Assisted Needle Insertion

1.3.1 Prostate Cancer: Medical Issues and Limitations

Prostate cancer strikes one in six men. Similar to many other types of cancer, it is curable when it is diagnosed at an early stage. This cancer is the second leading cause of cancer-related deaths in men, with lung cancer being the most common, and colon cancer closely following prostate cancer. Recently, its mortality has declined to a great extent, and the 5-year survival rate has seen a large increase mainly due to: (1) primary screening; (2) early detection, and (3) changes in lifestyle.

Fig. 1.3 depicts the anatomy of the prostate gland, and associated stages of cancer spread [7]. As prostate cancer progresses from Stage I to Stage IV, cancer cells grow within the prostate, through the outer layer of the prostate into nearby tissue, and then to lymph nodes or other parts of the body. Current clinical diagnostic routines for this cancer include:

1. **Digital Rectal Exam** (DRE)

2. **Prostate-Specific Antigen** (PSA)

3. **Transrectal Ultrasound** (TRUS) guided biopsy that may still miss the cancer

Despite its limitations and producing a high rate of false negative and false positive results, PSA is the most common test for prostate cancer diagnosis. PSA increase is the first sign of local recurrence or distant nodal/osseous metastases after surgery or radiation therapy. However, several clinical dilemmas remain, and alterations in PSA levels do not necessarily correlate with the clinical status. Men with serum PSA levels exceeding 2.5ng/mL have a greater than 20% chance of having cancerous prostate detected by needle biopsy, whereas more than 50% of men with a PSA level higher than 10.0ng/mL have cancer. Likewise, statistical analysis proves that 70% to 80% of men with abnormal findings on a PSA test (>4.0ng/mL) do not have cancer. Prostate biopsies using Gleason score is the next option as the best prognostic indicator that is the outcome of examination of histologic specimens from the prostate gland. But, up to 28% of clinically significant cancers have been reported to remain undetected by the traditional TRUS, and nearly 20% of men with biopsy-proven cancer have PSA values in the normal range (<4.0ng/mL) [10].
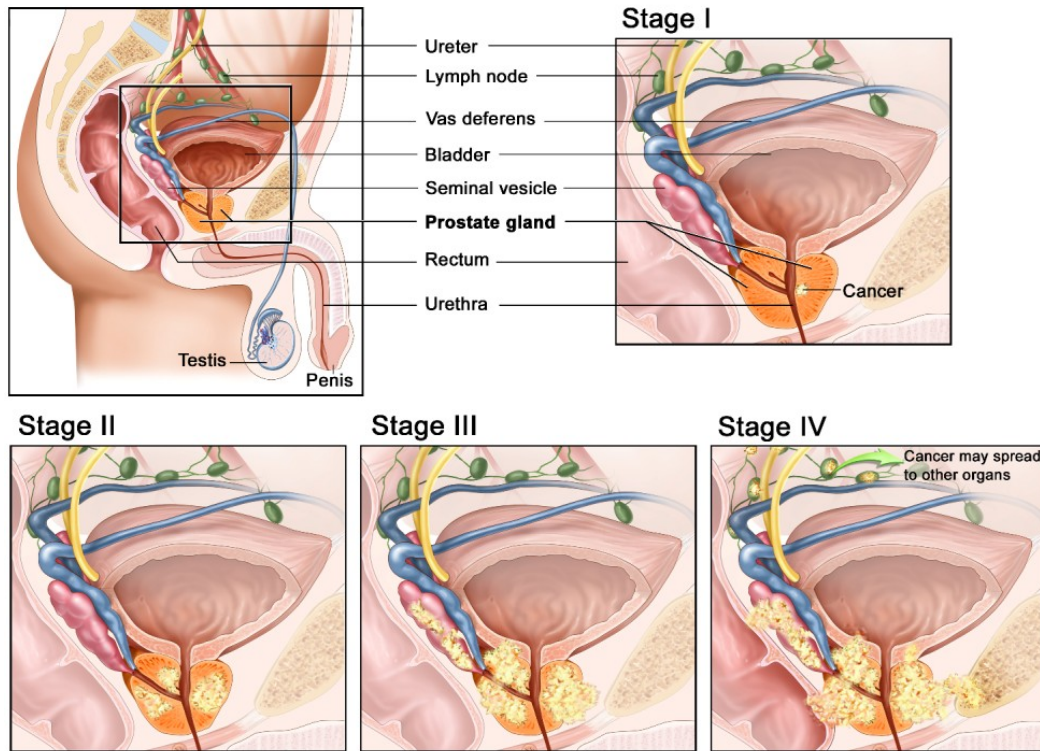
Figure 1.3: Anatomy of the prostate and staging of prostate cancer [7].

In Stage I, cancer is found only in the prostate. PSA level and the Gleason score are lower than 10 and 6, respectively and the cancer cannot be felt by DRE. In Stage II, prostate cancer is more advanced than in Stage I, but it is not yet spread outside the prostate gland. During Stage III, it spreads beyond the outer layer of the prostate on one or both sides and may have spread to the seminal vesicles. The PSA can have any level and the Gleason score from 2 to 10. Finally, in Stage IV, the cancer spreads beyond the seminal vesicles to adjacent organs such as the rectum, urethral sphincter, bladder, or pelvic wall. It may also contaminate distant parts of the body including lymph nodes or bones.

Note that initial diagnosis and staging of this cancer using medical routines is still challenging; however, it is a slow-growing disease. Currently, overdiagnosis of indolent disease rates is estimated to be between 27% and 56%, and overtreatment costs an estimated annual 3 billion dollars in the USA for example [10]. It is obvious that increased understanding of the early detection of local and distant recurrences leads to more accurate assessment and better treatment selection for patients. Briefly, current treatments include:

- **Watchful Waiting** or **Active Surveillance**

- **Radical Prostatectomy** (RP) or open surgery which is crucial for recovery of normal urinary and sexual function.

- **External Beam Radiation Therapy** (EBRT) in which high energy X-rays are used to kill cancer cells over seven weeks.

- **Hormone Therapy** that lowers the level of male hormones such as testosterone using injections or oral medication as they fuel cancer growth.

- **Low-Dose Rate (LDR) and High-Dose Rate (LDR) Brachytherapy**

Among these treatment methods, brachytherapy has received popularity because of its faster postoperative recovery time and fewer chronic side effects and surgical complications compared to RP as well as shorter overall treatment time compared with EBRT. For example, urinary incontinence is about 1% with brachytherapy which is much less than with RP, and patient is about 30% less likely to develop erectile dysfunction. This technique which can be improved by robotic assistance will be reviewed in section 1.3.2.

1.3.2   LDR Prostate Brachytherapy

LDR prostate brachytherapy or permanent seed implantation is an efficient minimally invasive procedure for treating early stage prostate cancer. In this procedure, encapsulated radioactive pellets or seeds are introduced into the prostate using long hollow needles inserted through the perineum and a template grid. It is performed by a radiation oncologist or urologist to target cancer cells while maximizing the preservation of healthy tissue. On average, the treatment takes just under one hour from start to finish, and most patients return to normal activities within a couple days.

The outpatient procedure itself involves the placement of 50 to 150 small seeds inside the prostate. The procedure varies with the size and shape of the prostate, and whether the patient has had any previous conformal external beam radiotherapy. The seeds are made of titanium and contain a small amount of radioactive isotope either cesium-131, palladium-103 or iodine-125. Iodine-125 seeds decay, or lose their energy, at a rate of 50% every 60 days. After 10 months, their radioactivity is nearly exhausted. Palladium-103 seeds decay much quicker, losing half their energy every 17 days. They are nearly inert after only 3 months. There is no need to remove the spent seeds, as they do not pose a radiation hazard for the patient. After the placement, the seeds emit an intense amount
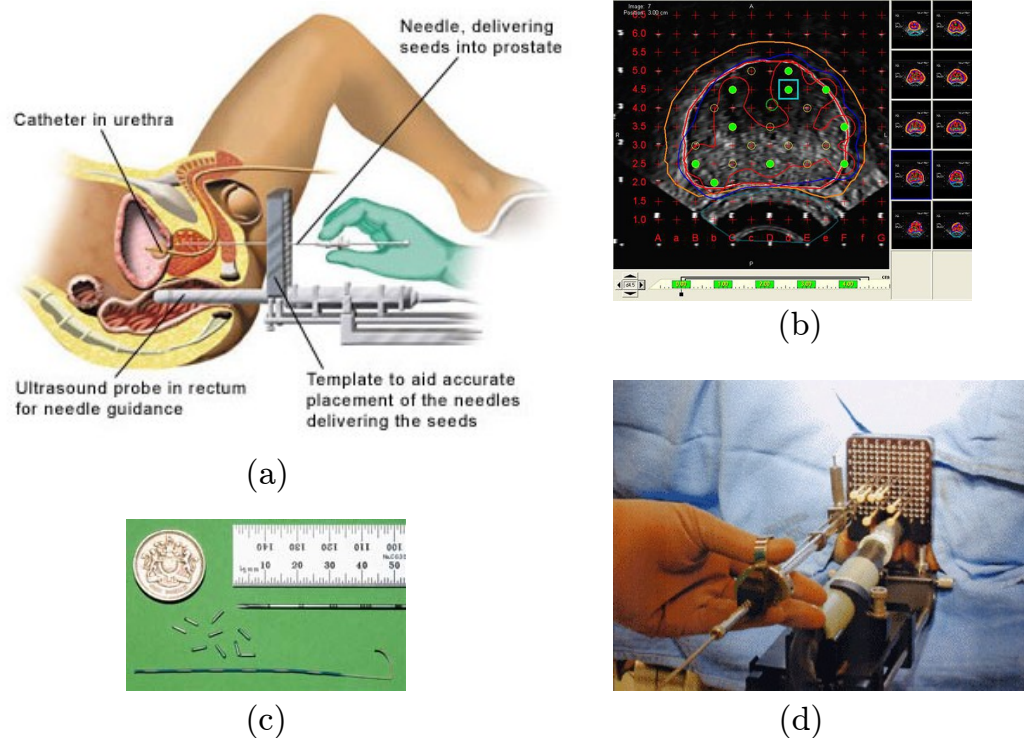
Figure 1.4: TRUS-guided needle insertion and its application in manual LDR prostate brachytherapy: (a) manual seed implantation [8], (b) preoperative dosimetry planning software using 2D ultrasound images [9] (Varian Medical Systems Inc., All rights reserved.), (c) radioactive seeds (pellets) [8], (d) standard grid template and ultrasound probe.

of localized radiation to the cancer in the prostate, and only minimal radiation outside the prostate to other areas, such as the urethra, bladder and rectum. The amount of radiation and its effect in the prostate tumor depend on the number of seeds implanted and their precise positioning determined via dosimetry planning. Note that cancer cells are much more sensitive to radiation than normal cells and can be selectively killed, and the seeds' radiation permanently decays to low level after 9-12 months.

Following the implant procedure, the patient is asked to return for fluoroscopic X-ray confirmation of the seed placement. Three to four weeks after the procedure, a CT scan is also performed to determine the locations of implanted seeds and compare the actual radiation with the dosimetry plan prepared by the medical physicist. A PSA blood test and DRE are checked when the patient returns for a check-up every six months.

Fig. 1.4 shows an overview of a TRUS-guided system for prostate interventions in which the ultrasound-based navigation system provides visualization of the prostatic bed in a

real-time fashion. In this system, due to the inherent low contrast of the images provided
by the ultrasound machine, accurately targeting the areas of interest is impossible, and
abnormalities are not clearly visible during standard manual guidance. Other shortcomings
of manual brachytherapy in the system described above stem from:

- Pubic arch interference in enlarged prostates or in patients suffering from Benign
  Prostate Hyperplasia (BPH) which may not allow parallel needles to reach the entire
  volume of the prostate

- Limited maneuverability as a result of the fixed template and parallel trajectories
  which are 5mm apart

- Fatigue of the clinicians that avoids consistent performance and accuracy

- Needle bending, tissue deformation, prostate shift, and edema that entail re-planning
  or needle adjustment

- Prostate stabilization and seed immobilization to achieve the planned dosimetry

Despite good outcomes of this procedure in clinical practice, there is still room for further
improvement and for making the outcome less dependant on a surgeon's skill. To over-
come the aforementioned problems and improve the performance in terms of accurate seed
implantation, TRUS-guided robotics-assisted prostate brachytherapy is an alternative and
it is expected to replace the manual procedure in clinical practice. Such a system consists
of the following basic components:

1. An imaging modality (primarily TRUS due to its real-time capability and low cost
   but could also be MRI to enhance visualization and image quality)

2. A 4- or 5-DOF (degrees-of-freedom) needle positioning robot

3. A dosimetry planning software for both pre- and intraoperative planning

The positioning robot is installed in the same location as the conventional template. The
planning software offers both pre- and intraoperative planning based on images. Thus, the
computer can calculate the location of seeds and control the robot to position and orient the
needles. The general advantages of TRUS-guided robotics-assisted prostate brachytherapy
are as follows:

- Consistency and accuracy of seed implantation are improved.

- Oblique needle insertion can facilitate access to all parts of the prostate and avoid pubic arch interference.

- Dosimetry and procedure can be merged in a single setting.

- Multiple needle insertions cause edema during the procedure that affects the delivered dose. Therefore, dosimetry can be updated based on the actual seed placement in a real-time or almost real-time fashion.

- Tissue heterogeneities and deformation can be detected using force sensing and imaging feedback.

- There is no need to use a template grid thereby improving maneuverability.

- It is possible to estimate and compensate for needle deflection based on force and position data.

- Needle steering can be performed using velocity modulation and feedback control.

- Visual and/or haptic feedback provides haptic perception for the clinicians if needle holder is appropriately sensorized.

Recent advances in the area of imaging, robotics, and mechatronics have begun to translate into more accurate targeted therapies that include robotics-assisted brachytherapy. Note that the general shortcomings of current ultrasound-based techniques significantly reduce the effectiveness of TRUS-guided therapies. For example, once radioactive seeds are loaded in the prostate gland, their positions cannot be correctly identified during the procedure using an ultrasound machine. This modality also shows poor capability to track needle trajectories intraoperatively. Therefore, it is difficult to determine the achieved dosimetry in real-time or re-plan the positions of new seeds based on the current situation and previous implantation [11]. To enhance the visibility and improve targeting, MRI is a preferable modality for guiding the needle and monitoring the procedure in this system, but places constraints of MR-compatibility of the equipment to be used in proximity of the MRI system.

Apart from the imaging aspects, several robotic systems with different architectures have been manufactured in recent years. The desired trend is to make the robotic system as compact as possible while providing sub-millimeter 3D seed placement accuracy. A maximum error of 2-3 millimeters is tolerable in prostate brachytherapy. Existing robotic systems come in the following two categories, in which the elimination of the grid template increases maneuverability.
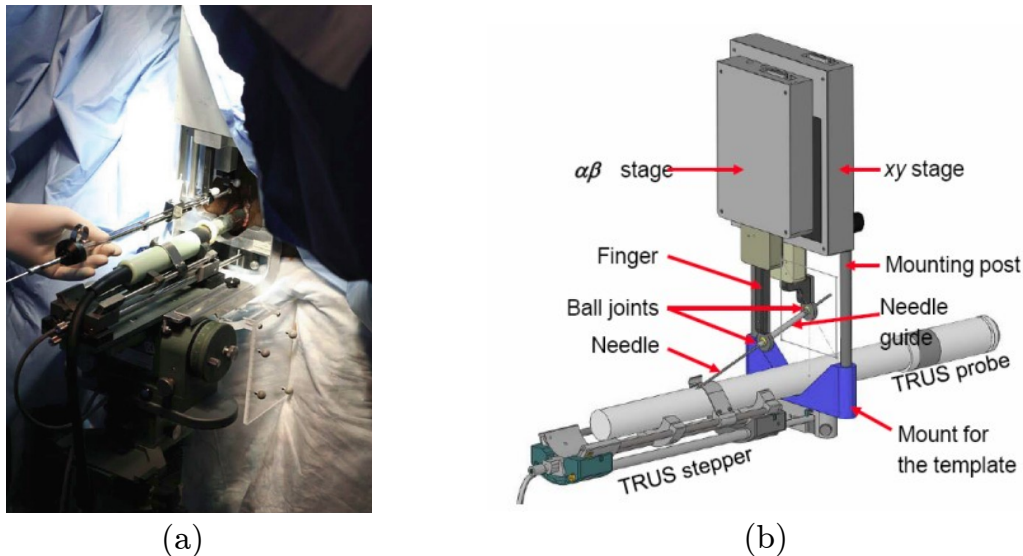
Figure 1.5: TRUS-guided robotic system: (a) the physician can manually correct the needle orientation before approving the position or releasing the payload, (b) mechanical components [12].

- Automated needed positioning, but manual insertion and seed delivery

- Automated needle positioning, insertion and seed delivery

The predicted perspective from a robotics viewpoint is to have an integrated MR-compatible robotic system that could satisfy the following requirements:

1. Image the prostate gland and regions nearby.

2. Model needle-tissue interaction including tissue deformation and needle bending in real-time using sensory information.

3. Steer the brachytherapy needle to the exact locations according to the pre-planning scheme.

Three examples of a sophisticated robotic system designed specifically for prostate brachytherapy or biopsy are depicted in Figs. 1.5 - 1.8 which are briefly reviewed below.

The first system shown in Fig. 1.5 is a TRUS-guided robotics-assisted prostate brachytherapy system [12,13] which was fully integrated with commercial treatment planning system.
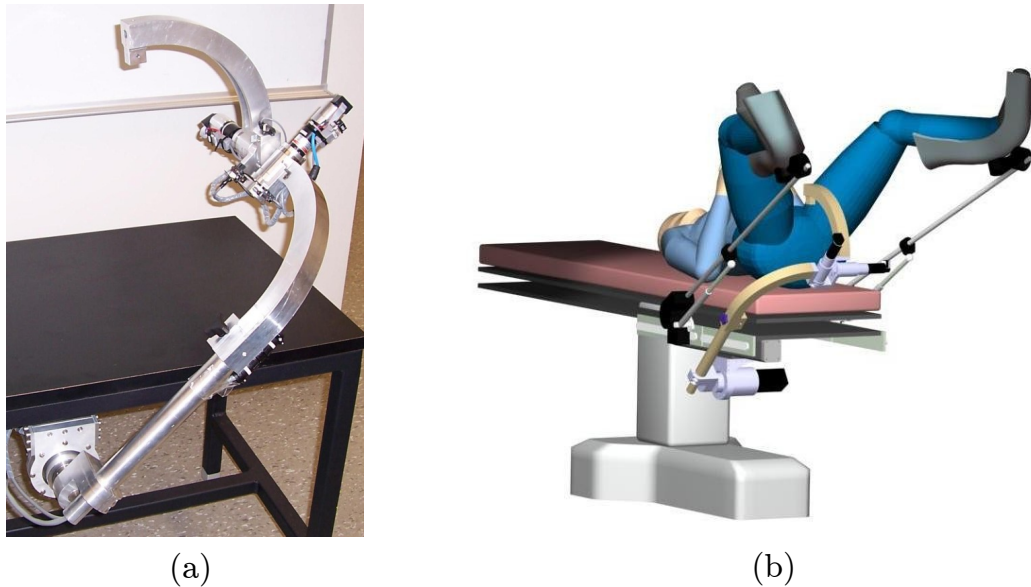
Figure 1.6: Macro manipulator: (a) joint structure [14], (b) high dexterity of the macro arm which provides efficient manipulation in constrained surgical environments such as in prostate brachytherapy (© Copyright 2006, IEEE).

The robotic system replaces the template interchangeably using the same coordinate system, and it fits in the neutral space over the perineum without obstructing the space for a C-arm if one is present. The robotic fingers were also designed to allow an extra 20mm of needle insertion. The unique feature of this system is that it retains the existing clinical setup, hardware and workflow. Furthermore, real-time TRUS images are acquired. Once the seeds are located, the computer promptly calculates a full dosimetry plan based on the implanted seeds as long as the seeds can be visualized.

The second system consisting of two parts shown in Figs. 1.6 and 1.7 is based on a two-tier design called Macro-Micro manipulation. This design is beneficial in terms of providing decoupled motions of the macro and micro stages and thereby enhancing safety. In brief, the macro stage shown in Fig. 1.6(a) is responsible for gross motions and is used to bring the needle tip in contact with the skin entry point. In general, this macro manipulator can carry, accurately position and orient and firmly lock different types of surgical instruments in MIS depending on the application (see Fig. 1.6(b)). In this robot, the normally locked braking system and the simple quick release joint enhance the safety features for emergencies and power shutdown. On the other hand, the micro part depicted in Fig. 1.7(a) provides finer motions and orients and inserts the needle until reaching the desired target. In this specific design, the micro manipulator has backdrivable joints, stationary actuators, and

(a)   (b)
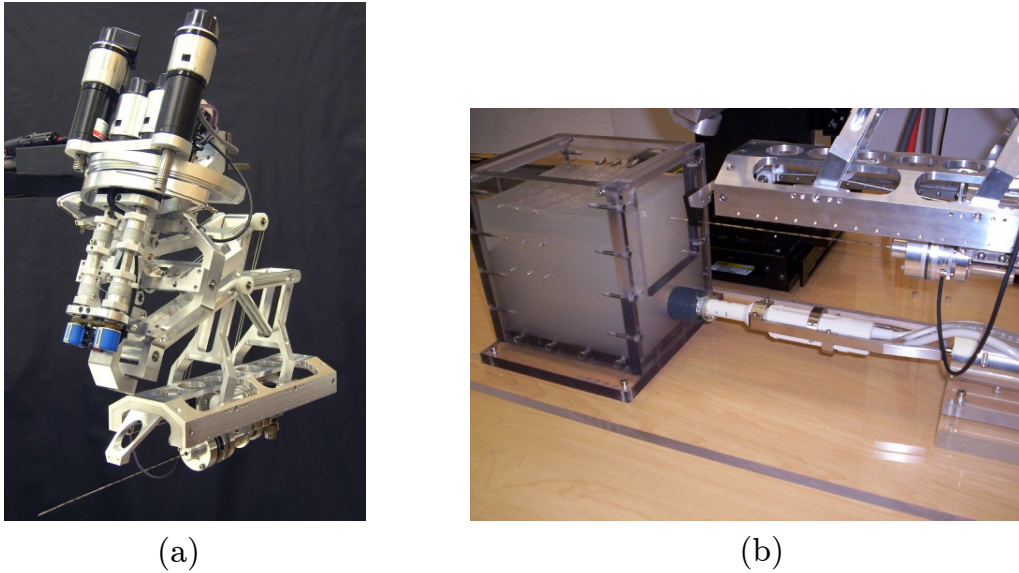
Figure 1.7: Micro manipulator: (a) 5-DOF double-parallelogram robotic structure [15], (b) motorized tracking system for needle guidance in an agar phantom under 3D ultrasound (© Copyright 2007, IEEE).

light-weight linkages, and the system includes a mechanically rotated side-fire transducer to create 3D ultrasound images. The 3D Slicer software [16] is subsequently employed as the user interface to visualize and define target points in the acquired images. The distal assembly of the micro robot holds an off-the-shelf 6-DOF hollow force sensor such that the plunger passes through the center bore of a force sensor and the needle is attached to its tool flange. The use of force sensor facilitates implementation of computer-assisted needle insertion/steering algorithms which is the subject of this thesis. This 5-DOF double parallelogram structure imposes a kinematic constraint on the mechanism such that all five joint axes intersect at a common point to maintain a Remote Center of Motion (RCM). Experimental evaluations of the proposed methodologies in this thesis were carried out using this micro manipulator which is described in more details in Appendix A.

According to the performance analysis, the macro robot operated with an average displacement accuracy of 0.58mm and a roll, pitch and yaw angular accuracies of 0.26º, 0.26º and 0.38º, respectively [14]. In addition, as reported in [15], the average RMS targeting error of the micro assembly was found to be 1.45mm at the average insertion depth of 75.78mm in an agar phantom while 85.7% of the insertions were within less than 2mm error.

In a more recent robotic system [17] demonstrated in Fig. 1.8, a pyramid-shape MR-
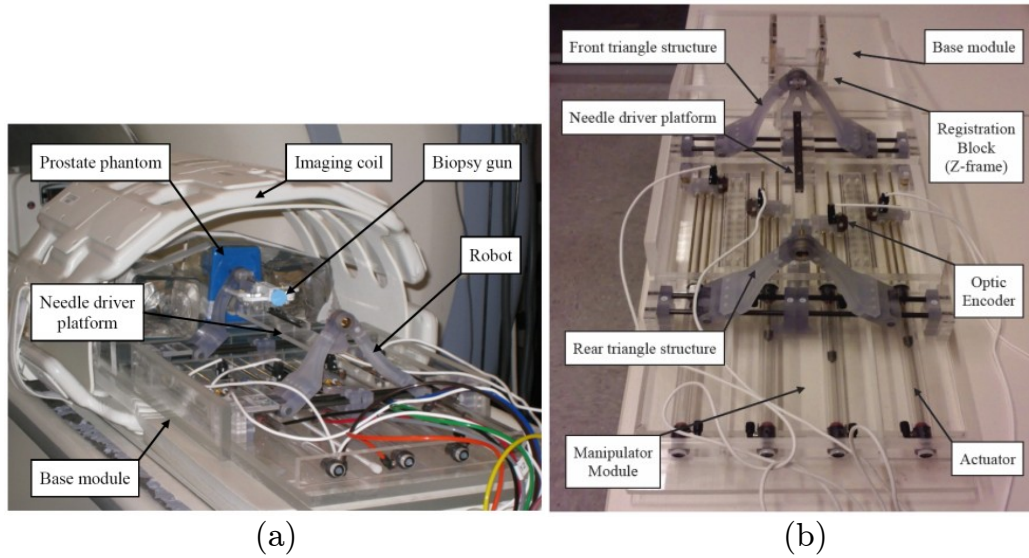
Figure 1.8: (a) 4-DOF MR-compatible parallel robot in the MR bore, (b) rail-and-carriage sliding joint for manual insertion [17] (© Copyright 2010, IEEE).

compatible robot has been designed to maximize the use of "under-legs" space while four pneumatic actuators are located in the lower position to minimize robot space within the limited space. Benefitting from a customized Graphical User Interface (GUI) in the 3D Slicer environment is another advantage of this robotic system. The maximum positioning error was reported to be 0.5mm.

1.4 Literature Review

Among the advantages listed in section 1.3.2 for a robotics-assisted system employed in needle-based interventions, using needle steering to deal with needle-tissue interaction and needle deflection is the main focus of this thesis. Image-based techniques, soft tissue deformation, and mechanical design of medical robotic systems are outside the scope of this study. Therefore, the following survey is in line with the goals of the project described in this thesis.

Several researchers have attempted to simplify the problem of needle insertion/steering and to find a computationally efficient solution through numerical models, though such models can never perfectly mimic the all features of needle-tissue interaction. On account of the fact that a needle guidance technique relies on the validity of the mathematical model

which captures the interaction or needle flexing behavior, accurate modeling is the first step towards control. Eventually, the model can be used either in fully-autonomous steering or in a force feedback teleoperation scheme as a surgeon assistant or as a training simulator [35]. In semi-autonomous steering, the surgeon's expertise for guiding the needle exists in the control loop, while a force control approach allows the slave system to apply a certain amount of force to soft tissue, and insert the needle to the desired depth of penetration. This scheme also gives the operator a realistic sense of the needle-tissue interaction so that the operator can take further actions.

A comprehensive survey on needle insertion and existing early challenges from a general point of view has been performed by Abolhassani et al. [2]. Misra et al. [3] have provided an extensive review of tool-tissue interaction with application in surgical simulations, and van Gerwen et al. [4] have reported the empirical aspects of needle-tissue interaction forces. The following review is based on more theoretical research work with a tighter focus on systematic modeling and steering.

1.4.1   Modeling: Needle-Tissue Interaction and Needle Deflection

When a needle is inserted into tissue, modeling needle deflection and tissue deformation is not an easy task due to the complex nature of interaction forces along the insertion path. Needle deflection and tissue deformation are coupled phenomena both of which are influenced by needle-tissue interaction. For ease of analysis, past work has tried to alleviate this coupling's effect by studying either a flexible needle inserted into rigid tissue or a rigid needle into soft tissue.

With regard to characterization of interaction forces, Okamura and her colleagues performed pioneering work on developing an empirical model for bilateral needle-tissue insertion force. This force is a summation of capsule stiffness force, friction and cutting forces [18]. According to their model, the stiffness force occurs before the puncture of the capsule while the friction and cutting forces occur right after the main puncture. However, in an attempt to experimentally validate the force model, significant variations in liver geometry and its internal structure made a perfect match impossible. They also characterized the impact of the needle diameter and the tip type using a silicone rubber phantom. Podder et al. [19] derived a statistical model to estimate the maximum force that the needle experienced during insertion into the prostate and the perineum. Force data were collected during

prostate brachytherapy to build the model based on (1) patient-specific parameters including age, cancer stage, PSA level, Gleason score, Body Mass Index (BMI), prostate volume, and (2) procedure-specific criteria such as needle size, maximum insertion force, and maximum insertion velocity. They also investigated the effect of insertion and linear velocity modulation on insertion forces and target movement in a Polyvinyl Chloride (PVC) phantom [20], and also experimentally verified that insertion with continuous rotation reduces target motion and interaction forces.

Considering computational efficiency, most of the biophysical models which incorporate monitoring of elastic medium properties might not be amenable to real-time control or be applicable to *in-vivo* experiments. As the most common numerical method for realistic modeling of surgical tool-tissue interactions, the *Finite Element Method* (FEM) divides the continuum into a finite number of subregions called elements, whose behavior is characterized by differential equations governing the motion of material points of a continuum. The element's material, geometric properties, and load distribution within the element and at the corresponding nodes determine the elastic behavior of each element.

Using FEM modeling in [21], needle-tissue interaction forces were modeled by a three-parameter distribution function composed of two step functions with variable amplitudes and spacing. For model validation, a standard brachytherapy needle was inserted into a two-layered PVC phantom. Employing FEM [22], a static linear elastic model in combination with a dynamic force function was developed to accurately model forces and deformations during insertion at varying speeds. However, the accuracy of the model diminished during tissue relaxation. Kobayashi et al. [23] proposed an FEM-based model to reproduce the nonlinear and viscoelastic response of a real liver in terms of generating realistic force-insertion depth relationship, and velocity dependency of needle displacement when a puncture event occurred. DiMaio and Salcudean [24] investigated the insertion of a 17GA symmetric epidural needle in a 2D linearly elastic PVC and then estimated needle shaft forces by monitoring tissue deformation using FEM and a vision system. Hing et al. [25] developed a system to predict soft tissue movement and involved forces using a linear elastic FEM and ABAQUS software. Two C-Arm fluoroscopes were used to image fiducial markers and needle bending. Misra et al. [26] explored the sensitivity of tip axial and transversal forces to tissue rupture toughness, linear and nonlinear tissue elasticity as well as the bevel angle of the tip. Using both contact and cohesive zone models, they incorporated these physical parameters into an FEM, and concluded that a smaller bevel angle

and a larger tissue elasticity result in larger tip forces. Kataoka et al. [27] measured translational friction forces along the needle shaft and analyzed them qualitatively without any explicit quantification. Using an energy-based approach, Mahvash and Dupont [28] studied the friction-deflection curves with respect to needle velocity, and investigated crack propagation during insertion. Reed et al. [29] also developed a mechanics-based approach using the Kelvin-Voigt (KV) interaction model, FEM, and the Karnopp friction model to predict the tip lag angle during rotating a needle inside tissue. They proposed a controller to compensate for torsional friction during needle insertion.

Toward deflection modeling using FEM, the Newton-Euler formulation was applied to a three-link manipulator with torsional springs at each pseudo joint to model needle flexibility [30]. A dynamic scheme was subsequently derived by relating the deflection to the force and torque signals measured at the needle base as well as the interaction forces along the shaft. The interaction forces were generated by the use of FEM.

Generally speaking, FEM is accurate for small linear elastic deformations. But, its numerical efficiency relies highly on (1) the development of effective pre- and post-processing; (2) the material parameters chosen; (3) the scale of deformation, and (4) the algorithm employed for solving the equations of continuum mechanics [31]. Although, researchers have focused efforts on optimizing FEM's computational efficiency and improving its numerical performance [32], due to the time-consuming steps involved in setting up and running an FEM calculation, it does not allow for real-time surgical simulations or intraoperative control. In addition, the large number of state variables involved in utilizing FEM turns the control problem into an ill-conditioned problem which is not desirable for intraoperative control. Another weak point of FEM-based methods for practical purposes is that local deformations are usually provided by markers or beads placed on the surface or implanted into the material. The estimated movement of the beads is then used to validate the model. Obviously, it is difficult to use this procedure under clinical conditions, specially in case of internal organs with complex geometries and boundary conditions.

Several studies have looked at alternative modeling methods. Viscoelastic properties of soft tissues can be represented by rheological models, which are obtained by connecting springs (elastic elements) and dashpots (viscous elements) in serial or parallel combinations. *Mass-spring-damper* or *spring-beam-damper* models are the most common non-continuum mechanics-based techniques used for soft tissue modeling [3]. However, they exhibit limited accuracy, but may work efficiently for real-time simulations. Using this

technique, Yan et al. [33] presented a complex online estimator to approximate the depth-varying tissue parameters through force measurements. A set of local polynomials in finite segments connected in serial was adopted to approximate the unknown parameters of a spring-beam-damper model while the accuracy of the approximation depended on the order of the polynomials and the width of the segments. Keeping the insertion velocity constant, they validated their model using an 18GA needle with a trihedral tip, and a two-layer phantom consisting of PVC and pork. Barbe et al. [34] proposed another online scheme using recursive least-squares with covariance resetting to detect abrupt transitions between tissue layers in *in-vivo* conditions. Accordingly, they integrated this estimator with a KV viscoelastic interaction model to reconstruct and characterize force evolution during insertion, and proposed a statistical method to detect rupture. According to their analysis and possibly due to ignoring friction, an accurate biomechanical model could not be estimated in an online manner. A brief review of the existing biomechanics-based models, which express force as a function of insertion depth and velocity, has also been reported in [34]. Using the same interaction model, associated parallel spring and dashpot combinations were modeled by a set of piecewise linear functions in [35]. In that work, all parameters were identified with a least-squares method and based on the measurements taken at constant insertion velocity from pork tissue.

In the context of bending models, Orcun et al. [36] compared two models in order to simulate the bending of a standard brachytherapy needle. The first FEM-based model took the geometric nonlinearity into account, while the second one comprised a series of rigid bars connected by angular springs. The parameters including Young's modulus for the first model and spring constants for the second model were identified to fit each model to the experimental data. The authors concluded that the angular springs model demonstrated the highest accuracy and computational efficiency compared to the FEM. It was shown that the Young's modulus in the tetrahedral/triangular model depended heavily on the number of elements.

More modeling issues of the needle-tissue interaction from a biophysical view have been reported in [3, 37]. Empirical observations and the role of needle geometry and tissue properties on interaction forces have been summarized in [4]. Note that simulation results have shown that a hybrid method is computationally efficient. In this respect, the small region of tool-tissue interaction is composed of a mass-spring model while the major part of the organ undergoes an FEM-based deformation.

As an alternative to the aforementioned global techniques in needle insertion, *mechanics-based* approaches consider the kinematics of the needle through analyzing the needle geometry and the measured force/torque signals at the base. None of existing models in this category integrate mechanical properties of soft tissue. Abdolhassani and Patel [38] modeled an 18GA bevel-tip needle as an *Euler-Bernoulli* beam and estimated the amount of static deflection based on needle base forces/torques. Misra et al. [39] took advantage of microscopic and macroscopic observations for several needle/gel combinations to characterize the interaction at the bevel tip and along the needle shaft. They proposed a model to account for the needle geometric and material properties as well as the medium's nonlinearity. Based on the energy-based interaction model proposed in [39], Roesthuis et al. [40] applied the *Rayleigh-Ritz* method, and considered the needle as a cantilever beam supported by springs in order to predict the amount of needle deflection.

Ignoring needle-tissue friction and soft tissue displacement, Webster et al. [41] developed *bicycle* and *unicycle* models experimentally for steering a flexible bevel-tip needle in stiff materials, and described this motion by a nonholonomic kinematic system. Due to its simplicity, this model was later on widely exploited for needle steering. This will be covered in section 1.4.2. According to this structure, tissue material can be chosen such that the needle tip acts like a small bicycle with locked handlebars while the needle moves along an arc of approximately fixed radius which is independent of velocity. In more recent research work, inconsistency of this pre-fitted curvature throughout an insertion in artificial phantoms was shown, and a maximum deviation of 24.9% was reported among a set of case studies [42]. As an experimental study, the complexity and variability of needle curvature in terms of needle geometry and insertion velocity into biological tissues were observed and reported in [43]. Compared with artificial phantoms, the lack of a consistent trend was mainly attributed to the inhomogeneity and viscoelasticity of organic tissues.

Several important issues on modeling with applications in needle insertion/steering are still open for further research. These are discussed as recommendations for future work in Chapter 7. In brief, explicitly incorporating and tracking physiological changes as a source of uncertainty in the model and later on in the planner is an open area of research. The challenge is to develop a computationally efficient model that can concurrently describe the behavior of needle-tissue interaction with an acceptable level of accuracy. In many cases, accurate physics behind the model is not deemed a priority.

1.4.2 Steering

After a feasible model for needle deflection is developed and coupled with needle-tissue interaction, we can proceed to the next step toward our ultimate goal to design a model-based path planner based on which tracking goals can be achieved.

Note that in surgical planning the desired tip positioning accuracy and the way by which this flexible tool is guided varies. Current studies refer us to the fact that an employed technique for either modeling or steering is highly influenced by restrictions imposed by both the clinical application and the existing technology. For example, in biopsies of organs such as breast, prostate, liver, and lung, determining possible tumor location as the needle penetrates the tissue is of primary importance, while in brachytherapy, reaching the target accurately in order to place radioactive seeds is the main concern. In all these examples, placement accuracy of millimeters is desirable while in brain, eye and ear procedures, sub-millimeter accuracy is required. In biopsies of the breast, ovaries, liver, prostate, and kidney, the targeted area is usually located at a depth of 5 to 10cm depending on the patient's body. Fine needles from 18 to 25 GA are mainly used for tissue aspiration. In other procedures, for example the Chorionic Villus Sampling (CVS), needles of 18 to 20 GA and 10cm long are inserted to collect a sample of the placental tissue for fetal karyotyping while having to avoid the pubic arch [60].

Path planning for bevel-tip needles has been studied in several ways, most of which are applicable only to a planar situation. Steerability and needle bending are afforded by asymmetric forces acting at the needle tip and tissue deformation is often disregarded. Note that accurately planning for such steerable needles is complex, and requires solving inverse kinematics for a nonholonomic system or deriving a perfect model to capture the interaction features. To date, no integrated control strategy has been suggested for autonomous needle steering, which could be extended as a reference for future comparison, and research in this area is still in its early stages.

Taking advantage of the *bicycle* model [41], Alterovitz et al. [44] formulated planar needle steering in rigid tissues as a Markov Decision Process (MDP) to derive a simulation-based optimal planner. They also proposed a planning framework based on a Stochastic Motion Roadmap (SMR) that computes the path that is most likely to succeed in terms of hitting the target [45]. In another study, a feedback controller was proposed to stabilize a flexible bevel-tip steerable needle to a desired 2D plane in 3D motion [46]. In conjunction with

this observer-controller pair, Reed et al. [47] used the SMR planner presented in [45] as a high-level controller inside an integrated system. Concurrently, an image-based low-level planner was employed as an observer [46] to estimate the pose of the needle in 2D. For validation, a nitinol wire with a diameter of 0.61mm was inserted in a plastisol tissue phantom. Using the idea of the *Dubin's* car [48, 49], Duindam et al. [50] simulated a new 3D motion planner for rigid tissue based on explicit geometric inverse kinematics. Here, similar to the *bicycle* model, the needle was interpreted as an airplane with constant speed and pitch rate, zero yaw, and controllable roll angle.

It should be noted that the aforementioned steering methods are based on the following fundamental modeling assumptions, any violations of which may lead to poor performance.

- The needle-tissue interaction follows the *bicycle* model [41].

- The motion of the needle is fully characterized by the motion of the needle tip, i.e., the needle body perfectly tracks the tip without applying considerable lateral force to the tissue.

- The tip orientation is manipulated by changing the orientation at the base, because the torsional effect is either negligible or compensated using a torsion model [29].

In conjunction with the *bicycle* model, the use of duty-cycled spinning as an alternative steering technique facilitates more curved trajectories, thereby giving the planner a more reachable workspace through adjustable arcs. This strategy, which has been developed by Riviere and his colleagues [51, 52], and is useful for guiding a needle around obstacles during insertions performed in a confined workspace. Combing this idea with the classic Rapidly-Exploring Random Tree (RRT) algorithm, Bernardes et al. [53] introduced a 2D planner with the capability to search for a fast and feasible solution. Integration of image feedback in the planner by the same group allowed the operator to manually update the curvature value and thus replan the trajectory, in order to account for possible changes in the environment [54]. However, continuous needle rotation may lead to extra tissue damage and trauma. So there is no clear agreement over the practicality of the duty-cycling steering technique in clinical practice.

Glozman and Shoham [55] presented 2D path planning using the concept of virtual springs and inverse kinematics based on the assumption of quasi-static motion. They modeled

needle-tissue interaction with a combination of lateral springs distributed along the needle. As the needle penetrates soft tissue, the location and orientation of the virtual springs change accordingly, and since the tissue elastic modulus changes as a function of strain, the coefficients of the springs are updated based on the strain-dependent dynamic elastic modulus. Using ultrasound imaging and the inverse kinematics of the virtual spring model, the needle base was manipulated, in order to guide the needle with a 2D tracking error below 1mm [56].

In a very recent study, to overcome the limitations of trajectory control and provide multiple curved segments rather than only the natural curvature, Ko et al. [57] manufactured the first prototype of a bioinspired multi-part probe in which the steering angle was a function of the offset between interlocked probe segments. Deriving a kinematic model of the flexible probe and using feedback control, *in-vitro* results demonstrated satisfactory 2D trajectory tracking of this *car-like* robot with a tracking error of 0.68mm (std=1.45mm).

Other methods of steering have been proposed in the literature with more emphasis on minimization of bending, biophysical simulation, or the preoperative aspect of the problem rather than real-time control. These methods is mostly aimed at designing computer simulators for training purposes. This category of needle guidance mechanisms are usually referred to in the literature as insertion or planning rather than steering.

In an effort to minimize needle deflection, a model-based strategy for successive needle rotation through 180 degrees was proposed in [58]. Finding the proper depth for changing the bevel direction, the maximum bending was limited to a predefined threshold value. Torabi et al. [59] proposed a single-point tissue manipulation technique to improve the accuracy and accessibility of needle insertion procedures. Based on stochastic optimization, the insertion path and manipulation locations were selected such that the pre-planner was able to guide a needle toward a target while avoiding sensitive tissue. Incorporating soft tissue motion, needle flexibility and a physically-based linear FEM-based model, DiMaio and Salcudean [60] introduced a manipulation Jacobian relating the base motion to tip motion for 2D steering and then applied a *potential fields technique* to demonstrate the tip placement and obstacle avoidance. Alterovitz et al. [61] optimized the initial point and angle for planar insertion of a flexible needle in order to reach a target while avoiding obstacles. This pre-planning technique involves transformation of a constrained optimization problem into an unconstrained one using a *penalty method* followed by a gradient descent algorithm. The algorithm can be used preoperatively to optimize the insertion parameters

in order to achieve accurate prostate brachytherapy implants. As opposed to gradient-based approaches, Dehghan and Salcudean [62] developed a path planning method for insertion of a rigid straight needle into deformable tissue using FEM. The insertion point, needle heading, and needle depth were optimized by minimizing the distance between the needle and a number of target points inside the tissue. At each iteration, the best 3D line fitted to the displaced targets in the deformed tissue was employed as a candidate for the new insertion line. This technique is directly applicable to prostate brachytherapy, where the goal is to generate straight-line trajectories rather than curved paths. The last two methods focus on optimizing certain initial insertion parameters while it is presumed that the needle will be directly guided without any further manipulation once the initial parameters are properly set.

To conclude this section, we note that there has been little attention paid to fully-automated robotics-assisted model-based needle steering in the presence of a flexible needle and deformable tissue. This fact serves as the main motivation of this thesis.

1.5 Research Statement: Objectives and Assumptions

Needle deflection and tissue deformation or target movement are major problems for accurate needle steering. In this study, it is assumed that target location is known a priori, or it is determined using real-time imaging. Thus, the main focus is to (1) explore needle-tissue interaction; (2) capture the steady-state and transient behaviors of contact forces, and (3) model needle deflection in an accurate and computationally efficient manner without using an image-based or FEM-based method. Next, a model-based path planner is designed such that flexibility and needle shape are the bases for trajectory generation for needle steering. The long-term objective of this study is to identify needle-tissue interaction properties and develop a needle bending model based on which the control law is implemented. Note that developing a fully-automated needle steering strategy capable of handling interaction uncertainties that are complex in nature is currently missing in the literature.

Straight needle insertion, bending minimization, and deformation reduction, which have been the subject of numerous research publications [58, 59, 61, 62], are not main priorities in this study. Instead, we take advantage of the maneuverability and flexibility properties of a bevel-tip needle for path planning. See Fig. 1.2. This illustration exhibits very

curved trajectories which are probably not feasible in practice. However, a general steering mechanism, if successfully deployed, has features that can also provide greater control for straight needle insertion in inhomogeneous, nonlinear viscoelastic tissue which is essential in several clinical applications.

Note that among the reported ways of deflection modeling in section 1.4.1, simple static solutions [38, 58, 64] cannot represent relevant aspects of needle-tissue interaction. With regard to advanced modeling [63], an analytical beam-based solution is desired to account for the effective forces, and relate them to the net bending. The axial insertion force is the summation of two major force components consisting of the cutting force at the tip and the distributed friction along the needle shaft. In this thesis, the lateral compressive force applied by soft tissue is interpreted as a normal force that generates frictional effects.

As the needle advances, soft tissues around the needle are compressed so that the bevel asymmetry creates a moment at the tip causing the needle to deflect laterally. Knowing the needle bending, and given a target and possible obstacle locations, the planner is intended to calculate a feasible trajectory that avoids the obstacles and reaches the target. The motion of the needle is determined kinematically by two control inputs (or two DOFs) as follows:

- Linear translation in the insertion direction

- Bevel orientation about the translational axis

The needle geometry and interaction properties are presumed to be known prior to steering. As the needle is rotated, the bevel tip is reoriented in space so that subsequent insertion follows an arc in the opposite plane. The value of the twisting torque is used to compensate for the torsional lag as proposed in [29]. Deflection from the desired deterministic path, which is a circular segment in this case, is modeled by a Gaussian perturbation applied to the tip angle. More details on the stochastic modeling and the discretization method are provided in Chapter 6.

1.6 Contributions and Thesis Structure

This section briefly explains the main contributions of this thesis. Each contribution is reported as a separate chapter in the thesis. The outline of the thesis is as follows.

In Chapter 2, the contact mechanism between a needle and soft tissue is investigated. The main objective of this study is to identify and quantify needle-tissue properties in the force domain. Encouraged by the LuGre model for representing friction forces in general, the proposed model in this chapter captures all stages of needle-tissue interaction including puncture, cutting, and friction forces. Accordingly, the insertion force is modeled by a novel nonlinear dynamic model in an efficient online approach without explicit incorporation of biomechanical aspects. Furthermore, an estimation algorithm for identifying the parameters of the proposed model is presented that is based on sequential asynchronous joint-extended Kalman filtering. The algorithm compares the axial force measured at the needle base with its expected value and then adapts the model parameters to represent the actual interaction force. While the nature of this problem is mathematically very complex, the use of multiple Kalman filters makes the system adaptable for capturing force evolution, including insertion and retraction phases during a standard interventional procedure. This technique releases the need to model each force component separately, and then add them together to produce the entire interaction force.

Having obtained insight into the complicated nature of needle-tissue interaction in Chapter 2, a new method for modeling translational friction during needle insertion is introduced in Chapter 3. Research on friction models has a long and rich history; however, the importance of this force component in needle insertion deserves further investigation. When a very fine needle is inserted into soft tissue, translational friction can play an important role in deflection mechanics. This would be a matter of more importance when a stop-and-rotate motion profile at low insertion velocities is implemented, and thus, the system is repeatedly transitioned from a pre-sliding to a sliding mode and vice versa. In this study, a distributed version of the well known LuGre model in the state-space form is adopted to account for dynamic friction along the contact surface. It is also proposed to derive the best force density function or normal pressure which influences the distributed friction, and then identify the differential equation using empirical data. This strategy also facilitates estimating cutting force in an intraoperative manner. According to the literature, the cutting force has a very complex pattern; so it is not very straightforward to find a realistic model for it. In practice, the friction model performs well in a number of organic and artificial phantoms, e.g., agar, gelatin, and beef liver, while exhibiting favorable static and dynamic frictional features. The results illustrate that the presented approach represent the main features of friction which is a major force component in needle-tissue interaction during needle-based interventions.

Chapter 4 deals with soft tissue deformation and its correction in friction-velocity cycles. Friction in general depends on relative velocity between moving contacts, and force-velocity mapping is an indicator of interaction characteristics. Soft tissue deformation is an inevitable and complex phenomenon that occurs during needle insertion, and results in relative motion. In this chapter, a high-gain observer is presented which can track this relative motion in a simple manner with no need for imaging or computer vision. The main purpose of this study is to provide a means of compensating for the velocity of tissue with respect to a moving needle in the insertion direction. Thus, the presented functional routine in conjunction with the previously developed friction structure in Chapter 3 can represent the dynamic nature of translational friction in the presence of tissue deformation. The entire scheme is, therefore, applicable to a wide range of needle-tissue combinations without excessive computational cost.

In Chapter 5, planar needle deflection is discussed. Needle flexion in general is directly linked to the interaction forces experienced by the needle. In previous chapters, needle-tissue interaction and the associated force components during a needle-based intervention were investigated. Dynamic response analysis of a beam-like structure on an elastic foundation under moving or distributed loads has been the subject of considerable research. This concept is used in Chapter 5 to model needle bending. Using intraoperative force measurements at the needle base, this approach relates mechanical and geometric properties of needle-tissue interaction to the net amount of deflection and estimates the needle curvature. In the proposed structure, tissue resistance is considered by adding virtual springs along the needle shaft in the *Euler-Bernoulli* beam setting, and the impact of distributed friction is incorporated by introducing a moving distributed external force to the bending equations. Cutting force also appears in the equations as sub-boundary conditions of the set of PDEs for two coupled sub-beams. Finally, an analytical solution of the PDEs governing the planar deflection is obtained using Green's functions. Due to the geometry of our problem and existing moving boundary conditions, the common method of separation of variables is not applicable to this case. Instead, using the Green's function provides us with a closed-form solution in an integral form.

Chapter 5 presents a new 2D motion planner for steering flexible needles inside relatively rigid tissue. We use a nonholonomic system approach, which models tissue-needle interaction, and formulates the problem as a Markov Decision Process that is solvable using infinite horizon dynamic programming (DP). Unlike conventional numerical solvers such

as the value iterator which inherently suffers from the curse of dimensionality for processing large-scale models, partitioned-based solvers show promising numerical performance. Given the locations of the obstacles and the targeted area, the proposed solver provides a descent solution where high spatial or angular resolution is required. As theoretically expected, it is shown how prioritized partitioning increases computational performance compared to the generic value iteration which was used in an earlier planning approach. Starting from any initial condition in the workspace, this method enables the needle to reach its target and avoid collisions with obstacles through selecting the shortest path with the least number of turning points, thereby causing less trauma. In this chapter, emphasis is given to the control aspects of the problem rather than to biomedical issues. Experimental results of a phantom test show that the method is capable of positioning the needle tip at the targeted area with an acceptable level of accuracy.

Chapter 6 presents a theoretic approach for 2D needle steering. Given the locations of the obstacles and the targeted area, this method provides a descent solution where high positioning resolution is required. Similar to the DP-based techniques reviewed in section 1.4.2, this algorithm takes advantage of a nonholonomic system approach, and formulates the steering problem as an MDP. Unlike conventional numerical solvers, e.g., the value iterator, which inherently suffers from the curse of dimensionality for processing large-scale models, a new solver based on prioritization and partitioning of the workspace is proposed which shows promising numerical performance. Starting from any initial condition in the workspace, this method enables the needle to reach its target and avoid collisions with obstacles through selecting the shortest path with the least number of turning points thereby causing less trauma. Herein, emphasis is given to the control aspects of the problem rather than to biomedical issues. Experimental results in artificial phantom indicate good performance of the steering mechanism in 2D. Collision avoidance is maintained in this planner, and the shortest path with the least number of needle turnings is selected in order to minimize tissue trauma.

Chapter 7 summarizes the research described in the thesis, and provides concluding remarks. Guidelines, directions and suggestions for future work are also outlined in this final chapter.

Bibliography

[1] http://www.miamiroboticprostatectomy.com/robotic-prostatectomy.htm

[2] N. Abolhassani, R. Patel, and M. Moallem, "Needle Insertion into Soft Tissue: A Survey," *Med. Eng. Phys.*, vol. 29, pp. 413-431, 2007.

[3] S. Misra, K.T. Ramesh, and A.M. Okamura, "Modeling of Tool-Tissue Interactions for Computer-based Surgical Simulation: A Literature Review," *Presence-Teleop. Virt.*, vol. 17, no. 5, pp. 463-491, 2008.

[4] D.J. Van Gerwen, J. Dankelman, and J.J. van den Dobbelsteen, "Needle-Tissue Interaction Forces: A Survey of Experimental Data," *Med. Eng. Phys.*, vol. 34, no. 6, pp. 665-680, 2012.

[5] T.J. Carter, M. Sermesant, D.M. Cash, D.C. Barratt, C. Tanner, and D.J. Hawkes, "Application of Soft Tissue Modelling to Image-Guided Surgery," *Med. Eng. Phys.*, vol. 27, pp. 893-909, 2005.

[6] H. Delingette, "Towards Realistic Soft Tissue Modeling in Medical Simulation," *In Proc. of the IEEE Special Issue on Surgery Simulation*, vol. 85, no. 3, pp. 512-523, 1998.

[7] http://www.prostatecancer.ca.

[8] http://www.prostatecancercentre.co.uk/treatments/brachy.html.

[9] http://www.varian.com/us/oncology/brachytherapy/treatment-planning-systems.html#.UQwtZx2Zkrp

[10] S. Jeschke, E. Schweigreiter, and G. Janetschek, "Role of Imaging in Prostate Cancer: A Review," *Imaging Decisions*, vol. 13(3-4), pp. 68-87, 2009.

[11] B. Turkbey, P.A. Pinto, and P.L. Choyke, "Imaging Techniques for Prostate Cancer: Implications for Focal Therapy," *Medscape Nat. Rev. Urol*, vol. 6, pp. 191-203, 2009.

[12] G. Fichtinger, J.P. Fiene, C.W. Kennedy, G. Kronreif, I. Iordachita, D.Y. Song, E.C. Burdette, and P. Kazanzides, "Robotic Assistance for Ultrasound-guided Prostate Brachytherapy," *Medical Image Analysis*, vol. 12, pp. 535Ű545, 2008.

[13] D.Y. Song, E.C. Burdette, J. Fiene, E. Armour, G. Kronreif, A. Deguet, Z. Zhang, I. Iordachita, G. Fichtinger, and P. Kazanzides, "Robotic Needle Guide for Prostate Brachytherapy: Clinical Testing of Feasibility and Performance," *Brachytherapy*, vol. 10, pp. 535-545, 2011.

[14] B. Yousef, R. Patel, and M. Moallem, "A Macro-Robot Manipulator for Medical Applications," *In Proc. of IEEE Int. Conf. on Systems, Man and Cybernetics (SMC)*, Taiwan, 2006, pp. 530-535.

[15] H. Bassan, T. Hayes, R.V. Patel and M. Moallem, "A Novel Manipulator for 3D Ultrasound Guided Percutaneous Needle Insertion," *In Proc. of IEEE Int. Conf. on Rob. Autom. (ICRA)*, Italy, 2007, pp. 617-622.

[16] http://www.slicer.org/slicerWiki/index.php/Documentation/4.2/Training.

[17] S.E. Song, N.B. Cho, G. Fischer, N. Hata, C. Tempany, G. Fichtinger, and I. Iordachita, "Development of a Pneumatic Robot for MRI-Guided Transperineal Prostate Biopsy and Brachytherapy: New Approaches," *In Proc. of IEEE Int. Conf. on Rob. Autom. (ICRA)*, USA, 2010, pp. 2580-2585.

[18] A.M. Okamura, C. Simone, and M.D. O'Leary, "Force Modeling for Needle Insertion into Soft Tissue," *IEEE Trans. Biomed. Eng.*, vol. 51, no. 10, pp. 1707-1716, 2004.

[19] T.K. Podder, J. Sherman, E.M. Messing, D.J. Rubens, D. Fuller, J.G. Strang, R.A. Brasacchio, and Y. Yu, "Needle Insertion Force Estimation Model Using Procedure-Specific and Patient-Specific Criteria," *In Proc of 28th IEEE EMBS Annu. Int. Conf.*, 2006, pp. 555-558.

[20] T.K. Podder, J. Sherman, D. Fuller, E.M. Messing, D.J. Rubens, J.G. Strang, R.A. Brasacchio, and Y. Yu, "In Vivo Measurement of Surgical Needle Intervention Parameters: A Pilot Study," *In Proc of 28th IEEE EMBS Annu. Int. Conf.*, 2006, pp. 3652-3655.

[21] E. Dehghan, X. Wen, R. Zahiri-Azar, M. Marchal, and S.E. Salcudean, "Parameter Identification for a Needle-Tissue Interaction Model," *In Proc. of 29th IEEE EMBS Annu. Int. Conf.*, 2007, pp. 190-193.

[22] J.R. Crouch, C.M. Schneider, J. Wainer, and A.M. Okamura, "A Velocity-Dependent Model for Needle Insertion in Soft Tissue," *In Proc. of Medical Image Computing and Computer Assisted Intervention (MICCAI)*, 2005, pp. 624-632.

[23] Y. Kobayashi, A. Onishi, H. Watanabe, T. Hoshi, K. Kawamura, and M.G. Fujie, "In Vitro Validation of Viscoelastic and Nonlinear Physical Model of Liver for Needle Insertion Simulation," *In Proc of 2nd Biennial IEEE/RAS-EMBS Int. Conf. on Biomedical Robotics and Biomechatronics*, 2008, pp. 469-476.

[24] S.P. DiMaio, S.E. Salcudean, "Needle Insertion Modelling and Simulation," *IEEE Trans. Robot. Autom.*, vol. 19, no. 5, pp. 864-875, 2003.

[25] J.T. Hing, A.D. Brooks, and J.P. Desai, "Reality-based Estimation of Needle and Soft Tissue Interaction for Accurate Haptic Feedback in Prostate Brachytherapy Simulation," *Springer Tracts in Advanced Robotics*, vol. 28, pp. 34-48, 2007.

[26] S. Misra, K.B. Reed, A.S. Douglas, K.T. Ramesh, and A.M. Okamura, "Needle-Tissue Interaction Forces for Bevel-Tip Steerable Needles", *In Proc of 2nd Biennial IEEE/RAS-EMBS Int. Conf. on Biomedical Robotics and Biomechatronics*, 2008, pp. 224-231.

[27] H. Kataoka, T. Washio, K. Chinzei, K. Mizuhara, C. Simone, and A.M. Okamura, "Measurement of the Tip and Friction Force Acting on a Needle During Penetration," *In Proc. of 5th Int. Conf. on Med. Image Comput. Comput. Assist. Intervention (MICCAI)*, 2002, pp. 216-223.

[28] M. Mahvah, P.E. Dupont, "Mechanics of Dynamic Needle Insertion into a Biological Material," *IEEE Trans. Biomed. Eng.*, vol. 57, no. 4, pp. 934-943, 2010.

[29] K.B. Reed, A.M. Okamura, and N.J. Cowan, "Modeling and Control of Needles with Torsional Friction," *IEEE Trans. Biomed. Eng.*, vol. 56, no. 12, pp. 2905-2916, 2009.

[30] A. Haddadi, K. Hashtrudi-Zaad, "Development of a Dynamic Model for Bevel-Tip Flexible Needle Insertion into Soft Tissues," *In Proc. of 33rd IEEE EMBS Annu. Int. Conf.*, 2011, pp. 7478-7482.

[31] J. Ma, *et al.*, "Accuracy of Non-Linear FE Modelling for Surgical Simulation: Study Using Soft Tissue Phantom," *Comp. Biomec. Med.*, part 1, pp. 29-41, 2010.

[32] I. Khalaji, K. Rahemifar, and A. Samani, "Statistical Finite Element Analysis," *In Proc. of 30th IEEE EMBS Annu. Int. Conf.*, 2008, pp. 5577-5580.

[33] K.G. Yan , T. Podder, Y. Yu, T. Liu, and C.W.S. Cheng, "Flexible Needle-Tissue Interaction Modeling with Depth-Varying Mean Parameter: Preliminary Study," *IEEE Trans. Biomed. Eng.*, vol. 56, no. 2, pp. 255-262, 2010.

[34] L. Barbe, B. Bayle, and M. de Mathelin, "In Vivo Model Estimation and Haptic Characterization of Needle Insertions," *Int. J. Rob. Res.*, vol. 26, no. 11-12, pp. 1283-1301, 2007.

[35] P.L. Yen, R. Hibberd, and B. Davies, "A Telemanipulator System as an Assistant and Training Tool for Penetrating Soft Tissue," *Mechatronics*, vol. 6, no. 4, pp. 377-489, 1996.

[36] O. Goksel, E. Dehghan, and S.E. Salcudean, "Modeling and Simulation of Flexible Needles," *Med. Eng. Phys.*, vol. 31, pp. 1069-1078, 2009.

[37] J.T. Hing, A.D. Brooks, and J.P. Desai, "A Biplanar Fluoroscopic Approach for the Measurement, Modeling, and Simulation of Needle and Soft Tissue Interaction," *Med. Image Anal.*, vol. 11, pp. 62-78, 2007.

[38] N. Abdolhassani, R.V. Patel, "Deflection of a Flexible Needle During Insertion into Soft Tissue," *In Proc. of 28th IEEE EMBS Annu. Int. Conf.*, USA, 2006, pp. 3858-3861.

[39] S. Misra, K.B. Reed, B.W. Schafer, K.T. Ramesh, and A.M. Okamura, "Observations and Models for Needle-Tissue Interactions," *In Proc. of IEEE Int. Conf. on Rob. Autom. (ICRA)*, Japan, 2009, pp. 2687-292.

[40] R.J. Roesthuis, Y.R.J. van Veen, A. Jahya, and S. Misra, "Mechanics of Needle-Tissue Interaction," *In Proc. of IEEE/RSJ Int. Conf. on Intel. Rob. Sys. (IROS)*, 2011, pp. 2557-2563.

[41] R.J. Webster III, J.S. Kim, N.J. Cowan, G.S. Chirikjian, and A.M. Okamura, "Nonholonomic Modeling of Needle Steering," *Int. J. Rob. Res.*, vol. 25, no. 5-6, pp. 509-525, 2006.

[42] S. Misra, K.B. Reed, B.W. Schafer, K.T. Ramesh, and A.M. Okamura, "Mechanics of Flexible Needles Robotically Steered through Soft Tissue," *Int. J. Rob. Res.*, vol. 29, 2010, pp. 1640-1660.

[43] A. Majewicz, T.R. Wedlick, K.B. Reed, and A.M. Okamura, "Evaluation of Robotic Needle Steering in *ex vivo* Tissue," *In Proc. of IEEE Int. Conf. on Rob. Autom. (ICRA)*, 2010, pp. 2068-2073.

[44] R. Alterovitz, A. Lim, K. Goldberg, G.S. Chirikjian, and A.M. Okamura, "Steering Flexible Needles under Markov Motion Uncertainty," *In Proc. of IEEE/RSJ Int. Conf. on Intel. Rob. Sys. (IROS)*, 2005, pp. 120-125.

[45] R. Alterovitz, M. Branicky, and K. Goldberg, "Motion Planning under Uncertainty for Image-Guided Medical Needle Steering," *Int. J. Rob. Res.*, vol. 27, no. 11-12, pp. 1361-1374, 2008.

[46] V. Kallem, N. Cowan, "Image-Guidance of Flexible Tip-Steerable Needles," *IEEE Trans. on Robotics*, vol. 25, no. 1, pp. 191-196, 2009.

[47] K.B. Reed, V. Kallem, R. Alterovitz, K. Goldberg, A.M. Okamura, and N.J. Cowan, "Integrated Planning and Image-Guided Control for Planar Needle Steering," *In Proc. of 2nd Biennial IEEE/RAS-EMBS Int. Conf. on Biomedical Robotics and Biomecha-tronics*, 2008, pp. 819-824.

[48] J.P. Laumond, S. Sekhavat, and F. Lamiraux, "Guidelines in Nonholonomic Motion Planning for Mobile Robots, Robot Motion Planning and Control," *Lect. Notes Contr. Inf.*, vol. 229, pp. 1-53, Springer Berlin Heidelberg; 1998.

[49] P. Soueres1 and J.D. Boissonnat, "Optimal Trajectories for Nonholonomic Mobile Robots, Robot Motion Planning and Control," *Lect. Notes Contr. Inf.*, vol. 229, pp. 93-170, Springer Berlin Heidelberg; 1998.

[50] V. Duindam, J. Xu, R. Alterovitz, S. Sastry, and K. Goldberg, "Three-Dimensional Motion Planning Algorithms for Steerable Needles Using Inverse Kinematics," *Int. J. Rob. Res.*, vol. 29, pp. 789-800, 2010.

[51] D. Minhas, J. Engh, M. Fenske, and C. Riviere, "Modeling of Needle Steering via Duty-Cycled Spinning," *In Proc. of 29th IEEE EMBS Annu. Int. Conf.*, France, 2007, pp. 2756-2759.

[52] N.A. Wood, K. Shahrour, M.C. Ost, and C.N. Riviere, "Needle Steering System Using Duty-Cycled Rotation for Percutaneous Kidney Access," *In Proc. of* 32nd *IEEE EMBS Annu. Int. Conf.*, 2010, pp. 5432-5435.

[53] M.C. Bernardes, B.V. Adorno, P. Poignet, N. Zemiti, and G.A. Borges, "Adaptive Path Planning for Steerable Needles Using Duty-Cycling," *In Proc. of IEEE/RSJ Int. Conf. on Intel. Rob. Sys. (IROS)*, USA, 2011, pp. 2545-2550.

[54] M.C. Bernardes, B.V. Adorno, P. Poignet, and G.A. Borges, "Semi-Automatic Needle Steering System with Robotic Manipulator," *In Proc. of IEEE Int. Conf. on Rob. Autom. (ICRA)*, 2012, pp. 1595-1600.

[55] D. Glozman, M. Shoham, "Image-Guided Robotic Flexible Needle Steering," *IEEE Trans. Rob.*, vol. 23, no. 3, pp. 459-467, 2007.

[56] Z. Neubach, M. Shoham, "Ultrasound-Guided Robot for Flexible Needle Steering," *IEEE Trans. Biomed. Eng.*, vol. 57, no. 4, pp. 709-805, 2010.

[57] S.Y. Ko, L. Frasson, and F.R. y Baena, "Closed-Loop Planar Motion Control of a Steerable Probe with a Programmable Bevel Inspired by Nature," *IEEE Trans. Rob.*, vol. 27, no. 5, pp. 970-983, 2011.

[58] N. Abolhassani, R.V. Patel, and F. Ayazi, "Minimization of Needle Deflection in Robot-Assisted Percutaneous Therapy," *Int. J. Med. Robotics Comput. Assist. Surg.*, vol. 3, pp. 140-148, 2007.

[59] M. Torabi, K.K. Hauser, R. Alterovitz, V. Duindam, and K. Goldberg, "Guiding Medical Needles Using Single-Point Tissue Manipulation," *In Proc. of IEEE Int. Conf. on Rob. Autom. (ICRA)*, 2009, pp. 2705-2710.

[60] S. DiMaio, S.E. Salcudean, "Needle Steering and Motion Planning in Soft Tissues," *IEEE Trans. Biomed. Eng.*, vol. 52, no. 6, pp. 965-974, 2005.

[61] R. Alterovitz, K. Goldberg, and A. Okamura, "Planning for Steerable Bevel-Tip Needle Insertion Through 2D Soft Tissue With Obstacles," *In Proc. of IEEE Int. Conf. on Rob. Autom. (ICRA)*, 2005, pp. 1640-1645.

[62] E. Dehghan, S.E. Salcudean, "Needle Insertion Parameter Optimization for Brachytherapy," *IEEE Trans. Rob.*, vol. 25, no. 2, pp. 303-315, 2009.

[63] S.S. Rao, Vibration of Continuous Systems, John Wiley and Sons Inc.; 2007.

[64] A.C. Ugural, Mechanics of Materials, McGraw-Hill Inc.; 1991.

Chapter 2

A Novel Force Modeling Scheme for Needle Insertion using Multiple Kalman Filters

The material presented in this chapter has been published in IEEE Transactions on Instrumentation and Measurement, vol. 61, no. 2, 2012, pp. 429-438. A part of this work has also been published in the Proceedings of the 32nd Annual International Conference of the IEEE Engineering in Medicine and Biology Society (EMBS), pp. 2292-2295, Argentina, 2010.

2.1   Introduction

Medical intervention using surgical needles is a common minimally invasive procedure. Flexible needles can facilitate curved trajectories, and are utilized for localized drug delivery, radioactive seed placement, neurosurgery, ablation, or tissue biopsy especially in regions that are difficult to access or in deep zones. In this context, robot-assisted needle steering, which is intended to guide the needle to the targeted locations inside soft tissue,

has become an active research area [1]. In this respect, positioning inaccuracy originates from a variety of factors such as i) soft tissue deformation; ii) bending mechanics as a result of tissue-needle interaction; iii) inhomogeneity, nonlinear viscoelasticity, and anisotropy of real organic tissue; iv) target movement due to respiration, heartbeat or similar artifacts, and finally v) tiny anatomic structures which could not be easily detected by conventional imaging modalities.

In therapeutic procedures, if applicable and possible, increasing the amount of steering may improve the accuracy of diagnosis. This is restricted by the amount of steering that can be achieved once the needle is inserted, and usually, the needle divergence from its desired path degrades the effectiveness of the diagnosis or treatment. In this regard, the actual path can be directly linked to the force signals experienced by the needle during penetration. Thus, accurate modeling is the first step towards developing a precise and effective trajectory planning scenario. Ultimately, the force model can be employed either in fully-autonomous motion planning [2, 3] or in a force feedback tele-operation scheme; either to assist a surgeon or as a training simulator [4]. High-fidelity simulators should have the capability to provide realistic haptic perception to the user. In semi-autonomous steering, where the surgeon remains in the loop, a force control approach allows the slave system to insert the needle to the desired penetration depth, and also gives the operator a realistic sense of needle-tissue interaction so that the operator can take further actions.

In case of percutaneous interventions, understanding the contact mechanism between the surgical needle and organs is a complex task. Indeed, environmental features including soft tissue dynamics are important to design the robot-assisted control strategy. During needle-tissue interaction, pre-puncture corresponds to a viscoelastic behavior, and post-puncture interaction forces are due to the combined effects of cutting force, friction, and tissue relaxation. Finally, during retraction or needle withdrawal, friction is the sole interactive force [5]. Identification of the associated properties can be rendered by employing adequate modalities. For instance, detection of abrupt changes in successive layers is captured by a haptic device or by a force/torque sensor. Nevertheless, characterization of the needle-tissue contact forces remains a challenge due to the following reasons [1, 8, 15]:

- The needle penetrates various layers of tissue, e.g., skin, fat, and muscles; and inhomogeneity, nonlinear viscoelasticity, and anisotropy of real organs suggest that the present force cannot be described by a simple structure.

- Biomechanical properties are patient dependent, and linked to the age, gender, disease stage, and needle geometry.

- During insertion, the elementary contributions of the various layers are intermixed.

The main objective of this study is to identify needle-tissue properties during percutaneous interventions; thereby, finding a mathematical model which mimics the translational force behavior. The outcome of this research will provide a means for characterizing the needle-tissue contact forces. The subject of needle insertion involves a substantial biophysical variations to be characterized. Therefore, the physical modeling and direct estimation of these parameters may not be possible. To deal with this problem, we will introduce a nonlinear dynamic model that allows intraoperative data extraction of the force profile. Without explicit investigation of biomechanical aspects, in the following we propose a recursive on-line estimation technique for system identification. The goal of the current work is to find a computationally feasible model that describes the relationship between the total axial force measured at the needle holder and the depth of insertion during both insertion and retraction in soft tissue. The proposed modeling and identification scheme enables us to tune the parameters according to the interaction properties. Consequently, any change in the mentioned properties which leads to a deviation in the insertion or retraction force can be intraoperatively captured by the model.

The outline of this chapter is as follows: In section 2.2, the relevant studies in the area of needle-tissue force modeling are reviewed. Section 2.3 introduces the proposed nonlinear model that can describe needle-tissue interaction in the force domain. In section 2.4, the employed recursive filtering method for system identification is explained while in section 2.5, experimental results and discussions are given. Finally, section 2.6 presents conclusions and suggestions for future work.

2.2 Related Work and Motivation

As a pioneering work for force modeling in needle insertion, Okamura et al. [5] developed an empirical model for unilateral needle insertion force, which was a summation of capsule stiffness force, friction and cutting forces. According to their model, the stiffness force occurs before the puncture of the capsule while the friction and cutting forces occur

right after the main puncture. In [6], interpretation of force features in conjunction with spectroscopic techniques was examined for a needle penetrating soft tissue with the aim of automatically identifying tissue type at the needle tip. Podder et al. [7] derived a statistical model to estimate the maximum force that the needle experienced during prostate brachytherapy. Insertion force data were collected to build their offline model based on i) patient-specific parameters including PSA level, BMI, prostate volume, and ii) procedure specific criteria such as needle size, and insertion velocity. They also quantified and measured *in-vivo* insertion forces while implanting radioactive seeds in the prostate gland [8]. In this empirical study, the overall maximum measured force on 18GA and 17GA needles with respect to velocity was compared.

DiMaio and Salcudean [9] illustrated a system for measuring the extent of planar PVC phantom deformation during needle insertion. They investigated the insertion of a 17GA symmetric epidural needle and then estimated forces applied to the needle shaft using linear elastic Finite Element Method (FEM) and a vision system. Hing et al. [10] developed a system to predict soft tissue movement and involved force components using traditional FEM and ABAQUS software. Two C-ARM Fluoroscopes were used in this study to image fiducial markers and needle bending. Misra et al. [11] also explored the sensitivity of the axial force to tissue rupture toughness, tissue elasticity as well as bevel angle of the needle tip. Using both contact and cohesive zone models, they incorporated these physical parameters into an FEM-based model. Kobayashi et al. [12] developed another model including viscoelastic and nonlinear behavior based on detailed material properties. Using FEM, they validated the relationship between the needle displacement and the insertion force and evaluated its velocity dependency when puncture occurs.

Generally speaking, FEM is accurate and adequate for small linear elastic deformations. However, robot-assisted needle interventions usually deal with deep insertion depths. On the other hand, numerical efficiency of this technique relies on i) the development of effective pre- and post-processing; ii) the material parameters chosen; iii) the scale of deformation, and iv) the algorithm employed for solving the equations of continuum mechanics. Although, researchers have focused efforts on optimizing FEM computational efficiency, it still does not allow for real-time complex simulations or intraoperative planning and control. This is due to the large system of equations involved as well as frequent topological and boundary condition changes that occur as the needle moves into the tissue. In [13], a manual indentation technique and a hand-held probe were proposed to estimate the biome-

chanical behavior of human body parts. This system can provide an initial setting for FEM-based approaches. Another weakness of FEM is the necessity of providing local deformations using markers or beads placed on the surface of or implanted into the material. The estimated movement of the beads is then used to validate the model. Obviously, it is difficult to employ this category of modeling methods in clinical conditions, specially in case of existing internal organs with complex geometries and boundary conditions.

Several studies have looked at alternative modeling methods. Viscoelastic properties of soft tissues can be represented by rheological models composed of serial and/or parallel combinations of springs (elastic elements) and dashpots (viscous elements). The spring-beam-damper model is the most common non-continuum mechanics-based approach used for soft tissue modeling in small scale motions. Despite its limited accuracy, it is efficient for real-time simulations and robot-assisted interventions. Using a set of local polynomials connected in serial finite segments, Yan et al. [14] presented an on-line estimator to approximate the depth-varying tissue parameters through force measurements. Keeping the insertion speed constant, the model was validated inserting an 18GA needle with a trihedral tip. Barbe et al. [15] developed another on-line scheme utilizing recursive least-squares. It was then integrated to the Kelvin-Voigt (KV) viscoelastic interaction model with time-varying parameters to reconstruct the force evolution during insertion. Based on this analysis and possibly due to ignoring friction, an accurate model could not be estimated in an on-line manner. Using the same interaction model, associated parallel spring and dashpot combinations were approximated by a set of piecewise linear functions at a constant insertion velocity [4].

Other important issues on modeling of tool-tissue interaction are still open for future research. Misra et al. [16] reviewed this matter with emphasis on surgical simulations. More aspects of the interaction from a biomechanics view have been reported in [17, 18]. The former paper is an empirical study, and as observed, needle-tissue interaction and associated biomechanical properties are influenced by various factors. Thus, it can be impractical or impossible to measure or investigate the effect of involved parameters separately.

Although it is well-understood that incorporating explicit biomechanical features of soft tissue in estimation and modeling is part of an ideal solution, the intention is to focus on local force measurements to build a dynamic structure. It is worth mentioning that finding accurate physics behind the needle-tissue interaction model as a multi-faceted problem is not deemed a priority here. Perhaps the most significant impediment towards physically-

based modeling is the fact that the contact forces are influenced by complicated biophysical tissue behavior whose description using physical theories is still a challenge. In addition, the mechanism of cutting at the needle tip is not yet well formulated, and distributed friction along the needle shaft that affects the measurements has its own modeling complexities. All these issues motivated us to study a non-physics-based approach as presented in this work.

To the best of our knowledge, no one has ever presented a compact and feasible model to capture both insertion and retraction forces. The importance of finding a computationally efficient model that can partly or fully embody the interaction properties is that it paves the path for focusing more on intraoperative model-based planning or tele-operation techniques that constitute the ultimate objectives in this body of work.

2.3 Reflecting Needle-Tissue Interaction in the Force Domain

Assuming a constant insertion velocity, the total translational force can be dynamically modeled as a function of insertion depth using the following nonlinear state-space model. Thus, the entire interaction which includes insertion and retraction phases can be described by a dynamic model as proposed here.

The main motivation for this selection arose from the fact that the trend describing the total insertion force as a function of penetration depth is identical to the dynamic friction described by the LuGre model [19]. Replacing the velocity in the original LuGre model with the depth of insertion and modifying the measurement equation, the current model enables us to capture an approximation for the force pattern. In this setting, z is an internal state, and l stands for the depth of insertion acting as the model input. f also represents the axial force experienced by the needle, and it is the output of the single-state models as following

2.3.1 Model I

$$
\begin{cases}
\frac{dz}{dt} = l(\beta_0 - \frac{\sigma_0}{g(l)}z) \\
f = \sigma_0 zl + sign(\dot{l})l\{\sigma_1 e^{-\alpha l}(\beta_0 - \frac{\sigma_0}{g(l)}z) + \sigma_2\}
\end{cases}
\tag{2.1}
$$

where,

$$g(l) = f_1 + f_2 e^{-\alpha l} \tag{2.2}$$

As previously shown in [20], the total force measured at the base is characterized by six parameters, namely f_1, f_2, σ_0, σ_1, σ_2, and α in model I. Collectively, the g function, which models the Stribeck effect in the traditional LuGre model, corresponds to the sharp drop in the insertion force once the main puncture occurs here. This function is defined by the following three parameters: f_1, f_2, and α. In (2.1), selecting a smaller value for σ_0 yields a bigger force peak and also a sharper force drop during the rupture. It has almost no impact on the retraction force profile. Changing the value of σ_1 results in the same effect during the insertion regime, but it also shapes the retraction axial force in the vicinity of the entry point. The value of σ_2 directly affects the steady-state value of the generated output, and can remove the oscillation from the simulated force in the backward motion if the filter is properly tuned. β_0 is also a normalized constant.

Note that these parameters are not physically-inspired, and thus their role cannot be individually interpreted. Due to the same reason as well as the combined effect of them on the generated force features, it is not possible to obtain the parameters separately. Instead, the recursive mechanism introduced in section 2.4 allows us to estimate the parameters, update the model, and reconstruct the force pattern during percutaneous interventions.

As a reduced order version of model I, model II is introduced in (2.3). In this structure, the unknown parameters α and f_2 are replaced with their estimated values provided by model I. The new values are respectively named $\tilde{\alpha}$ and $\tilde{f}_2$. Here, a new varying parameter denoted by β is added to (2.1) to achieve a better overall accuracy. Model II is expected to suffer less from numerical issues compared to the previous state-space structure, and it will be discussed in section 2.5.

2.3.2   Model II

$$\begin{cases} \frac{dz}{dt} = l(\beta - \frac{\sigma_0}{g(l)}z) \\ f = \sigma_0 zl + sign(\dot{l})l\{\sigma_1 e^{-\tilde{\alpha}l}(\beta - \frac{\sigma_0}{g(l)}z) + \sigma_2\} \end{cases} \tag{2.3}$$

where,

$$g(l) = f_1 + \tilde{f}_2 e^{-\tilde{\alpha}l} \tag{2.4}$$

Compared to the existing models, in this study no separation is made between axial force components, e.g., rupture, friction, and cutting forces, and the entire intervention including insertion and retraction phases is described by a single set of equations. Herein, the relaxation time has been ignored, and the procedure is desired to be learned in an on-line scheme by the usage of a bank of Kalman filters in a switching process.

2.4 Proposed Sequential Identification Procedure

Having selected one of the proposed models, the associated parameters are required to be experimentally identified. Generally speaking, the parameters that are hardly measurable but observable can be estimated using state-parameter estimation methods. Several studies and discussions have been reported in the literature on adaptive identification of the original LuGre model [19,21,22]. As a modification to this model, in the current work an estimator is realized using a joint state-parameter EKF (extended Kalman filter) technique. Details of the design of a conventional EKF as a widely accepted tool in estimation theory are discussed in [23]. It is assumed here that readers are familiar with discrete Kalman filtering.

To implement the joint state-parameter EKF, the original state vector (z) is augmented with new state variables (θ) which denotes the unknown coefficients of the proposed model [24]. The dynamics of the augmented state is commonly assumed to be of random walk nature which is subject to zero-mean white noise perturbation (ζ). ζ is presumed to be uncorrelated with system noise (υ), and to have a positive definite variance [23].

A 3rd-order Runge-Kutta algorithm is then employed to discretize the state-space representation of the system which includes the continuous force-depth model given in the previous section and the augmentative model. Let the discrete representation of the entire system at the kth instant be formulated as

$$\begin{cases} z^{k+1} = F(z^k, \theta^k, l^k) + \upsilon^k \\ \theta^{k+1} = \theta^k + \zeta^k \\ f^k = H(z^k, \theta^k, l^k) + \omega^k \end{cases} \qquad (2.5)$$

where $\theta_{m \times 1}$ is the vector of model parameters as introduced previously; $\upsilon_{1 \times 1}$ and $\zeta_{m \times 1}$ are the process noise while $\omega_{1 \times 1}$ is the measurement noise. Thus, the stochastic dynamics of
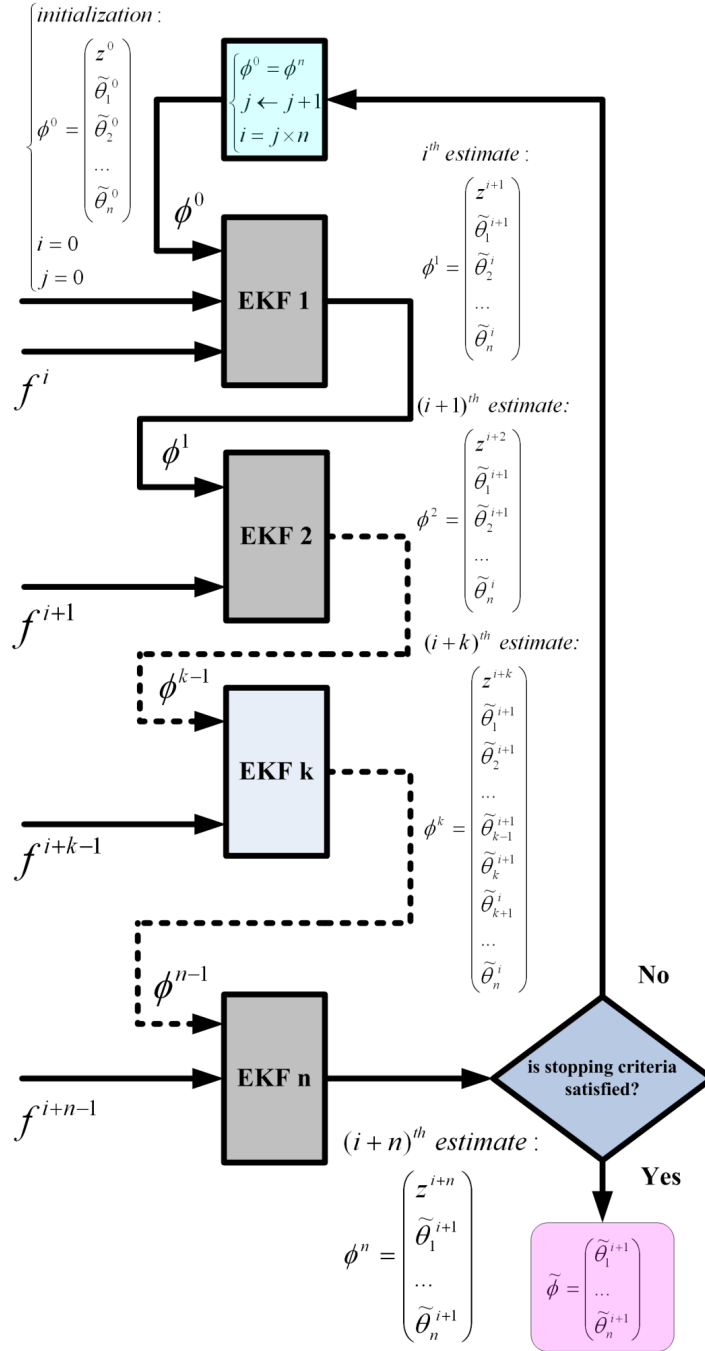
Figure 2.1: Flowchart of the proposed sequential identification procedure.

the interaction force transforms into

$$
\begin{cases}
\phi^{k+1} = \hat{F}(\phi^k, l^k) + \hat{v}^k \\
f^k = H(\phi^k, l^k) + \omega^k
\end{cases}
\tag{2.6}
$$

in that $\hat{v}_{(m+1)\times 1}$ is the process noise of the new state vector (ϕ) which is written as

$$\phi^k_{(m+1)\times 1} \equiv \begin{pmatrix} z^k_{1\times 1} \\ \theta^k_{m\times 1} \end{pmatrix}$$

The multiple EKF is then applied to estimate the augmented state vector which consists of both the original state variables and the augmentative state variables. This approach combines data asynchronously for use by EKFs in a switching mode. In other words, the multiple approach is to alternatively run multiple filters at which a subset of the states in the $\phi_{(m+1)\times 1}$ space is subjected to estimation and the rest of them are treated as known values [25]. The number of states estimated by a single EKF is chosen with respect to the observability properties of (2.6).

Assume that $\tilde{\theta}_n$ $(1 \leq n \leq m)$ denotes a set of vectors, which tessellates $\theta_{m\times 1}$, i.e.,

$$\forall n, q\ (1 \leq n, q \leq m):\ \tilde{\theta}_n \bigcap \tilde{\theta}_q = \emptyset$$

$$\bigcup_{n=1}^{m} \tilde{\theta}_n = \theta_{m\times 1}$$

Each single joint-EKF estimates the unknown vector of $\tilde{\theta}_n$ plus the internal state of the nonlinear dynamics (z) at the current step. Once the estimation is completed at the current iteration, the model is updated with the estimated values, i.e., the estimated vector is fed into the model and then the next filter in the queue is triggered. This procedure is followed iteratively until a narrow error bound as the stopping criteria is achieved. Fig. 2.1 shows the sequence of the estimation procedure as proposed in this study. Finally, $\tilde{\phi}$ represents the estimated value for the unknown parameters. It should be noted that these parameters may have no physical interpretations.

2.5 Implementation and Experiments

2.5.1 Instrumentation

An experimental implementation of the proposed methodology was carried out on the state-of-the-art robotic system [26] described in Appendix A. This system is capable of imple-

menting more advanced approaches; however, it was employed here to validate the pro-
posed modeling scheme. Experiments were carried out on an artificial phantom made from
Gelrite Gellan Gum (Sigma-Aldrich) with two concentration rates in water: 4.5% (tissue A,
less stiff) and 6% (tissue B, more stiff). Based on the experiments and experience, this pow-
der simulates a uniform elastic environment, and mimics the frictional effects of biological
tissues better than rubber phantoms. Compared to live tissues in which water comprises a
considerable portion of the phantom, rubber-made artificial phantoms consist of a smaller
number of water molecules, and that is why they generate an exaggerated amount of fric-
tion. The employed gum powder in this study created a more watery phantom that made
the experiments more realistic in terms of the measured force ranges and viscosity. In order
to get more consistent results, the room temperature must be controlled carefully. Keeping
the phantom in the refrigerator for a few days leads to creating a thin crust on the tissue
surface which acts as a membrane. In this test-bed, two sizes of stainless steel needle (Cook
Medical) were used; the cannula of an 18GA needle (needle A, less flexible) with outer and
inner diameters of 1.270mm and 0.838mm, and the cannula of a 22GA needle (needle B,
more flexible) with outer and inner diameters of 0.718mm and 0.413mm, respectively.

2.5.2 Experimental Results

It is presumed that the insertion trajectory is of linear segment with parabolic blend (LSPB)
with a preset velocity of the linear segment. The contact force was modeled under this con-
stant speed assumption. Fig. 2.2 shows a sample of the recorded force and depth profiles.
Note that while exciting the system within a limited range of frequencies does not reveal all
dynamic features, applying such a low-band signal was inevitable. Robot-assisted prostate
brachytherapy entails a very similar insertion velocity profile, and one of the goals was to
identify force-depth parameters in a clinical condition.

Selecting the proper number of filters and state pairing are challenging tasks that affect the
convergence rate, and a wrong selection can lead to instability in extreme cases. Based on
the simulation studies and taking into account the observability properties of the system,
three EKFs were employed in parallel according to the definitions given in Table 2.1. It is
notable that the reported results in this section are the outcomes of multiple experiments
repeated under the same test conditions at different insertion points.

Each individual EKFs were tuned. To this effect, the initial error covariance matrices were
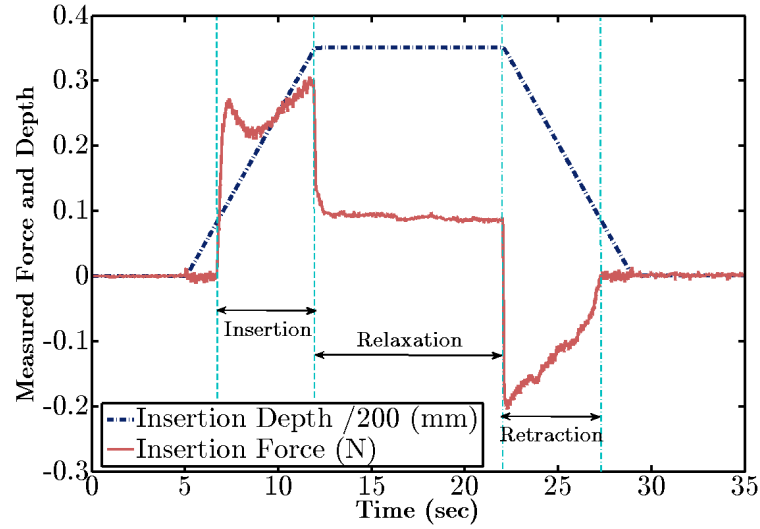
Figure 2.2: Typical force and depth profiles during needle insertion into a homogeneous phantom (needle A/tissue A, insertion velocity=10mm/s).

Table 2.1: Filter Definition

applied model	filter number	$\tilde{\theta}_i$	$Q(\tilde{\theta}_i)$
I	$i = 1$	(f_2, σ_0)	$0.05 \times diag(10^5, 10^9)$
	$i = 2$	(f_1, σ_1)	$0.05 \times diag(10^{15}, 10^{15})$
	$i = 3$	(α, σ_2)	$0.05 \times diag(10^5, 10^{15})$
II	$i = 1$	σ_0	0.05×10^9
	$i = 2$	(f_1, σ_1)	$0.05 \times diag(10^{15}, 10^{15})$
	$i = 3$	(β, σ_2)	$0.05 \times diag(10^3, 10^{15})$

chosen to be large in order to ensure rapid convergence. However, not much improvement were achieved for the diagonal magnitudes larger than 10^{15}. The system noise covariance matrices or $Q(\tilde{\theta}_i)$ representing the level of uncertainty in each sub-space were set as in Table 2.1 in which index i refers to the subspace number. The measurement noise variance or R was also set to be 0.01 in each filter. This selection is a matter of a few trials and errors, and the noise patterns are assumed to be time-invariant. In some studies, the initial values for the parameters are chosen very close to the estimated ones although it is believed that this selection may result in an observability problem. In this study, $\tilde{\phi}_0$ was set to be within $\pm 500\%$ of the estimated value of $\tilde{\phi}$ provided by the first run of the algorithm. Due to the highly nonlinear structure of the proposed model(s)/estimator, assuming a completely random initial state may result in either divergence or getting stuck in local minima.

Table 2.2: RMSE of the Proposed Estimator (N)

	including initial transition		
applied model	insertion phase	retraction phase	entire profile
I	1.68×10^{-1}	3.25×10^{-2}	1.21×10^{-1}
II	6.63×10^{-2}	2.09×10^{-2}	2×10^{-2}
	excluding initial transition		
applied model	insertion phase	retraction phase	entire profile
I	1.81×10^{-2}	1.71×10^{-2}	2.03×10^{-2}
II	3.44×10^{-3}	2.83×10^{-3}	3.9×10^{-3}

Inserting the needle according to the profile shown in Fig. 2.2, the models introduced in section 2.3, and in conjunction with the proposed on-line estimation technique exhibited the following performance. For this test, the combination of needle A plus tissue A was selected. Fig. 2.3 depicts the estimated force during the insertion phase while Fig. 2.4 compares the estimated values and measured forces in the retraction stage. As shown in Fig. 2.3(a), the filter response is oscillatory especially during the pre-puncture stage. Large transitions in the estimated values are also visible at the beginning of both insertion and retraction. Moreover, according to Fig. 2.4(a), during the retraction and in the vicinity of the entry point, model I exhibits poor estimation performance.

Root mean squared error (RMSE) is proposed here as a means of assessing the estimation quality. To this end, numerical results of the previous test are listed in Table 2.2. The error values listed in the first half of the table include the entire insertion depth while in the second half, the first five samples of both insertion and retraction data were intentionally ignored. Focusing more on the steady-state response, the second set of the reported values are, therefore, less affected by the initial oscillatory behavior of the estimator. Comparing estimated signals shown in Figs. 2.3 and 2.4 and numerical values reported in Table 2.2 verifies that model II outperforms model I.

As observed, the proposed scheme enables us to express the axial force during needle-tissue interaction by estimating a set of parameters $(\tilde{\phi})$. As a rule of thumb, provided that the sequence of estimated values lies within the corresponding $\pm 3\sigma$ limits, the estimation is statistically confident where σ denotes the standard deviation. Thus, to further investigate, a track of $\pm 3\sigma$ values was sequentially computed in each run.
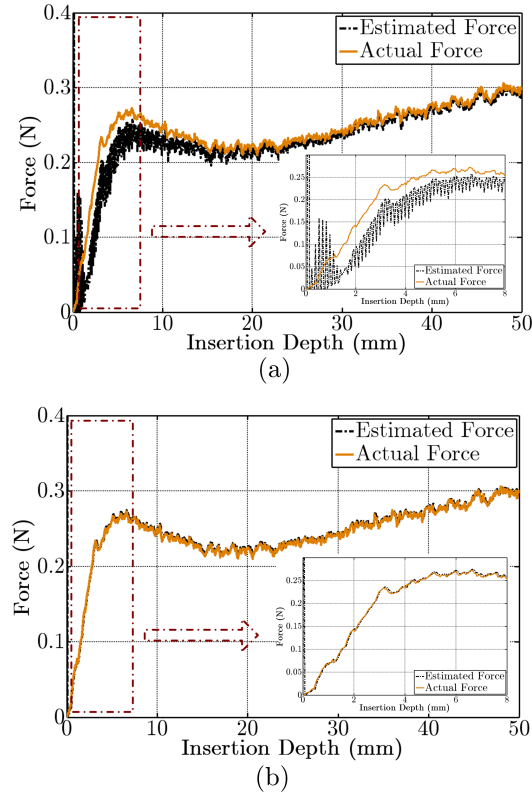
Figure 2.3: On-line force estimation during insertion using needle A/tissue A (insertion velocity=10 mm/s) (a) model I (b) model II.

Fig. 2.5 shows the estimated values for z, σ_2, σ_0 and f_2 of model I within the first 50 millimeters of insertion depth. Fig. 2.6 also demonstrates the estimation results using model II in the same scenario at two examined speeds. Herein, σ_2, f_1 and β were selected for visualization. For the parameter α, it was noticed that in the conducted experiments, the estimation starts to be dominated by noise from a middle point during the insertion process. Although being observable, the contribution of α in the model's output diminishes as the value of l increases, and this effect could not be improved by changing the associated noise parameter. Hence, to have less dependency on the noise characteristics, the value of α was assumed to be constant from the aforementioned point onward. This strategy resulted in more stable practical results; however, this observation led to adopting model II in which this parameter was omitted.

By comparison, estimation of σ_0 and σ_2 has the lowest confidence level and convergence rate, respectively, as shown in Fig. 2.5. In the same figure, rupture appears to be informative for the identification procedure, although inherent lack of excitation in the system avoids
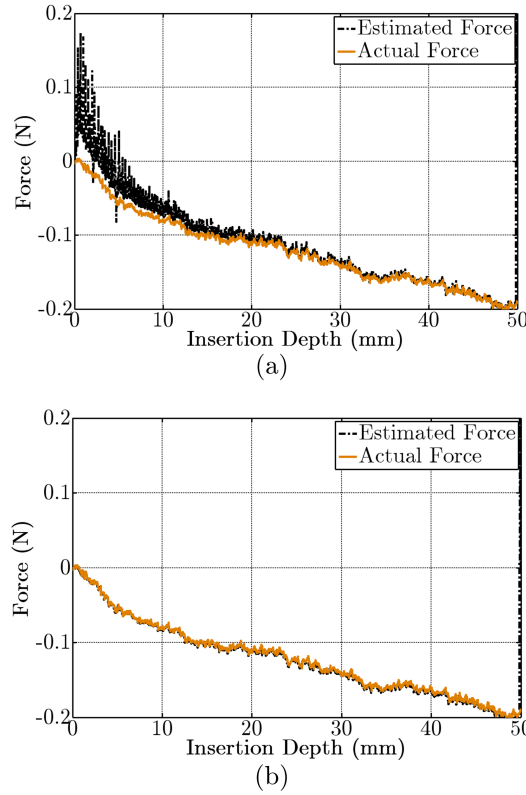
Figure 2.4: On-line force estimation during retraction using needle A/tissue A (insertion velocity=10mm/s) (a) model I (b) model II.

fast convergence. This problem can be partially resolved by injecting more noise into the state-space model that yields the selected $Q(\tilde{\theta})$ matrices in Table 2.1. As emphasized previously, in order to have a realistic approach that can capture force-depth cycle during a clinical procedure, a low-velocity LSBP profile was applied. Note that needle insertion rates usually vary between 0.4mm/s and 10mm/s in clinical practice [9].

Next, the insertion velocity was reduced to 6mm/s. As depicted in Fig. 2.6 and in general, model II resulted in a more confident estimation in terms of retaining $\pm 3\sigma$ limits at the lower examined velocity. To make a fair comparison, both filters were triggered from the same initial conditions. The force pattern relies on the insertion velocity thus the parameters settle down at different values at the end of conducted experiments. As observed, the convergence rate and confidence level for a particular parameter are dependent on the velocity and the model employed, but model II outperforms model I according to Figs. 2.3 and 2.4.

For the final evaluation, model II was employed to simulate the force-length mapping using
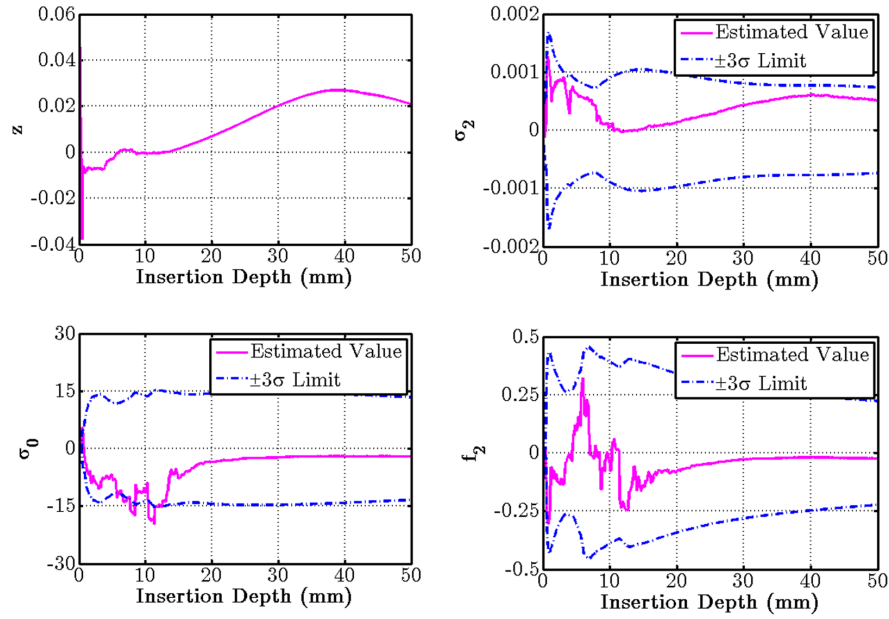
Figure 2.5: State-parameter estimation during insertion using needle A/tissue A and model I (insertion velocity=10mm/s).

steady-state values of the parameters estimated in the previous step. Setting the speed to be 10mm/s, the force profile was plotted using (2.3) and the following nominal values: $\sigma_0 = 7.9 \times 10^{-3}$, $\sigma_1 = 2.46$, $\sigma_2 = 4.14 \times 10^{-3}$, $f_1 = 5.59 \times 10^{-2}$, and $\beta = 2.55 \times 10^{-2}$. Note that the values of $\tilde{f}_2$ and $\tilde{\alpha}$ were already set to be -2.11×10^{-2} and 5.25×10^{-2}, respectively. The same simulation was repeated by plugging the following parameters into model II at 6mm/s: $\sigma_0 = 3.91 \times 10^{-3}$, $\sigma_1 = 2.25$, $\sigma_2 = 3.55 \times 10^{-3}$, $f_1 = 3.25 \times 10^{-2}$, $\beta = 2.43 \times 10^{-2}$, $\tilde{f}_2 = -1.17 \times 10^{-2}$, and $\tilde{\alpha} = 3.63 \times 10^{-2}$.

It is evident from Figs. 2.7(a) and 2.7(b) that this strategy provides a means to capture the entire insertion-retraction loop without having *a priori* information about the phantom's biophysical properties as well as the needle geometry. Mean absolute error values in the studied cases in Fig. 2.7 were respectively calculated to be 9.87mN and 7.52mN.

Now, in order to thoroughly evaluate the work, the same experiments were carried out for other needle-tissue combinations, i.e., needle A/tissue B, needle B/tissue A, and needle B/tissue B. Fig. 2.8 shows parameter estimation using model II and the combination of needle B and tissue B during the 80 millimeters of insertion. Fig. 2.9 also compares the measured force-depth cycles with the estimated ones using steady-state values of the estimated parameters, and Table 2.3 summarizes the steady-state parametric values in three
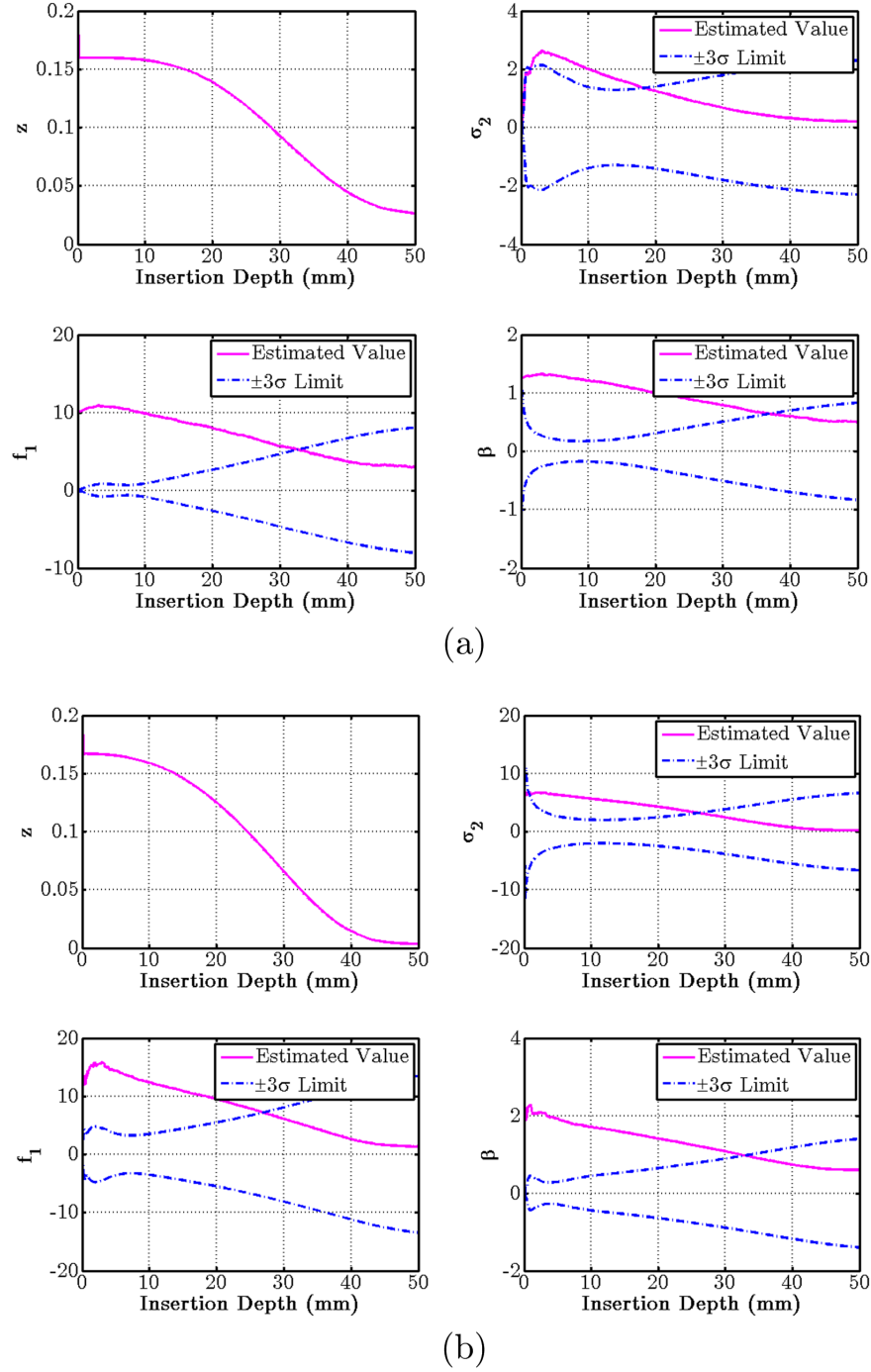
Figure 2.6: State-parameter estimation during insertion using needle A/tissue A and model II (a) insertion velocity=10mm/s (b) insertion velocity=6mm/s.

sets of conducted experiments with the tinier needle. Inserting this needle at 6mm/s was excluded from performed studies due to the fact that force measurements were noisy and

(a)

(b)
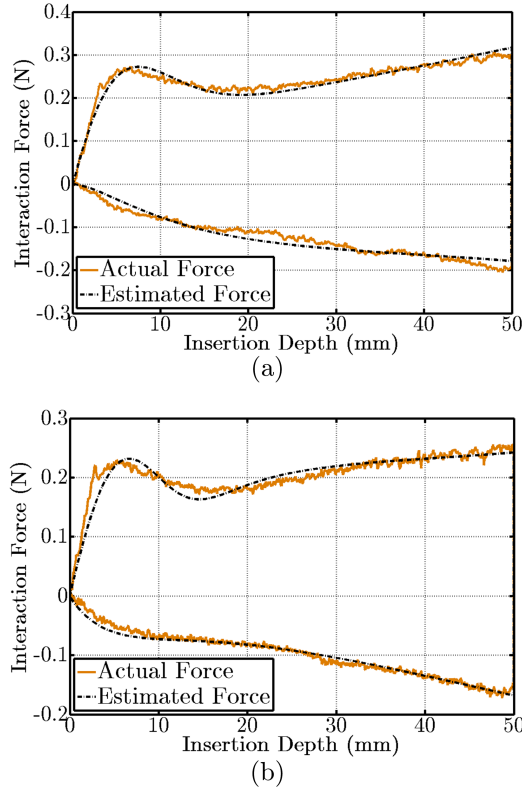
Figure 2.7: Interaction force profile using model II, needle A/tissue A, and steady-state values of the estimated parameters (a) insertion velocity=10mm/s (b) insertion velocity=6mm/s.

Table 2.3: Steady-state Values of the Estimated Parameters using Model II and Needle B

	tissue B v=10 mm/s	tissue B v=6 mm/s	tissue A v=10 mm/s
σ_0	9.2×10^{-4}	8.37×10^{-4}	7.96×10^{-4}
σ_1	4.48×10^{-1}	9.27×10^{-1}	5.35×10^{-1}
σ_2	1.63×10^{-3}	1.79×10^{-3}	7.63×10^{-4}
f_1	2.7×10^{-2}	9.21×10^{-3}	2.15×10^{-2}
$\tilde{f}_2$	-9.96×10^{-3}	2.49×10^{-1}	-1.19×10^{-2}
$\tilde{\alpha}$	1.11×10^{-2}	5.84×10^{-2}	1.08×10^{-2}
β	1.53×10^{-2}	1.36×10^{-2}	1.58×10^{-2}

comparable to the force sensor's resolution. Existence of intricate friction in the internal structure of the robot which is too complex to be fully compensated for by the Proportional-Integral-Derivative (PID) controller to provide a smooth motion is a stumbling block using low-velocity profiles.
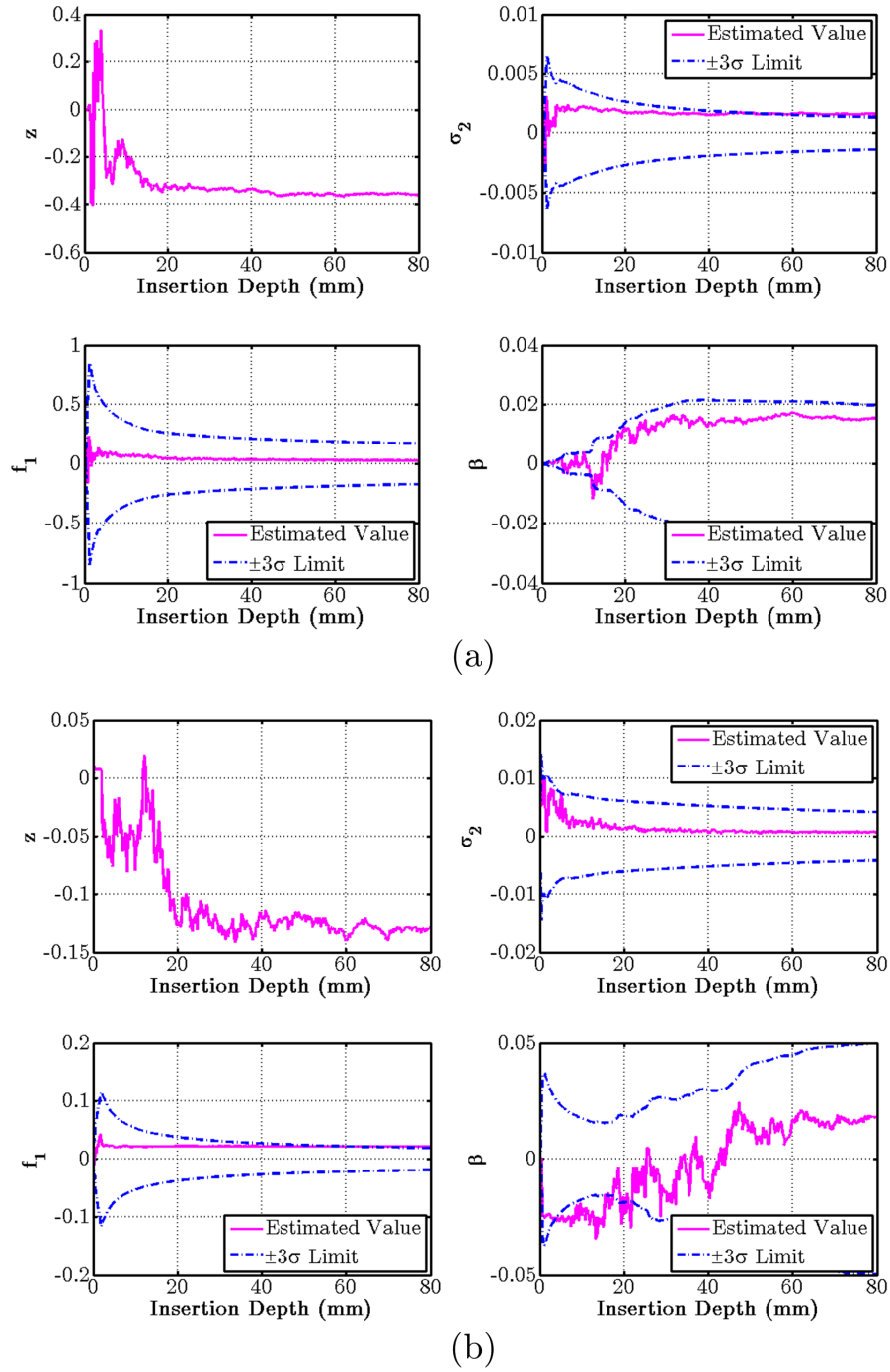
Figure 2.8: State-parameter estimation during insertion using model II at 10mm/s (a) needle B/tissue B (b) needle B/tissue A.

Note that the electromagnetic (EM) tracker measures the needle bending from its initial straight path. The inserted length of the needle is also known using forward kinematics
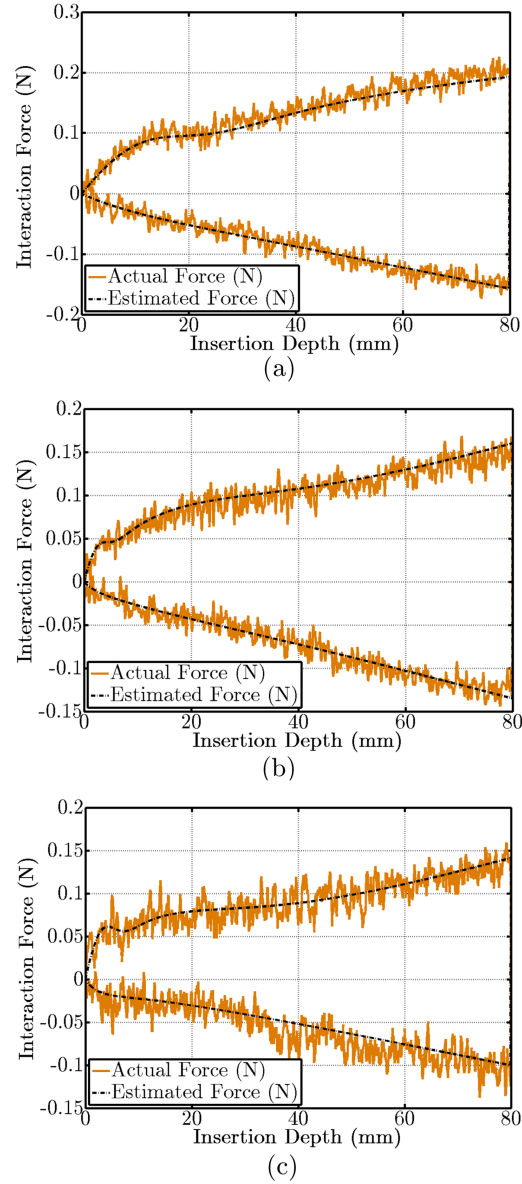
Figure 2.9: Interaction force profile using model II, and steady-state values of the estimated parameters (a) needle B/tissue B, insertion velocity=10mm/s (b) needle B/tissue B, insertion velocity=6mm/s (c) needle B/tissue A, insertion velocity=10mm/s.

of the robot. Thus, the inserted depth can be easily approximated and used in the force-depth model. In these experiments, the maximum deflection measured by the EM tracker at 50 millimeters of insertion depth for needle A/tissue A varied from 4.20mm to 4.38mm whereas for the combination of needle B and tissue A, the deflection amount was limited to 6.62mm.

As observed in Figs. 2.8(a) and 2.8(b), σ_2 and f_1 exhibited a marginal confidence level. In addition, apart from β whose convergence rate in both figures is relatively low, other parameters converged faster compared to the counterpart experiments performed with the 18GA needle. Mean absolute of force estimation errors using steady-state parameters in the three studied cases shown in Fig. 2.9 were also 9.27mN, 9.41mN, and 11.02mN, respectively. It is worthwhile noting that in practice it was not easy to make a purely homogeneous phantom using gum powder. There always existed some air bubbles in the entire volume of the phantom which prevented the elastic medium from being completely uniform, and added unexpected force oscillations to the measured data set. Due to the lower stiffness (or greater flexibility) of the 22GA needle compared to the 18GA one, needle B was susceptible to the effect of air bubbles as observed in the experiments.

To conclude, the proposed on-line mechanism for tuning the filter allows us to minimize the error between the measured and the estimated axial force instead of accurate parameter estimation. In other words, even in a homogeneous environment, the estimated coefficients can be slightly different depending on the maximum penetration depth or applied trajectory. A critical point that has to be noticed is that the convergence rate of each parameter relies on a variety of factors including insertion velocity, state pairing, initial adjustment, and the selected needle-tissue combination.

To illustrate this fact, the initial value of f_2 in the experiments using needle A/tissue A combination was switched to -0.01 instead of 0.01. For a long insertion depth at 10 mm/s, the filter tended to be unstable. Then, σ_0 and σ_2 in model II were paired together and β was treated as a single parameter in the filter bank as opposed to the initial setting described in Table 2.1. As the results confirmed, the convergence was very slow and considerably dominated by the system noise. Note that, it is a complex task to draw a solid conclusion on the model's sensitivity with respect to the initial values selection. Therefore, achieving optimal performance and improving the convergence rate and robustness require a more intricate strategy to tune the bank of filter and is left for future work. In general, optimal tuning can be a complicated task in estimation theory, and it is an area of challenge.

2.6 Conclusions and Future Work

In this chapter, the application of asynchronous joint-EKF in needle insertion was studied. In summary, it is a complex task to find an explicit mapping between existing variables and

measured force profile during needle-tissue interaction, and the sheer complexity of the physics behind it led us to seek a non-physics-based approach. Most of the current models reported in the literature are not implementable in operating conditions. For instance, while FEM is well suited to compute accurate and complex deformation of soft tissue, it is difficult to achieve a perfect real-time performance even on a moderately powerful workstation [1,16]. From this point of view, successful parameter identification from intraoperative data stream during a conventional medical procedure is a remarkable advantage.

This study presented a method that is particularly important for needle-based interventions performed using a robotic system where no imaging data is available throughout the operation. As the needle interacts with an elastic medium, the force-depth measurements provide a useful guide to characterize force evolution. The axial interaction force was described using a nonlinear state-space model, and associated parameters were intraoperatively identified. Hence, explicit knowledge of needle and tissue properties was not required prior to experimentations. Another achievement in this study was to describe the entire axial force without i) separating the measured force to its constituent components including rupture, friction, and cutting forces; and ii) using preoperative curve fitting or least-squares methods. Although existing parameters in this model can not be intuitively interpreted, the presented single-state model holds appeal due to its simplicity and real-time implementation. From the experiments, we can conclude that the proposed modeling strategy is feasible and efficient. Consequently, it is possible to make an atlas for a variety of needle-tissue combinations, and then take advantage of the proposed scheme in the absence of the force/torque sensor in order to have an approximation of the total translational force.

We plan to investigate the performance of the proposed scheme using a multi-layer phantom which mimics the behavior of a live tissue during percutaneous therapies. To this end, each layer consisting of a membrane plus a rigid body can be represented by the proposed model and a set of parameters in the force domain. Model validation during *in-vivo* experiments and in the presence of vascular pressure and temperature effects is left for future work. Finally, ongoing work is concerned with integration of the force estimator with a steering mechanism to provide more accuracy and robustness. In [2,3], while assuming a constant radius of curvature for steering, no force feedback was utilized to update the needle curvature. Applying an adaptive approach can be the first step to enhance the overall performance in robot-assisted needle insertion or force control in a haptic system.

Bibliography

[1] N. Abolhassani, R. Patel, and M. Moallem, "Needle Insertion into Soft Tissue: A Survey," *Med. Eng. Phys.*, vol. 29, pp. 413-431, 2007.

[2] K.B. Reed, V. Kallem, R. Alterovitz, K. Goldberg, A.M. Okamura, and N.J. Cowan, "Integrated Planning and Image-Guided Control for Planar Needle Steering," *In Proc of 2nd Biennial IEEE/RAS-EMBS Int. Conf. on Biomedical Robotics and Biomechatronics*, 2008, pp. 819-824.

[3] A. Asadian, M.R. Kermani, and R.V. Patel, "Robot-Assisted Needle Steering Using a Control Theoretic Approach," *J. Intell. Robot. Syst.*, vol. 62, no. 3-4, pp. 397-418, 2011.

[4] P.L. Yen, R. Hibberd, and B. Davies, "A Telemanipulator System as an Assistant and Training Tool for Penetrating Soft Tissue," *Mechatronics*, vol. 6, no. 4, pp. 377-489, 1996.

[5] A.M. Okamura, C. Simone, and M.D. O'Leary, "Force Modeling for Needle Insertion into Soft Tissue," *IEEE Trans. Biomed. Eng.*, vol. 51, no. 10, pp. 1707-1716, 2004.

[6] P.N. Brett, A.J. Harrison, and T.A. Thomas, "Schemes for the Identification of Tissue Types and Boundaries at the Tool Point for Surgical Needles," *IEEE Trans. Inf. Technol. Biomed.*, vol. 4, no. 1, pp. 30-36, 2000.

[7] T.K. Podder, J. Sherman, E.M. Messing, D.J. Rubens, D. Fuller, J.G. Strang, R.A. Brasacchio, and Y. Yu, "Needle Insertion Force Estimation Model Using Procedure-specific and Patient-specific Criteria," *In Proc of 28th IEEE EMBS Annu. Int. Conf.*, 2006, pp. 555-558.

[8] T.K. Podder, J. Sherman, D. Fuller, E.M. Messing, D.J. Rubens, J.G. Strang, R.A. Brasacchio, and Y. Yu, "In Vivo Measurement of Surgical Needle Intervention Parameters: A Pilot Study," *In Proc of 28th IEEE EMBS Annu. Int. Conf.*, 2006, pp. 3652-3655.

[9] S.P. DiMaio, S.E. Salcudean, "Needle Insertion Modeling and Simulation," *IEEE Trans. Robot. Autom.*, vol. 19, no. 5, pp. 864-875, 2003.

[10] J.T. Hing, A.D. Brooks, and J.P. Desai, "Reality-based Estimation of Needle and Soft Tissue Interaction for Accurate Haptic Feedback in Prostate Brachytherapy Simulation," *Springer Tracts in Advanced Robotics*, vol. 28, pp. 34-48, 2007.

[11] S. Misra, K.B. Reed, A.S. Douglas, K.T. Ramesh, and A.M. Okamura, "Needle-Tissue Interaction Forces for Bevel-Tip Steerable Needles", *In Proc of 2nd Biennial IEEE/RAS-EMBS Int. Conf. on Biomedical Robotics and Biomechatronics*, 2008, pp. 224-231.

[12] Y. Kobayashi, A. Onishi, H. Watanabe, T. Hoshi, K. Kawamura, and M.G. Fujie, "In Vitro Validation of Viscoelastic and Nonlinear Physical Model of Liver for Needle Insertion Simulation," *In Proc of 2nd Biennial IEEE/RAS-EMBS Int. Conf. on Biomedical Robotics and Biomechatronics*, 2008, pp. 469-476.

[13] M.H. Lu, W. Yu, Q.H. Huang, Y.P. Huang, and Y.P. Zheng, "A Hand-Held Indentation System for the Assessment of Mechanical Properties of Soft Tissues in Vivo," *IEEE Trans. Instrum. Meas.*, vol. 58, no. 9, pp. 3079-3085, 2009.

[14] K.G. Yan , T. Podder, Y. Yu, T. Liu, and C.W.S. Cheng, "Flexible Needle-Tissue Interaction Modeling with Depth-Varying Mean Parameter: Preliminary Study," *IEEE Trans. Biomed. Eng.*, vol. 56, no. 2, pp. 255-262, 2010.

[15] L. Barbe, B. Bayle, and M. de Mathelin, "In Vivo Model Estimation and Haptic Characterization of Needle Insertions," *Int. J. Rob. Res.*, vol. 26, no. 11-12, pp. 1283-1301, 2007.

[16] S. Misra, K.T. Ramesh, and A.M. Okamura, "Modeling of Tool-Tissue Interactions for Computer-based Surgical Simulation: A Literature Review," *Presence-Teleop. Virt.*, vol. 17, no. 5, pp. 463-491, 2008.

[17] J.T. Hing, A.D. Brooks, and J.P. Desai, "A Biplanar Fluoroscopic Approach for the Measurement, Modeling, and Simulation of Needle and Soft Tissue Interaction," *Med. Image Anal.*, vol. 11, pp. 62-78, 2007.

[18] H. Delingette, "Towards Realistic Soft Tissue Modeling in Medical Simulation," *In Proc. of the IEEE Special Issue on Surgery Simulation*, vol. 85, no. 3, pp. 512-523, 1998.

[19] M.R. Kermani, R.V. Patel, and M. Moallem, "Friction Identification and Compensation in Robotic Manipulators," *IEEE Trans. Instrum. Meas.*, vol. 56, no. 6, pp. 2346-2353, 2006.

[20] A. Asadian, M.R. Kermani, and R.V. Patel, "A Compact Dynamic Force Model for Needle-Tissue Interaction," *In Proc of 32nd IEEE EMBS Annu. Int. Conf.*, 2010, pp. 2292-2295.

[21] L.R. Ray, A. Ramasubramanian, and J. Townsend, "Adaptive Friction Compensation Using Extended Kalman-Bucy Filter Friction Estimation," *Control Eng. Pract.*, vol. 9, pp. 169-179, 2001.

[22] P. Lichinsky, C. Canudas De Wit, and G.C. Morel, "Friction Compensation for an Industrial Hydraulic Robot," *IEEE Control Syst. Mag.*, vol. 19, no. 1, pp. 25-32, 1999.

[23] C.K. Chui, and G. Chen, Kalman Filtering with Real-Time Applications, Edition 4, Springer Berlin Heidelberg; 2008.

[24] P. Moireau, D. Chapelle, and P.L. Tallec, "Joint State and Parameter Estimation for Distributed Mechanical Systems," *Comput. Methods Appl. Mech. Engrg.*, no. 197, pp. 659-677, 2008.

[25] L.P. Yan, B.S. Liua, and D.H. Zhou, "The Modeling and Estimation of Asynchronous Multirate Multisensor Dynamic Systems," *Aerosp. Sci. Technol.*, no. 10, pp. 63-71, 2006.

[26] H.S. Bassan, R.V. Patel, and M. Moallem, "A Novel Manipulator for Percutaneous Needle Insertion: Design and Experimentation," *IEEE/ASME Trans. Mechatron.*, vol. 14, no. 6, pp. 746-761, 2009.

Chapter 3

Dynamics of Translational Friction in Needle-Tissue Interaction During Needle Insertion

The material presented in this chapter has been submitted to the Annals in Biomedical Engineering (Springer Verlag), 2013, and is currently under peer review. A part of this work has also been published in Proceedings of IEEE International Conference on Robotics and Automation (ICRA), pp. 1896-1901, China, 2011.

3.1 Introduction

Flexible needles that can facilitate curved trajectories are of importance in a number of percutaneous applications: brachytherapy, anaesthesia, tissue/fluid sampling, ablation, neurosurgery, and deep brain stimulation particularly in regions that are difficult to access. However, precise placement of a needle tip is a difficult task, and deviation of the needle tip from its intended target area can degrade the effectiveness of the therapy, lead to misdiagnosis or tissue damage. Thus, accurate and dexterous targeting is important in per-

cutaneous procedures, and robotics-assisted needle steering for tip positioning at specific targets inside soft tissue has become an active research area [1].

In order to design a needle steering strategy, the needle is likely to be stopped or slowed down and then rotated before further insertions [2, 3]. Thus, the interaction between the needle and living tissue which is velocity-dependant and includes frictional features has to be thoroughly studied. In this chapter, we formulate a model of translational friction so as to investigate the dynamic behavior of distributed friction along the contact patch when the needle interacts with an elastic medium. In the future, adding full frictional components as developed in this chapter to real-time beam-based bending models [2, 6], and incorporating the deflection mechanism into path planners [2–5] are expected to yield better needle steering. This will allow the guidance of highly steerable needles or needle-like structures with enhanced steerability. This is the main motivation for the current study.

Several studies have been performed dealing with the measurement and the modeling of force components involved in needle-tissue interaction while a comprehensive analytical model for distributed friction in percutaneous interventions is lacked. Misra et al. [7] provided an extensive review on tool-tissue interaction, and van Gerwen et al. [8] presented a comprehensive survey of the empirical aspects of needle-tissue interaction forces. As a pioneering study for force modeling in needle insertion, Okamura et al. [9] proposed an empirical force model based on which the total insertion force was composed of capsule stiffness force, friction and cutting forces. In this study, friction was described by a modified Karnopp model which was comprised of a viscous term plus a constant static friction within a dead zone in the vicinity of zero. Asadian et al. [10] introduced a compact nonlinear dynamic model plus a feasible identification procedure to model the total axial insertion force in terms of the insertion depth. Kataoka et al. [11] measured the involved forces and analyzed them qualitatively without any explicit quantification, and Podder et al. [12] derived a statistical model to estimate the maximum insertion force during prostate brachytherapy. In [13], Barbe et al. employed the Kelvin-Voigt (KV) model in order to reconstruct force evolution during needle insertion. Based on their results and possibly due to ignoring frictional terms, an accurate bio-mechanical model could not be found in an on-line manner. Hing et al. [14] predicted the insertion force by relating needle-tissue interaction force to tissue deformation, and using a linear elastic finite element method (FEM). This analysis led to extraction of important parameters for modeling tissue puncture and relaxation, but not for friction. In [2] the translational friction along the insertion depth

was ignored in order to present a static model for needle deflection. The results were relatively convincing. However, the assumption is not valid when the needle is very flexible, or frictional effects are significant. Ignoring the impact of friction, Webster et al. [15] also developed an experimental bending model for insertion a flexible bevel-tip needle in stiff rubber. This concept of fitting a constant curvature to the needle path was then employed to guide the needle [3,5].

In general, research on systems with friction has a long and rich history [16]. At this point, the complexity of the friction mechanism in needle insertion deserves further detailed examination to develop a feasible solution. In [6,17], and in the context of bending modeling, only the viscous translational friction was studied. With regard to rotational friction, Reed et al. [18] developed a mechanics-based approach using the KV interaction model, FEM, and the Karnopp friction model to predict the tip lag for a rotating needle inside tissue. In the current work as an extension of the preliminary work [19], we will study the translational frictional force in needle insertion. The essence of this approach is inspired by the physically-based method presented by Canudas et al. [20] for modeling longitudinal road-tire interaction in ground vehicles. In this study, we develop a solution that is feasible to implement, and is well suited for interventional procedures.

The remainder of this chapter is organized as follows. In section 3.2, the proposed methodology is described while section 3.3 introduces the test-bed followed by experimental evaluation in section 3.4. Finally, section 3.5 presents conclusions and suggestions for future work.

3.2 The Proposed LuGre-based Structures

Several studies have explored different aspects of friction, and numerous models have been developed to account for it [16, 20, 21]. Friction does not have an instantaneous response, but has internal dynamics. That is why dynamic models such as the LuGre model have been widely discussed in the literature [16, 20, 21], and extensively applied to robotic applications [22]. The conventional point LuGre model [16, 21] can be extended to a distributed version along the inserted portion of the needle (the area of contact or patch) in the following. To this end, let $z(\zeta, t)$ denote the model's internal state or the deflection of the bristle elements located at the longitudinal position ζ at a certain time t. Fig. 3.1 also helps
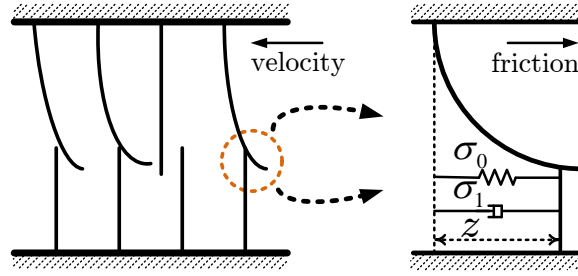
Figure 3.1: Microscopic representation of irregular contact surfaces and elastic bristles whose bending gives rise to the distributed friction.

us to get more insight into the principle of this model which is based on the deflection of spring-like bristles at the microscopic level of moving surfaces. The governing equation is, therefore, written as follows [20]:

$$
\begin{cases}
\frac{dz}{dt}(\zeta, t) = v - \frac{\sigma_0 |v|}{g(v)} z \\
F_{friction}(t) = \int_0^{L(t)} dF(\zeta, t)
\end{cases}
\tag{3.1}
$$

$$
g(v) = \mu_c + (\mu_s - \mu_c) e^{-\alpha |v|^\gamma}
\tag{3.2}
$$

$$
dF(\zeta, t) = \{\sigma_0 z(\zeta, t) + \sigma_1 \frac{\partial z}{\partial t}(\zeta, t) + \sigma_2 v\} dF_n(\zeta, t)
\tag{3.3}
$$

where $dF(\zeta, t)$ is the differential friction force developed in the element $d\zeta$, and $dF_n(\zeta, t)$ is the differential normal force applied to the same element at time t. Herein, v is the contact velocity of each differential element, and L is the current insertion distance.

As observed, the total contact friction in (3.1) is characterized by five static coefficients namely μ_c, μ_s, σ_2, α, and γ, and two dynamic parameters: σ_0 and σ_1. σ_0 can be understood as being the stiffness coefficient of the microscopic deformations during the pre-sliding displacement, and σ_1 as being the damping coefficient associated with $\dot{z}$. σ_2 is the viscous relative damping while μ_c and μ_s are the normalized Coulomb and stiction friction, respectively. The function g also generates the classical Stribeck effect in which the parameter γ is used to achieve desirable steady-state behavior. For more details, see [21]. In the following and prior to experimental validation, we derive three versions of the sought translational friction model during needle insertion.

Assuming a steady-state normal force distribution and introducing a normal force inten-
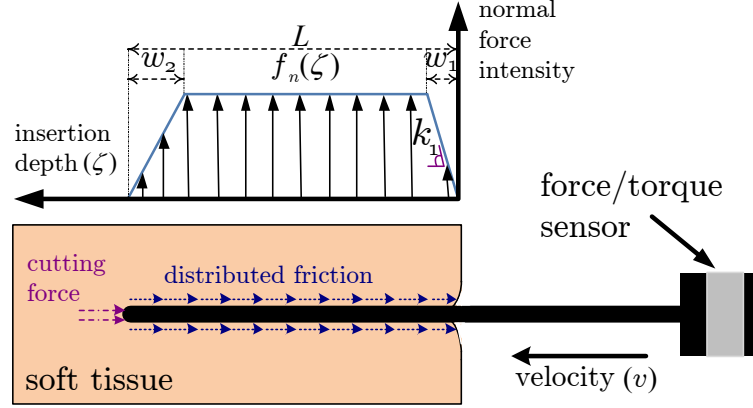
Figure 3.2: Macroscopic representation of needle-tissue interaction and involved force components with a fully trapezoidal force intensity distribution.

sity function $f_n(\zeta)$ (force per unit length) along the patch as shown in Fig. 3.2, we have $dF_n(\zeta, t) = dF_n(\zeta) = f_n(\zeta)d\zeta$. Note that the friction force acts on the side wall of the needle shaft in the axial direction while the clamping force is applied in the normal direction. The latter force is the impact of tissue resistance, and is influenced by the incision shape created by the needle tip and its size as well as the tissue elasticity. The cutting force is separately treated as a concentrated load at the tip [9] that is beyond the scope of this discussion. Thus, the tangential friction force is given by

$$F_{friction}(t) = \int_0^{L(t)} \{\sigma_0 z(\zeta, t) + \sigma_1 \frac{\partial z}{\partial t}(\zeta, t) + \sigma_2 v\} f_n(\zeta)d\zeta \tag{3.4}$$

Setting $\frac{dz}{dt}(\zeta, t) = \frac{\partial z}{\partial \zeta}\frac{\partial \zeta}{\partial t} + \frac{\partial z}{\partial t} = \frac{\partial z}{\partial \zeta}v + \frac{\partial z}{\partial t}$ in (3.1) renders the following equation that has to be solved both in time and space to find a closed-form relationship to account for the friction.

$$\frac{\partial z}{\partial \zeta}(\zeta, t) = 1 - sign(v)\frac{\sigma_0}{g(v)}z - \frac{1}{v}\frac{\partial z}{\partial t}(\zeta, t) \tag{3.5}$$

Assuming the deflection of the first bristle element to be zero imposes the boundary condition as $z(0, t) = 0$ for $\forall t \geq 0$. In a quasi-static condition where $\frac{\partial z}{\partial t}(\zeta, t) \simeq 0$ within a small enough interval of time, (3.5) is reduced to

$$\frac{\partial z}{\partial \zeta}(\zeta, t) = 1 - sign(v)\frac{\sigma_0}{g(v)}z \quad \zeta \in (0, L) \tag{3.6}$$

The solution of the ordinary differential equation (ODE) defined in (3.6) is expressed as below, and can suitably approximate the solution of the equation introduced in (3.5). It is assumed in (3.6) that the bristles have a faster dynamic response compared to variations of the insertion velocity.

$$z_{qs} = \frac{g(v)}{\sigma_0}(1 - e^{-\frac{\sigma_0}{g(v)}\zeta})sign(v) \tag{3.7}$$

$$F_{qs} = \int_0^L \{\sigma_0 z_{qs} + \sigma_2 v\} f_n(\zeta)d\zeta \tag{3.8}$$

To calculate the steady-state solution defined by (3.8), it is required to know the distribution of the force density function $f_n(\zeta)$. For the sake of simplicity, the first step is to presume a uniform load intensity where $f_n(\zeta) = F_n/L$ for $\zeta \in (0, L)$. Here, F_n stands for the total normal load along the shaft. This particular choice agrees with the constant estimated force density along the needle shaft reported in [25]. Due to the symmetry resulting from the use of a cone-tip needle, the force peak at the tip that can be attributed to the tissue cutting force [25] is ignored here. Therefore, the quasi-static solution, namely Model I, is expressed as

$$F_{qs} = \left(sign(v)g(v)\left[1 - \frac{g(v)}{\sigma_0 L}(1 - e^{-\frac{\sigma_0 L}{g(v)}})\right] + \sigma_2 v\right)F_n \tag{3.9}$$

Following this strategy and by fitting the above steady-state representation to experimental data, the unknown parameters except σ_1 can be identified. As another numerical approximation that is proposed at this point, the distributed model introduced by (3.1) agrees with a lumped model assuming that the patch region is not changing with respect to time, or the bristles are moving much faster than the needle itself. A mean friction state is defined as follows [20]:

$$\tilde{z}(t) = \frac{\int_0^L z(\zeta, t)f_n(\zeta)d\zeta}{F_n} \tag{3.10}$$

where $F_n = \int_0^L f_n(\zeta)d\zeta$. Following a few algebraic manipulations and applying the chain rule using (3.5) and (3.10) the friction model in terms of $\tilde{z}$ is given by (3.11). In the following, the first and last terms on the right-hand side of (3.12) represent the effect of the boundary conditions while the term under the integral describes the impact of the lateral

force distribution.

$$\begin{cases} \dot{\tilde{z}} = v - \left(sign(v)\frac{\sigma_0}{g(v)} - \beta(t)\right)v\tilde{z} \\ F_{friction}(t) = F_n(\sigma_0\tilde{z} + \sigma_1\dot{\tilde{z}} + \sigma_2 v) \end{cases} \tag{3.11}$$

$$\beta(t) = \frac{1}{F_n\tilde{z}}\left(z(0,t)f_n(0) + \int_0^L z(\zeta,t)\frac{\partial f_n(\zeta)}{\partial\zeta}d\zeta\right) - \frac{f_n(L)}{F_n} \tag{3.12}$$

This approximation is called the averaged lumped model. Setting $\frac{\partial f_n}{\partial\zeta}(\zeta) = 0$ in (3.12) due to the assumption of a uniform load distribution with zero-force boundary conditions, i.e., $f_n(0) = f_n(L) = 0$, yields $\beta(t) = 0$. This assumption is borrowed from the fact that a realistic solution, by continuity, provides zero normal force at the boundaries of the contact area. A trapezoidal force profile that fully satisfies these conditions may be a more realistic choice. However, the main reason for setting $f_n(\zeta)$ to be uniform along the shaft with zero force intensity at the boundaries is to reduce the identification complexity. Thus, we obtain Model II as

$$\begin{cases} \dot{\tilde{z}} = v - \frac{\sigma_0|v|}{g(v)}\tilde{z} \\ F_{friction}(t) = F_n(\sigma_0\tilde{z} + \sigma_1\dot{\tilde{z}} + \sigma_2 v) \end{cases} \tag{3.13}$$

This feasible and dynamic scheme denoted by (3.13) is in fact the conventional point-contact LuGre model, and will be used in the sequel as employed in [22]. However, in order to more precisely incorporate the effect of distributed needle-tissue interaction, and introduce the third friction model, β should not be ignored from the friction calculations. The function β captures the distributed nature of translational friction, and is determined according to the postulated functional form of $f_n(\zeta)$. Towards this goal, let us assume that $z(\zeta,t)$ can be decomposed into two time-independent and space-independent components $\psi(\zeta)$ and $\phi(t)$, respectively [20]. Hence, $z(\zeta,t) = \psi(\zeta)\phi(t)$ for $0 \leq \zeta \leq L(t)$ and $t \geq 0$, and $\beta(t)$ is rewritten by replacing L with $L(t)$ in (3.12), and applying the zero-force boundary conditions.

$$\beta(t) = \frac{\int_0^{L(t)} \psi(\zeta)f_n'(\zeta)d\zeta}{\int_0^{L(t)} \psi(\zeta)f_n(\zeta)d\zeta} \tag{3.14}$$

For a trapezoidal distribution that is a realistic assumption, the normal force intensity function can be defined by a set of five parameters, namely k_1, k_2, w_1, w_2 and f as in (3.15). In case of a symmetrical distribution, we have $w_1 = w_2 = w$, $k_1 = f/w$, and $k_2 = Lf/w$ ($w \neq 0$) in Fig. 5.1. Note that it is rational to assume that the bristles are gradually deflected along the contact patch. In addition, for the first differential bristle-like element at the skin

entry point, the amount of deflection is zero as assumed previously.

$$f_n(\zeta) = \begin{cases} k_1\zeta & 0 \leq \zeta \leq w_1 \\ f & w_1 \leq \zeta \leq L(t) - w_2 \\ -k_1\zeta + k_2 & L(t) - w_2 \leq \zeta \leq L(t) \end{cases} \tag{3.15}$$

Thus, $\psi(\zeta) = \zeta^\lambda \left(0 \leq \zeta \leq L(t), \ \lambda > 0\right)$ is a good candidate to represent the deflection function ψ in (3.14). Next, introducing (3.15) into (3.14) yields the sought function $\beta(t)$. Thus, $\beta(t)$ is approximated using either (3.16) or (3.17).

$$\beta_1(t) \approx \begin{cases} \frac{\lambda+2}{\lambda+1}\frac{1}{L(t)} & 0 < L(t) \leq w \\ \frac{(\lambda+2)w^\lambda}{(\lambda+2)L(t)^{\lambda+1}-w^{\lambda+1}} & L(t) > w \end{cases} \tag{3.16}$$

$$\beta_2(t) \approx \begin{cases} \frac{-2(\lambda+2)(2^\lambda-1)}{2^{\lambda+1}-1}\frac{1}{L(t)} & 0 < L(t) \leq 2w \\ -\frac{\left(L(t)-w\right)^{\lambda+1}+w^{\lambda+1}-L(t)^{\lambda+1}}{\left(L(t)-w\right)^{\lambda+2}+w^{\lambda+2}-L(t)^{\lambda+2}}(\lambda+2) & L(t) > 2w \end{cases} \tag{3.17}$$

In (3.16), $w = w_1$, and w_2 was set to zero while in (3.17), the function f_n was assumed to have symmetrical form in which $w = w_1 = w_2$. In both cases, at $t = t_k$, the force intensity profile converts to the trapezoidal functional form from the triangular functional shape as it is for $t < t_k$. In this setting, the functions $\beta_1(t)$ and $\beta_2(t)$ correspond to right and isosceles trapezoids, respectively. Accordingly, Figs. 3.3(a) and 3.3(b) show the transition of the force profiles as the needle is inserted into the tissue. In both figures, the dashed circles represent insertions states. States 1 to 3 associate with the growing triangular forms while state 4 is a boundary state, and state 5 denotes the full trapezoidal shape as $t > t_k$. The validity of presuming such force intensity profiles will be investigated later on through experimental work.

Obtaining an explicit expression for the function $\beta(t)$ enables us to complete the distributed dynamic LuGre model represented in (3.11), and thereby forming Model III. Model III is an extension of Model II in which $\beta(t)$ is not zero. It is not difficult to show that (3.14) and therefore (3.16) or (3.17) hold valid for a time-varying insertion velocity. It occurs when the zero-force boundary conditions are satisfied for each differential element at each time instant. Thus, all mathematical terms containing $\dot{L}(t)$ are set to zero towards deriving the closed-form representation of $\beta(t)$. This assumption is valid when the bristles have fast
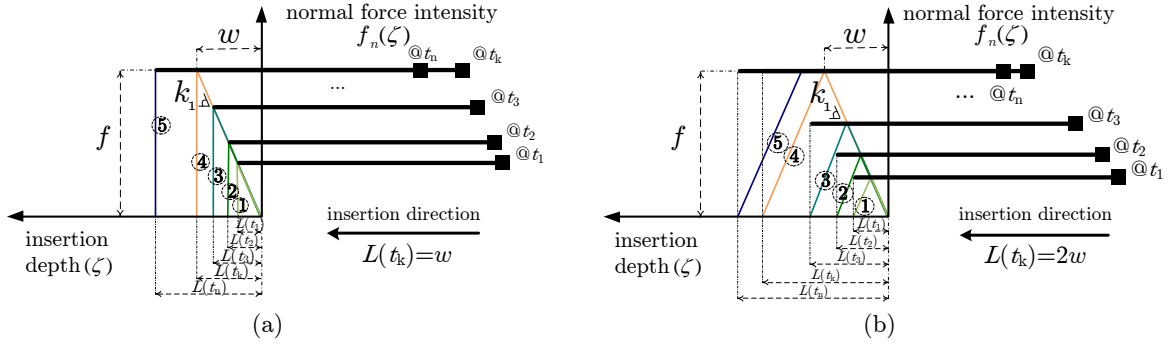
Figure 3.3: Evolution of the triangular/trapezoidal interaction force distribution associated with: (a) β_1 in Model III-A, (b) β_2 in Model III-B.

dynamics relative to the insertion speed.

At this point, the measurement equation expressing the distributed friction is revisited in order to fit it into the new state-space model. Equation (3.4) can be rewritten as

$$F_{friction}(t) = \int_0^{L(t)} \left\{ (\sigma_0 - \frac{\sigma_0 \sigma_1 \mid v \mid}{g(v)}) z(\zeta, t) - \sigma_1 v \frac{\partial z}{\partial \zeta}(\zeta, t) + (\sigma_1 + \sigma_2) v \right\} f_n(\zeta) d\zeta$$

(3.18)

Knowing that $\int_0^{L(t)} z(\zeta, t) f_n(\zeta) d\zeta = \tilde{z}(t) \times \int_0^{L(t)} f_n(\zeta) d\zeta = \tilde{z}(t) \times F_n$, and applying the zero-force boundary conditions, we obtain the following set of equations for Model III in which $\tilde{x}(t)$ stands for the patch length $L(t)$ that can be time-varying. In the current state-space representation (3.19), labeled henceforth as Model III-B, the β function was approximated using β_2 as in (3.17). A similar structure can be simply obtained by the use of β_1 (Model III-A).

$$\begin{cases} \dot{\tilde{x}} = v \\ \dot{\tilde{z}} = \begin{cases} v - \dfrac{\sigma_0}{g(v)} \mid v \mid \tilde{z} - \dfrac{2(\lambda + 2)(2^\lambda - 1)}{2^{\lambda+1} - 1} \dfrac{1}{\tilde{x}} & 0 < \tilde{x} \le 2w \\ v - \dfrac{\sigma_0}{g(v)} \mid v \mid \tilde{z} - \dfrac{(\tilde{x} - w)^{\lambda+1} + w^{\lambda+1} - \tilde{x}^{\lambda+1}}{(\tilde{x} - w)^{\lambda+2} + w^{\lambda+2} - \tilde{x}^{\lambda+2}} (\lambda + 2) v \tilde{z} & \tilde{x} > 2w \end{cases} \\ F_{friction}(t) = f(\tilde{x} - w) \left\{ (1 - \dfrac{\sigma_1 \mid v \mid}{g(v)}) \sigma_0 \tilde{z} - \sigma_1 \dot{\tilde{z}} + (\sigma_1 + \sigma_2) v \right\} \end{cases}$$

(3.19)

3.3   Setup Description

An experimental implementation of the proposed methodology was carried out on the 5-DOF double parallelogram robotic system [23] described in Appendix A. In our test-bed, needle A represents the cannula of an 18GA needle (Cook Medical) while needle B denotes the cannula of a 22GA needle (Covidien). Needle B is more flexible than needle A both of which are with conical tip. Using a compression test [24], Young's modulus E of an examined phantom was also estimated from the force-deformation mapping of the sample with known geometry. In this test-bed, needle A represents the cannula of an 18GA needle (Cook Medical) while needle B denotes the cannula of a 22GA needle (Covidien). Needle B is more flexible than needle A both of which are with conical tip.

3.4   Experimental Studies

3.4.1   Friction Identification Using an Artificial Phantom

We start validating the proposed friction structure with a detailed description of the artificial phantom study. A similar procedure was applied to organic tissue that will be explained in section 3.4.3. The artificial phantom was made from Gelrite Gellan Gum (Sigma-Aldrich) with two different concentrations in water: 4% (tissue A, E= 0.11MPa, less stiff) and 6% (tissue B, E= 0.16MPa, more stiff). This powder simulated a uniform elastic environment, and created a watery medium that made the experiments more realistic in terms of the measured force ranges and viscosity.

In order to identify the models' parameters, the system was excited in the axial direction by applying a low-frequency sinusoidal torque. The frequency and the amplitude of the insertion signal was selected so that it could transition the system from the pre-sliding to the sliding phase and vice versa. The proper selection required a few trials and errors. We examined a translational motion profile whose maximum amplitude (d_{in}) lied between 10mm and 50mm and its frequency (f_{in}) ranged from 0.02Hz to 0.2Hz. In this setting, γ was assumed to be 1 in (3.2), and without loss of generality, F_n was set to 1.

For identification, the needle was inserted from one side into the phantom so that the tip was placed 5cm outside of the tissue. Each artificial phantom with a known thickness
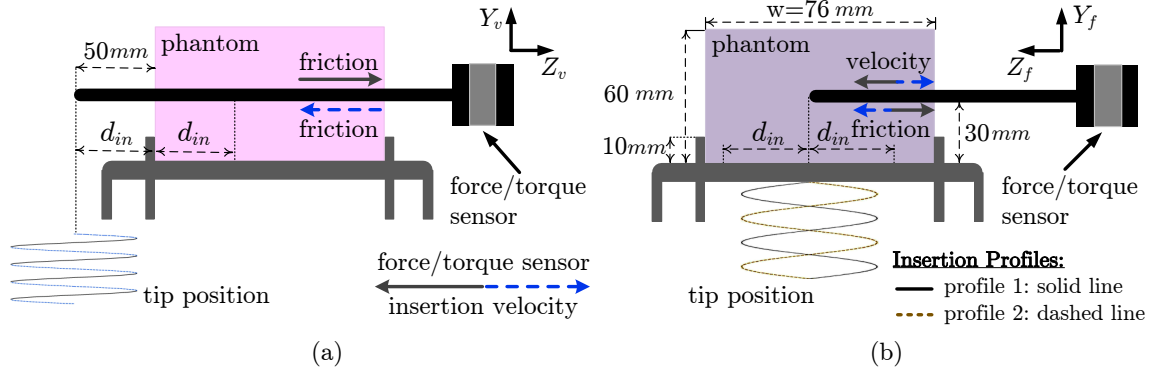
Figure 3.4: Needle insertion profiles: (a) periodic insertion profile for friction identification, (b) cyclic insertion profiles for friction estimation.

(w=76mm) was placed into a container and clamped such that the bottom of the tissue was rigidly fixed (see Fig. 3.4). The insertion height was approximately adjusted to 30mm, while the phantoms were fabricated at the total height of 60mm. In the identification test shown in Fig. 3.4(a), the tip is not cutting the tissue and there exists a constant amount of tissue in contact with the needle shaft. Fig. 3.4(b) in addition corresponds to the prediction test in which the needle tip is initially placed in a middle point inside the phantom. It will be later on revisited in section 3.4.2.

The total axial force (F_z) measured by the F/T sensor is expressed as the sum of inertial and interaction forces. The interaction force is composed of a cutting force at the tip and distributed friction along the needle. The estimated acceleration profile (a) and mass of each needle plus its holder (m) are known. The mass values for the 18GA and 22GA needles were measured to be 44.058g and 13.128g, respectively. Thus, according to the reference frames of the force sensor and the robot's end-effector expressed in Fig. 3.4, we have $F_{interaction} = F_z(measured) + ma$.

Note that clinical insertion rates are usually kept low (less than 10mm/s [25]) mainly due to safety considerations. One practical issue of applying low velocities and accelerations is that ordinary differentiation to compute joint velocities from encoder readings leads to high computational noise. Thus, to reduce this noise which can become dominant, a high-gain observer has been implemented to estimate the velocity from the encoder measurements. The details of observation and velocity estimation have been discussed in [26] where we took advantage of dynamic observation to compensate for soft tissue motion during fric-

tion identification. Needle-tissue relative velocity compensation is essential particularly in highly deformable tissue (section 3.4.3) since frictional effects in general depend on the relative velocity between moving contacts.

Having obtained a friction-velocity cycle, the parameters of the models proposed in the previous section can be identified. Due to the additional term $\beta(t)$ in the equations, many of existing adaptive or advanced friction identification techniques [22] are not applicable here. Hence, we employed MATLAB$^{\circledR}$ built-in functions and system identification toolbox to find the unknown parameters of each introduced model. In brief, each structure, i.e., Models I, II, and III, was defined as a nonlinear state-space grey-box model. The specified object then underwent parameter estimation using an iterative prediction-error minimizer, and an adaptive Gauss-Newton search method.

Initially, a sensitivity test was performed. Four values were selected for λ, and Model III was identified in each case for w=2.5mm. Fig. 3.5(a) compares the outcome of each parameter selection for Model III-B. According to this research, it is likely that by optimizing Model III in terms of λ over the entire range of $[0.5, 5]$, friction estimation can be improved further. For the sake of brevity, this task is omitted from this chapter and will be reported in a future publication. Henceforth, it is assumed that this tuning parameter is selected from the set $\{0.5, 2.5, 1.5, 5\}$ such that the estimation error is minimized. In Fig. 3.5(a), the best performance was achieved by setting λ to 5. In addition, Model III-A mimicked a very identical performance but with a different selection for λ; thus, it has been ignored from presentation in this section. However, in section 3.4.2 when the inserted length of the needle changes with the passage of time, Model III-A will be assessed further.

Table 3.1 defines the test conditions of four studied cases, and Figs. 3.5(b)-3.5(c) present two estimated friction-velocity mappings using the introduced LuGre-based techniques. For comparison, the modified Karnopp model was also implemented [9]. Briefly, this static benchmark includes only viscous and Coulomb terms whose corresponding coefficients were estimated by a simple least-squares method. We studied the logged data over four periodic cycles, and repeated each test as described at four different insertion points. The plots show that Models II and III are capable of capturing the dynamic behavior of friction including the Stribeck effect and the hysteresis loop as opposed to the Karnopp model and Model I. Note that the inset subplots in the graphs are the magnified versions of the original plots in the region of the origin in order to better visualize the data. Tables 3.2-3.4 summarize the estimated parameters. The reported results are the averaged values
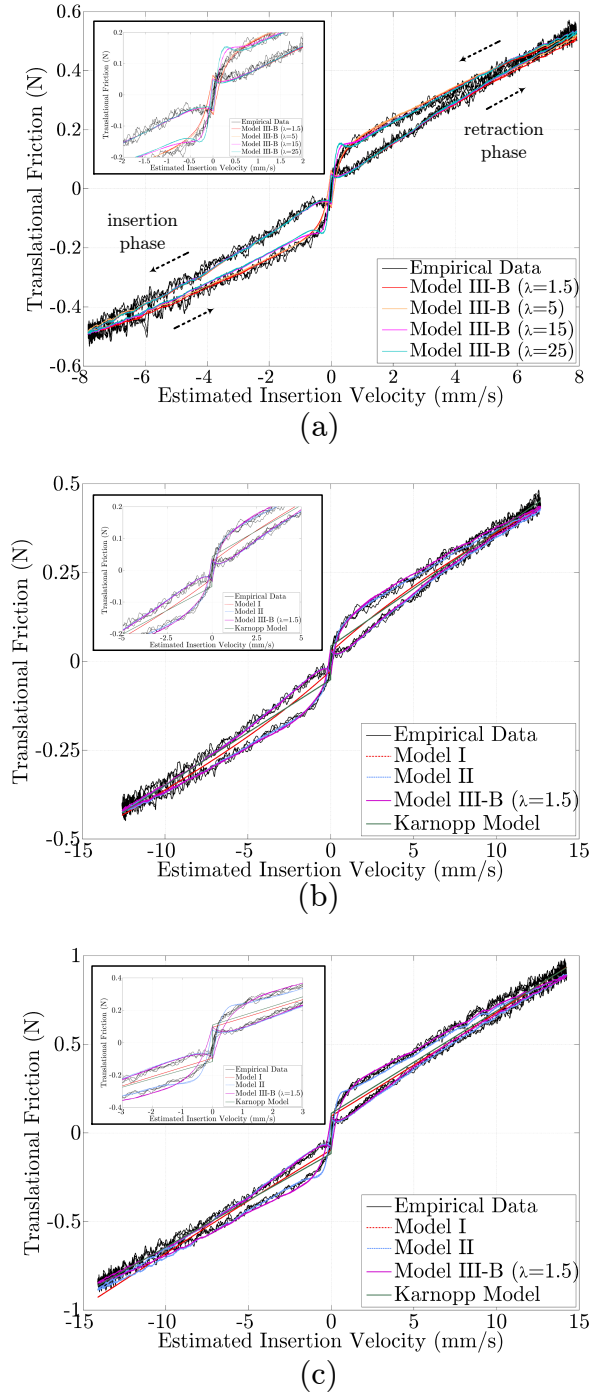
Figure 3.5: (a) Identified and experimental friction-velocity cycle: Model III-B with vari-able λ, needle A/tissue A, f_{in}=0.05Hz, and d_{in}=25mm, (b) Identified and experimental friction-velocity cycle in case 2, (c) Identified and experimental friction-velocity cycle in case 4.

Table 3.1: Test Conditions of Four Case Studies

	case 1	case 2	case 3	case 4
f_{in} (Hz)	0.05	0.08	0.02	0.05
d_{in} (mm)	25	25	45	45
needle/tissue combination	needle A + tissue A	needle B + tissue A	needle A + tissue B	needle B + tissue B

Table 3.2: Estimated Parameters of Model I

	case 1	case 2	case 3	case 4
σ_0	1.272±0.338	0.616±0.098	1.903±0.125	0.812±0.044
σ_2	0.017±0.005	0.015±0.002	0.011±0.002	0.030±0.003
μ_c	0.711±0.116	0.338±0.148	0.715±0.090	0.653±0.055
μ_s	0.044±0.011	0.024±0.003	0.055±0.003	0.058±0.009
α	0.081±0.007	0.077±0.024	0.121±0.018	0.073±0.010

Table 3.3: Estimated Parameters of Model II

	case 1	case 2	case 3	case 4
σ_0	1.344±0.214	0.592±0.224	1.877±0.104	0.813±0.132
σ_1	0.463±0.013	0.239±0.055	0.686±0.045	0.312±0.037
σ_2	0.016±0.003	0.012±0.002	0.011±0.000	0.031±0.002
μ_c	0.735±0.087	0.448±0.082	0.669±0.073	0.633±0.029
μ_s	0.034±0.004	0.017±0.001	0.046±0.003	0.050±0.007
α	0.092±0.007	0.076±0.014	0.113±0.021	0.074±0.002

expressed as mean ± standard deviation (σ). By comparison, the parameter σ_0 had the most inconsistency. Estimation of μ_c could exhibit a similar behavior depending on the insertion profile and the employed needle-tissue combination.

Table 3.5 lists the root mean squared error (RMSE) values of friction estimation in the four considered cases. To further assess the performance of each model, RMSE values were separately evaluated in two ranges of insertion velocities labeled low and high range. The low range was associated with the velocities whose absolute values lied in the interval $[0, 0.5v_{max}]$ while the high range covered the interval $[0.5v_{max}, v_{max}]$. Here, v_{max} denotes the maximum insertion velocity of each motion profile. It is emphasized again that in each experiment, Model III should be optimized in advance in terms of the parameter λ. We defined the same RMSE value as the objective function, and examined the four quantities

Table 3.4: Estimated Parameters of Model III-B

	case 1	case 2	case 3	case 4
σ_0	1.203±0.157	0.559±0.266	1.818±0.143	0.763±0.092
σ_1	0.374±0.017	0.255±0.063	0.581±0.046	0.287±0.030
σ_2	0.014±0.004	0.012±0.001	0.010±0.002	0.028±0.001
μ_c	0.788±0.149	0.450±0.028	0.667±0.014	0.744±0.026
μ_s	0.033±0.003	0.018±0.008	0.041±0.002	0.048±0.006
α	0.088±0.010	0.074±0.006	0.135±0.006	0.072±0.005

Table 3.5: Averaged RMSE of Friction Force Estimation (mN)

	Total				Low range				High range			
	case 1	case 2	case 3	case 4	case 1	case 2	case 3	case 4	case 1	case 2	case 3	case 4
Model I	29.7	23.1	27.0	49.3	37.7	30.1	33.0	51.8	25.1	19.0	23.5	48.0
Model II	19.6	14.5	19.2	30.9	15.9	11.8	18.5	21.2	21.1	16.0	20.0	34.5
Model III-B	17.9	13.3	15.8	28.1	18.1	11.6	17.6	26.6	17.8	13.5	14.3	28.7
Karnopp Model	28.2	22.9	21.8	39.8	38.9	31.4	29.4	52.3	21.2	17.5	17.0	32.3

in each case study to select the best λ value.

In general, the dynamic structures, e.g., Models II and III, outperformed the static models. By comparison, the Karnopp model showed better overall performance than Model I which was the static version of the LuGre model. Nevertheless, Model I provided a slightly better prediction for the low range velocities in cases 1, 2, and 4. Model I also exhibited an exponential growth of error in terms of velocity that was more apparent in Fig. 3.5(c) (for $v \leq$-10mm/s). At higher velocities, Model III-B performed better in contrast to Model II, and surprisingly, the Karnopp model outperformed Model II in cases 3 and 4 (the second half of Table 3.5). Considering all the models and cases studied, Model III-B excelled overall as shown. This suggests that the isosceles trapezoidal force density function in needle insertion serves better than the right trapezoidal density assumption. To remind, see Fig. 3.3. However, in the vicinity of zero velocity, Model II depicted the friction loop the best in case studies 1 and 4 according to the low-range error values reported in Table 3.5. This better accuracy originates from the faster transient response provided by Model II that is visible in the upper-left graph in Fig. 3.5(c).

In the observations, unexpected fluctuations in the empirical data should not come as a surprise. In practice, it was not easy to fabricate a completely homogeneous phantom using Gellan gum, and air bubbles spread over the volume of the phantom prevented the

Table 3.6: Averaged RMSE of Friction Force Prediction (mN)

	solid profile		dashed profile	
	case 1	case 2	case 1	case 2
Model I	79.0	68.9	74.7	62.8
Model II	73.1	67.0	75.6	68.7
Model III-A	39.2	31.5	55.3	35.7
Model III-B	41.9	22.8	51.6	29.0

medium from being fully uniform.

3.4.2   Friction Prediction and Cutting Force Estimation

Having identified the models, the estimated parametric values (specified in Tables 3.2-3.4) were fed into the selected lumped or distributed model in order to predict the friction force along the time-varying insertion length. In this experiment, the needle tip was initially placed inside the phantom so that L_0=0.5w=38mm (see Fig. 3.4(b)). In the first motion profile illustrated by a solid line, the needle was inserted until it approached the left wall of the container and then it was retracted towards the right wall. In the second profile denoted by a dashed line in the same plot, the tip motion had an opposite periodic sequence. To conduct the experiments, needle B was inserted into tissue A and tissue B respectively at the rates of 0.05Hz and 0.08Hz (d_{in}=25mm). Here, they are referred to as cases 1 and 2. Testing other combinations was possible, but without loss of generality, we limited the observations to only two case studies. Fig. 3.6 compares the measured interaction force with the predicted friction forces in the second case study, and Table 3.6 reports the numerical results in which major cutting was excluded from RMSE calculations.

Generally speaking, the cutting mechanism, as the most obvious non-frictional behavior during needle insertion, has not been well formulated heretofore. The cutting force at the needle tip (Fig. 5.1) is influenced by complex factors, e.g., tip shape and tissue properties, in practice. As mentioned before, the measured axial force denotes the summation of friction, cutting force, and inertial effect meaning that we can estimate the cutting force if the frictional effects are accurately modeled. Thus, as a potential advantage of the proposed scheme, the cutting force can be simply obtained by deducting the estimated friction and inertial term from the totally measured interaction force.
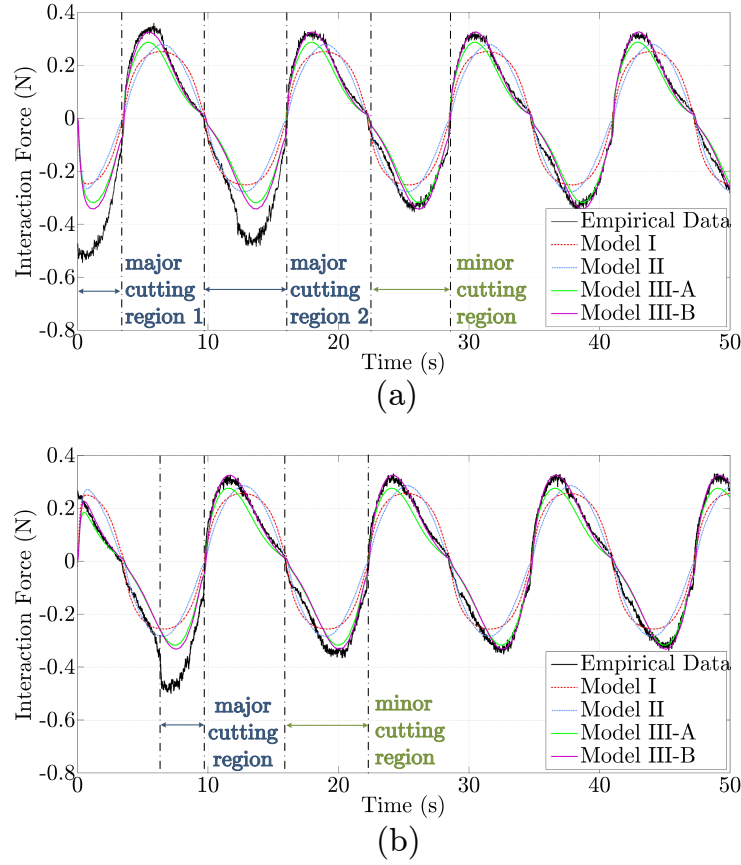
Figure 3.6: Predicted and measured interaction force: needle B/tissue A, f_{in}=0.08Hz, and d_{in}=25mm (case 2): (a) solid profile (b) dashed profile.

In the experiments carried out in section 3.4.1, the needle tip protruded from the tissue container hence no major cutting was present. This is not the case here since the tip cuts the tissue during the first cycle(s) of penetration. Referring to Fig. 3.6(a), within the very first seconds of motion, cutting occurred which was indicated by the major cutting regions. Substantial cutting also existed in the second profile as highlighted before 10s during needle penetration into fresh tissue. According to Fig. 3.6(a), minor cutting as a result of unpredicted needle-tissue interaction was found to be present in the third and fourth negative lobes of insertion. Here, due to the tip shape, needle deflection was small, and could be ignored from calculations as we have done. However, the slight bending that was not easy to predict caused the needle to cut fresh tissue. Consequently, an extra cutting force with a random pattern was introduced during the periodic insertion phase denoted by minor cutting in Fig. 3.6. Herein, the force prediction error can be mainly attributed to the cutting effect.

From the graphs, it is evident that the distributed solution, i.e., Model III, exhibits reasonably accurate results. Both versions of this model maintained close levels of accuracy albeit version B performed slightly better. Another observation was the inability of the lumped version (Model II) to provide a good friction tracking while its accuracy was unexpectedly as low as the static structure (Model I). Model II presented a good estimation of the friction loop in section 3.4.1. However, lack of an explicit term of the time-varying inserted length in (3.13) turned out to degrade accuracy here. It is worth noting that some of the conditions applied for the ease of implementation, e.g., the simplified boundary conditions introduced in section 3.2, make a perfect match impossible. This suggests that $f_n(\zeta)$ or $\psi(\zeta)$ may have complex functional shapes in reality that need further investigation.

3.4.3   Friction Identification in Organic Tissues

Living tissues exhibit complex behaviors. In section 3.4.1, due to the relative rigidity of the employed sample, tissue motion was negligible. However, organic tissues are expected to deform substantially. The mechanism introduced in [26] was employed in this chapter to compensate for the relative velocity between a moving needle and deformable tissue. This technique allows us to formulate translational friction with respect to the insertion rate without imposing further complexities in tracking the entire soft tissue motion. For more details, refer to [26].

We repeated a similar set of experiments using gelatin samples of differing concentrations (4%-8%). Gelatin is an organic artificial substance whose main ingredients are bone and pig skin. Compared to the Gellan gum, the gelatin-made phantom deformed considerably, and exhibited a smoother force pattern with a negligible Stribeck effect. By tuning the slow observer introduced in [26], the distributed friction in 5% gelatin (E= 5.57kPa) was successfully predicted as illustrated in Figs. 3.7(a)-(b). At the next stage, beef liver was examined. The liver was the least stiff tissue (E= 1.89kPa) in the experiments, and deformed the most. In this case, it was observed that the dynamics of tissue relaxation and friction mixed together lead to a wide force-velocity mapping; thus, a very slow velocity observer was employed to track the tissue motion. Figs. 3.7(c)-(d) show the measured and the estimated loops in terms of the estimated needle velocity and the estimated needle-tissue relative velocity in a studied case. Accordingly, in beef liver, the friction force in terms of needle-tissue relative velocity could be represented approximately by a single viscous term
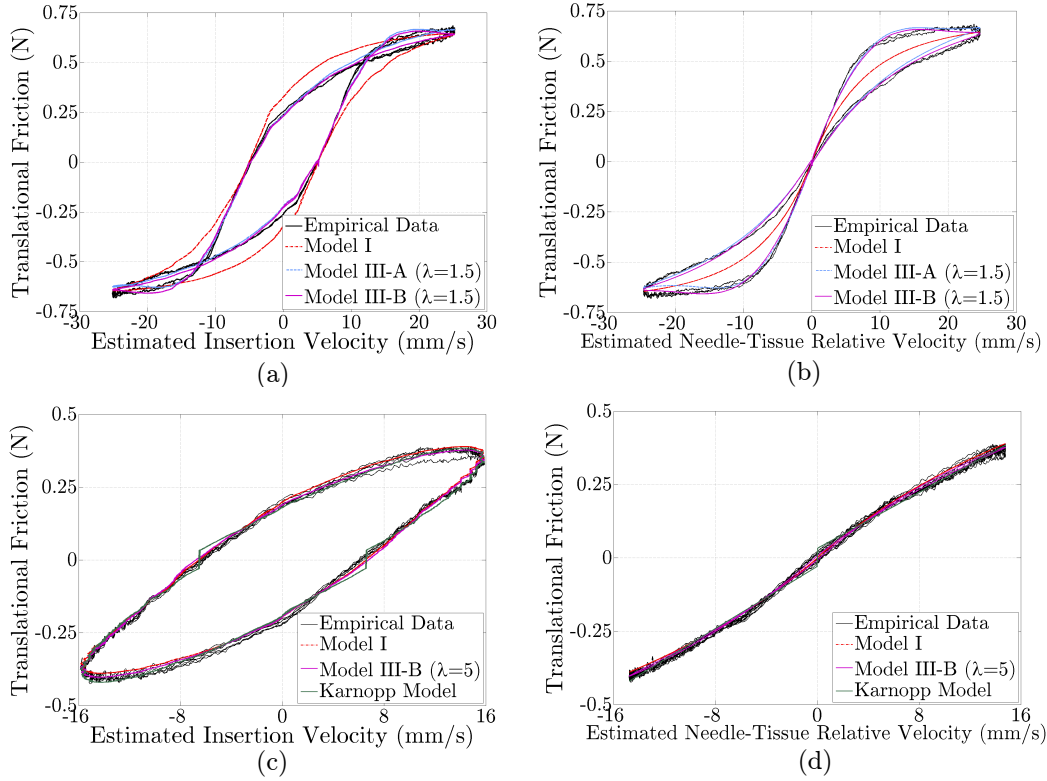
Figure 3.7: Experimental and identified cycles: (a) reconstructed friction versus needle insertion velocity using needle A/gelatin (5% concentration), f_{in}=0.1Hz, and d_{in}=40mm, (b) friction versus needle-tissue relative velocity using needle A/gelatin (5% concentration), f_{in}=0.1Hz, and d_{in}=40mm, (c) reconstructed friction versus needle insertion velocity using needle A/beef liver, f_{in}=0.1Hz, and d_{in}=25mm, (d) friction versus needle-tissue relative velocity using needle A/beef liver, f_{in}=0.1Hz, and d_{in}=25mm.

whereas the hysteresis was found to be substantial with respect to the needle velocity. The Stribeck effect was also absent which may stem from the internal lubrication of the organ due to blood. In addition, one foreseeable observation in the recent experiment was the high variations in the force patterns acquired at different insertion paths. This fact originated from tissue inhomogeneity. Consequently, standard deviation values of the estimated parameters were relatively large; however, the suggested approach yielded good results at a wide range of insertion frequencies and amplitudes. Due to space limitations, only one set of results is reported here.

We also performed extensive *ex-vivo* experiments on other animal tissues. In each case, tissue membrane and fat layers were initially removed. Fresh muscle including chicken breast, beef, and pig ham produced identical force-velocity loops whose dynamics differed

from the cycles generated by the LuGre model(s). For example, in extended experiments on these three types of muscle tissue, it was observed that the equivalent Stribeck effect appeared very slowly, and viscous damping turned out to be negative (or zero) that were not justifiable by conventional friction theories. This suggests that mechanics of translational friction in muscle-like materials deserves more theoretical work. It is likely that we need to look at the problem at a molecular level in order to identify and then classify the structural components of a specific type of organic tissue. This is a challenging area in materials science and demands further study. Guidelines provided in [27, 28] can be helpful since tissue inhomogeneity and nonlinearity contribute to greater complexity in analyzing of living tissue. The case studies presented in this work showed how the proposed approach can accommodate and deal with a wide range of friction dynamics in needle-tissue interaction without excessive complexity.

3.5   Concluding Remarks and Future Work

This chapter presented a sophisticated approach to study and model features of translational friction during needle-tissue interaction. The interaction between the needle and soft tissue comprises frictional effects, and exhibits hysteresis loops. We showed that static friction mappings were inadequate for describing the existing transient nature. On the other hand, the proposed family of single-state dynamic models as alternatives were capable of rendering the dynamics of the distributed friction along the needle shaft. In practice, they performed well in a number of organic and artificial phantoms, e.g., agar, gelatin, and beef liver, while preserving favorable static and dynamic properties. The proposed models were developed by extending the well-known LuGre point friction model to the case of a moving contact patch along the insertion depth. Overall, the close match between the measured and the estimated friction forces presented in this chapter proved the capability of the suggested approach to mimic friction complexities. Furthermore, the proposed structure facilitated approximating the cutting force in an intraoperative manner.

In this study, due to the shape of the needle tip, bending was negligible, but future work will explore the effect of the distributed friction on bending dynamics of a bevel-tip needle. Friction modeling is believed to be a crucial step towards automating needle guidance in live tissues, and the method developed in this chapter enable us to refine the beam-based deflection models in which full frictional effects are ignored [2]. Although not very accu-

rate, these static models are widely exploited for the purpose of steering [3–5] due to their simplicity and computational efficiency. In order to steer a flexible needle, clinicians will likely have to slow down the insertion and rotate the needle with variable insertion rates before further actions. Thus, path deviation as a result of unmodeled friction can cause planning inaccuracy. Related research is reported in [6] in which only the viscous term was accounted for in needle deflection.

In the experiments conducted, the frictional effects during needle insertion were found to be considerable. Furthermore, significant differences were observed between the phantoms either artificial or organic. Considering these empirical observations, exploring a new artificial phantom as a mixture of chemicals that produces a more realistic force pattern would be of value. It will certainly ease and accelerate the process of developing new modeling and guidance mechanisms in interventional procedures. As is obvious, managing experiments on animal organs under controlled or repeatable conditions is challenging and requires addressing practical issues including (1) storage and contamination; (2) precise cutting and fitting the sample into its container, and (3) tissue immobilization. That is why artificial phantoms are usually preferred as the very first steps in validating a new approach. An ideal artificial phantom is expected to preserve the typical range of elasticity, viscosity and tissue deformation of living tissues as well as replicating its force-velocity dynamics. Another aspect of future work involves validation of the results using other animal organs such as lung and kidney. In the case of inhomogeneous phantoms, the dynamics of tissue puncture may have considerable effect on the entire needle-tissue interaction, especially for multi-layer tissue. This also requires further in-depth investigation.

Bibliography

[1] N. Abolhassani, R. Patel, and M. Moallem, "Needle Insertion into Soft Tissue: A Survey," *Med. Eng. Phys.*, vol. 29, pp. 413-431, 2007.

[2] N. Abolhassani, R.V. Patel, and F. Ayazi, "Minimization of Needle Deflection in Robot-Assisted Percutaneous Therapy," *Int. J. Med. Robotics Comput. Assist. Surg.*, vol. 3, pp. 140-148, 2007.

[3] V. Duindam, J. Xu, R. Alterovitz, S. Sastry, and K. Goldberg, "Three-Dimensional Motion Planning Algorithms for Steerable Needles Using Inverse Kinematics," *Int. J. Rob. Res.*, vol. 29, pp. 789-800, 2010.

[4] N.A. Wood, K. Shahrour, M.C. Ost, and C.N. Riviere, "Needle Steering System Using Duty-Cycled Rotation for Percutaneous Kidney Access," *In Proc. of 32nd IEEE EMBS Annu. Int. Conf.*, 2010, pp. 5432-5435.

[5] R. Alterovitz, M. Branicky, and Ken Goldberg, "Motion Planning under Uncertainty for Image-Guided Medical Needle Steering," *Int. J. Rob. Res.*, vol. 27, no. 11-12, pp. 1361-1374, 2008.

[6] A. Asadian, M.R. Kermani, and R.V. Patel, "An Analytical Model for Deflection of Flexible Needles During Needle Insertion," *In Proc. of IEEE/RSJ Int. Conf. on Intel. Rob. Sys. (IROS)*, 2011, pp. 2551-2556.

[7] S. Misra, K.T. Ramesh, and A.M. Okamura, "Modeling of Tool-Tissue Interactions for Computer-based Surgical Simulation: A Literature Review," *Presence-Teleop. Virt.*, vol. 17, no. 5, pp. 463-491, 2008.

[8] D.J. Van Gerwen, J. Dankelman, and J.J. van den Dobbelsteen, "Needle-Tissue Interaction Forces: A Survey of Experimental Data," *Med. Eng. Phys.*, vol. 34, no. 6, pp. 665-680, 2012.

[9] A.M. Okamura, C. Simone, and M.D. O'Leary, "Force Modeling for Needle Insertion into Soft Tissue," *IEEE Trans. Biomed. Eng.*, vol. 51, no. 10, pp. 1707-1716, 2004.

[10] A. Asadian, M.R. Kermani, and R.V. Patel, "A Novel Force Modeling Scheme for Needle Insertion Using Multiple Kalman filters," *IEEE Trans. Instrum. Meas.*, vol. 61, no. 2, pp. 429-438, 2012.

[11] H. Kataoka, T. Washio, K. Chinzei, K. Mizuhara, C. Simone, and A.M. Okamura, "Measurement of the Tip and Friction Force Acting on a Needle During Penetration," *In Proc. of 5th Int. Conf. on Med. Image Comput. Comput. Assist. Intervention (MIC-CAI)*, 2002, pp. 216-223.

[12] T.K. Podder, J. Sherman, E.M. Messing, D.J. Rubens, D. Fuller, J.G. Strang, R.A. Brasacchio, and Y. Yu, "Needle Insertion Force Estimation Model Using Procedure-specific and Patient-specific Criteria," *In Proc of 28th IEEE EMBS Annu. Int. Conf.*, 2006, pp. 555-558.

[13] L. Barbe, B. Bayle, and M. de Mathelin, "In vivo Model Estimation and Haptic Characterization of Needle Insertions," *Int. J. Rob. Res.*, vol. 26, no. 11-12, pp. 1283-1301, 2007.

[14] J.T. Hing, A.D. Brooks, and J.P. Desai, "Reality-based Estimation of Needle and Soft Tissue Interaction for Accurate Haptic Feedback in Prostate Brachytherapy Simulation," *Springer Tracts in Advanced Robotics*, vol. 28, pp. 34-48, 2007.

[15] R.J. Webster III, J.S. Kim, N.J. Cowan, G.S. Chirikjian, and A.M. Okamura, "Non-holonomic Modeling of Needle Steering," *Int. J. Rob. Res.*, vol. 25, no. 5-6, pp. 509-525, 2006.

[16] H. Olsson, K.J. Astrom, C. Canudas De Wit, M. Gafvert, and P. Lichinsky, "Friction Models and Friction Compensation," *Eur. J. Control*, vol. 4, no. 3, pp. 176-195, 1998.

[17] R.J. Roesthuis, Y.R.J. van Veen, A. Jahya, and S. Misra, "Mechanics of Needle-Tissue Interaction," *In Proc. of IEEE/RSJ Int. Conf. on Intel. Rob. Sys. (IROS)*, 2011, pp. 2557-2563.

[18] K.B. Reed, A.M. Okamura, and N.J. Cowan, "Modeling and Control of Needles with Torsional Friction," *IEEE Trans. Biomed. Eng.*, vol. 56, no. 12, pp. 2905-2916, 2009.

[19] A. Asadian, R.V. Patel, and M.R. Kermani, "A Distributed Model for Needle-Tissue Friction in Percutaneous Interventions," *In Proc. of IEEE Int. Conf. on Rob. Autom. (ICRA)*, 2011, pp. 1896-1901.

[20] C. Canudas De Wit, P. Tsiotras, E. Velenis, M. Basset, and G. Gissinger, "Dynamic Friction Models for Road/Tire Longitudinal Interaction," *Veh. Syst. Dyn.*, vol. 39, no. 3, pp. 189-226, 2003.

[21] C. Canudas De Wit, H. Olsson, K.J. Astrom, and P. Lischinsky, "A New Model for Control of Systems with Friction," *IEEE Trans. Automat. Contr.*, vol. 40, pp. 419-425, 1995.

[22] M.R. Kermani, R.V. Patel, and M. Moallem, "Friction Identification and Compensation in Robotic Manipulators," *IEEE Trans. Instrum. Meas.*, vol. 56, no. 6, pp. 2346-2353, 2006.

[23] H.S. Bassan, R.V. Patel, and M. Moallem, "A Novel Manipulator for Percutaneous Needle Insertion: Design and Experimentation," *IEEE/ASME Trans. Mechatron.*, vol. 14, no. 6, pp. 746-761, 2009.

[24] K.A. Ross, M.G. Scanlon, "Analysis of the Elastic Modulus of Agar Gel by Indentation," *J. Texture Stud.*, vol. 30, no. 1, pp. 17-27, 1999.

[25] S.P. DiMaio, S.E. Salcudean, "Needle Insertion Modelling and Simulation," *IEEE Trans. Robot. Autom.*, vol. 19, no. 5, pp. 864-875, 2003.

[26] A. Asadian, R.V. Patel, and M.R. Kermani, "Compensation for Relative Velocity between Needle and Soft Tissue for Friction Modeling in Needle Insertion," *In Proc. of 34th IEEE EMBS Annu. Int. Conf.*, 2012, pp. 960-963.

[27] M. Mahvah, P.E. Dupont, "Mechanics of Dynamic Needle Insertion into a Biological Material," *IEEE Trans. Biomed. Eng.*, vol. 57, no. 4, pp. 934-943, 2010.

[28] K. Lister, Z. Gao, and J.P. Desai, "Development of In Vivo Constitutive Models for Liver: Application to Surgical Simulation," *Ann. Biomed. Eng.*, vol. 39, no. 3, pp. 1060-1073, 2011.

Chapter 4

Compensation for the Relative Velocity between Needle and Soft Tissue for Friction Modeling in Needle Insertion

The material presented in this chapter has been published in the Proceedings of the 34th *Annual International Conference of the IEEE Engineering in Medicine and Biology Society (EMBS), pp. 960-963, USA, 2012.*

4.1   Introduction and Related Work

Flexible needles have the potential to provide dexterous and precise targeting for percutaneous interventions while reducing the patient's suffering and trauma. However, erroneous needle guidance mitigates the effectiveness of the planned therapy or diagnosis. Much of research on needle insertion has focused on surgical simulation [1, 2], although needle guidance in the contexts of robot-assisted needle insertion has been rapidly growing [3–5]. While not fully investigating robustness issues, a significant body of work exists on controlling bevel-tip steerable needles using ideal kinematic models [4, 5]. Accordingly, a

steerable needle is controlled from its base through sequential insertion and rotation actions.

The needle itself can be considered as a flexible structure whose shape is determined by needle-tissue interaction forces. Modeling of these forces is challenging, and there has been extensive research work on characterization of the interaction behavior. Using various needle geometries, the complexity and variability of needle response once it is inserted into biological tissues was shown in [6].

Note that the surrounding environment in the needle insertion problem is subject to deformation. Tissue motion is essential in force studies and especially in friction modeling. This is the main focus of the current chapter. The approaches reported in the literature for tissue tracking are mostly employed to construct surgical simulators primarily using finite element analysis. Applying this method, X-ray opaque markers were placed at several layers of a silicone gel phantom, and real-time images were captured in indentation tests [2]. Tracking the 2D motion of embedded markers by a CMOS camera, DiMaio and Salcudean [7] modeled force distribution along the needle shaft. Crouch et al. [8] also addressed the velocity-dependency of force profile in transparent silicone gel. In their work, force-displacement data were acquired using multiple layers of fiducial markers whose 3D positions were captured by two digital cameras. Dehghan et al. [9] proposed an experimental technique to build a prostate brachytherapy simulator in which B-mode ultrasound images and radio-frequency (RF) signals were used to measure tissue displacement. In another study to characterize needle-tissue interaction, Hing et al. [10] tracked implanted fiducial beads in tissue using a dual C-arm fluoroscopy. In a different application to model friction, a CCD camera was used to track a single marker attached near the needle-tissue contact point, and then the Karnopp friction model was implemented [11]. In this work, relative inaccuracy and high variance of the estimated parameters can be attributed to the low resolution of the acquired images as well as the camera's low update rate. In an early study on force modeling and identification in needle insertion, Okamura et al. [12] distinguished frictional effects using fluoroscopic images and manual segmentation. However, they did not include tissue displacement in their force model.

The current work is in line with former studies to find an analytical and feasible representation of needle-tissue interaction and particularly friction. We addressed friction and associated issues in [13] in which tissue motion was not considered due to relative rigidness of the examined sample. However, in clinical procedures, living tissues are expected

to deform depending upon the insertion rate and needle type. Thus, soft tissue deformation should be accounted for in friction modeling. Towards this goal, we will analyze tissue motion during needle insertion, and present a functional routine so that the previously developed friction structure [13] can mimic the dynamic nature of translational friction in the presence of tissue deformation.

The rest of this chapter is organized as follows. Section 4.2 introduces the proposed velocity filtering scheme. Section 4.3 presents experimental results, and section 4.4 summarizes the chapter with conclusions and suggestions for future work.

4.2 Estimation of Tissue Motion for Reconstructing Friction-Velocity Loop

We have built this work on a previous friction analysis introduced in Chapter 3 to deal with significant tissue deformation. Mathematical details and the employed procedure regarding the friction model were introduced in [13]. In brief, this LuGre-based scheme is capable of mimicking standard features of the friction phenomenon in solid contacts including viscous friction, hysteresis, and the Stribeck effect. One crucial observation in the extended tests was that this structure could not tolerate tissue deformation, thus was unable to represent the wide hysteresis loop around the origin in the force-velocity cycle. This discrepancy is studied and compensated for in this study.

Note that clinical insertion rates are usually kept low mainly due to safety concerns. One practical issue of applying a low-velocity or low-acceleration profile in feedback control is that ordinary differentiation to compute joint velocities from encoder readings leads to large amounts of computational noise. Thus, to reduce the noise perturbation that can be dominant, a high-gain observer is implemented to estimate the velocity from the encoder measurements. We will benefit from this feature in order to estimate needle-tissue relative motion. Let us denote the joint angle as θ and the corresponding joint velocity as ω. The estimated values are, therefore, recursively obtained in joint space using (4.1) in which i and T are respectively the sampling instant and the sampling time [14].

$$
\begin{cases}
\tilde{\theta}(t_i) = \frac{\epsilon\tilde{\theta}(t_{i-1}) + \epsilon T\tilde{\omega}(t_{i-1}) + \alpha_1 T\theta(t_i)}{\epsilon + \alpha_1 T} \\
\tilde{\omega}(t_i) = \tilde{\omega}(t_{i-1}) + \frac{\alpha_2 T}{\epsilon}(\theta(t_i) - \tilde{\theta}(t_i))
\end{cases}
\tag{4.1}
$$
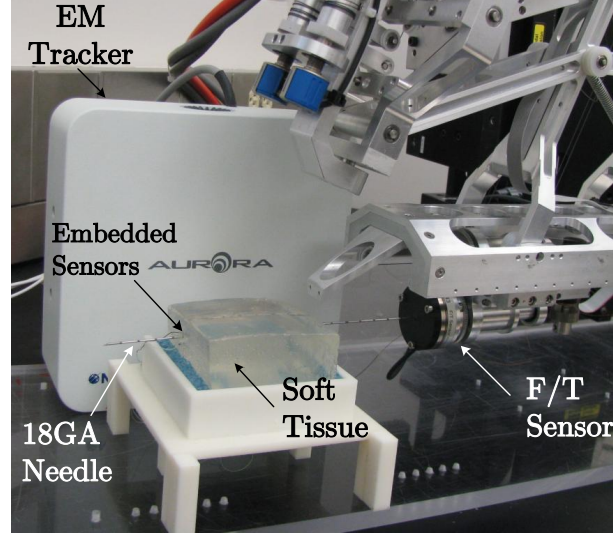
Figure 4.1: The 5-DOF robotic system and embedded EM tracker sensors for needle insertion/steering.

In (4.1), α_1 and α_2 are chosen such that $H(s)=s^2 + \alpha_1 s + \alpha_2$ is a Hurwitz polynomial, and ϵ is set to be 1. In this system, $\tilde{\omega}$ can be replaced with kv where v is the estimated velocity of the robot's distal assembly, and k is a constant value [15]. Thus, using the Z-transform, $V(z)$ is expressed as $V(z)=\Psi(z;\alpha_1,\alpha_2)\Theta(z)$ where Ψ is the discrete transfer function of the observer dynamics in (4.1).

$$\Psi(z;\alpha_1,\alpha_2) = \frac{\alpha_2 T z(z-1)}{(\epsilon + \alpha_1 T)z^2 + (\alpha_2 T^2 - \alpha_1 T - 2\epsilon)z + \epsilon} \tag{4.2}$$

The following strategy is proposed to be combined with the LuGre-based friction model. This simple technique allows us to formulate translational friction in terms of the insertion rate, and include the effect of relative tissue motion. Note that friction effects in general depend on the relative velocity between moving contacts. That is why applying the LuGre model directly to the insertion force and needle velocity information does not generate an acceptable solution. For example, it cannot represent the existing wide gap around the origin that stems from soft tissue motion. Hence, we require estimation of needle-tissue relative velocity.

Here is the suggested refiltering routine: At first, the original force-velocity loop in terms of v_f is projected to a new space versus v_s using a slow observer. v_f is the outcome of the observation using the vector $\underline{p}_f=[\alpha_{1f},\alpha_{2f}]^T$ that defines a fast observer to track the needle

axial motion. v_s also denotes the relative velocity of the moving needle with respect to the deformed tissue. The parameter $\underline{p}_s = [\alpha_{1s}, \alpha_{2s}]^T$ defining the slow observer is chosen such that the converted empirical friction-velocity loop in the v_s domain is centered around the origin. The relationship between v_f and v_s is denoted by (4.3). Note that tuning the second observer requires a few attempts, but it is an easy task. Then, the LuGre-based structure is built based on the transformed force-velocity cycle using v_s and the measured force signals. Finally, the sought force-velocity mapping in the v_f domain is reconstructed taking the inverse Z-transform indicated by (4.3), and projecting the outcome of the LuGre model to the original force-velocity space.

$$\Theta(z) = \frac{V_f(z)}{\Psi(z; \underline{p}_f)} = \frac{V_s(z)}{\Psi(z; \underline{p}_s)} \Rightarrow v_f(t_i) = Z^{-1}\left\{ V_s(z) \frac{\Psi(z; \underline{p}_f)}{\Psi(z; \underline{p}_s)} \right\} \tag{4.3}$$

4.3 Experimental Validation

4.3.1 Setup Description

An experimental implementation of the proposed approach was carried out on the double parallelogram robotic system [15] described in Appendix A (see Fig. 4.1). In the experiments, force data are acquired at the rate of 200Hz while the EM tracker is updated at the rate of 40Hz. Note that the EM tracker is used to evaluate the motion estimation technique.

4.3.2 Experiments and Results

We conducted multiple insertions using a standard 18GA prostate brachytherapy needle (Bard Medical). Validation was performed on the following artificial phantoms: 1) gelatin, 5% concentration, 2) Gelrite Gellan Gum (Sigma-Aldrich), 2% concentration in water. These phantoms simulate an elastic environment. However, gelatin is expected to replicate pure biological tissues better than the Gellan gum since it is an organic artificial material whose main ingredients are bone and skin of pig.

Each tissue sample was placed into a container and clamped such that the bottom of the tissue was rigidly fixed, leaving the sides free to move and unobstructed for needle insertion. Three sensor coils were manually embedded in each phantom at equal vertical distances

Figure 4.2: A schematic of the experimental setup and embedded EM tracker sensors inside soft tissue.

from the needle shaft (see Fig. 4.2). In this configuration, sensors 1 and 2 were located very close to the entry and exit points of the needle, and sensor 3 was placed 10mm deeper inside soft tissue compared to sensor 2. The height parameter $\tilde{h}$ was initially adjusted to 50mm, while the phantom was fabricated at the total height of 60mm. A sinusoidal trajectory was applied to insert and withdraw the needle. The amplitude and frequency of this reference signal were set to 40mm and 0.1Hz, respectively; however, this selection was a matter of a few tests to get an initial insight into needle-tissue interaction. The acquired signals were studied over 4 periodic cycles, and using Kalman filtering, the axial velocity of each embedded sensor was extracted from displacement readings. Henceforth, tissue displacements and insertion forces are respectively expressed in the z-direction of the tip and the base frames marked by ⊛ and ⊙ signs in Fig. 4.2. In addition, we assumed for simplicity that both observers were critically damped systems, i.e., $\alpha_{2f}=\alpha_{1f}^2/4$ and $\alpha_{2s}=\alpha_{1s}^2/4$.

Applying the procedure introduced in section 4.2, the loops shown in Fig. 4.3 were obtained in gelatin. Initially, by trial and error and setting α_{1s} to 9, the first empirical loop in Fig. 4.3(a) was transformed to the one in Fig. 4.3(b). The LuGre friction model was then identified using the converted loop, and the model's output was mapped to the first space afterwards. To validate whether v_s was a good estimate of needle-tissue relative velocity, let us focus on the EM tracker measurements in the next plots. Fig. 4.4(a) presents the measured tissue displacement at sensor locations, and Fig. 4.4(b) demonstrates tissue velocity at those points. Repeating the experiments at a number of different insertion points, sensors 2 and 3 reported the minimum and maximum amount of displacement, respectively, while

Figure 4.3: Experimental and identified friction-velocity cycle with needle-tissue motion compensation in gelatin versus (a) v_f (b) v_s using $\underline{p}_f = [40, 400]^T$ and $\underline{p}_s = [9, 20.25]^T$ ($\tilde{h} = 50$mm).

sensor 2 recorded the slowest tissue motion. This observation suggested that soft tissue did not deform uniformly along the insertion path. The next subgraph, Fig. 4.4(c), displays all velocity components in this problem including needle velocity v_f, needle-tissue relative velocity v_s estimated by the tuned slow observer, and needle-tissue relative velocity approximated from EM tracker measurements that could be defined as $v_{comp,i} = v_f - v_i$ where v_i is the estimated velocity of each sensor ($1 \leq i \leq 3$). Presented results confirm that there exists a close agreement between v_s and the actual velocities provided by each EM tracker sensor. Throughout these experiments, the best match was found between v_s and $v_{comp,3}$.

In an extended test, insertions were performed at a lower level so $\tilde{h}$ was readjusted to 40mm. As expected, deformation magnitude reduced since the insertion path shifted down towards the firmly fixed edges of tissue container; however, the tracking procedure performed well to capture the needle-tissue relative velocity and frictional effects. Due to the complexity of the trends in general, investigating the practical impacts of incision location and tissue boundary conditions on interaction dynamics will be considered for future work. It is observed in Fig. 4.2 that tissue attachments at the walls on the both sides of the container are not identical; so it is expected that sensors 1 and 2 would experience different deformations (see Fig. 4.4(a)).

In the next step, an agar phantom was tested. Due to the rigidity of agar in comparison to gelatin, in this case the sample was only slightly deformed. Thus, as a result of limited measurement accuracy, it was impossible to evaluate the precision of tissue motion estima-
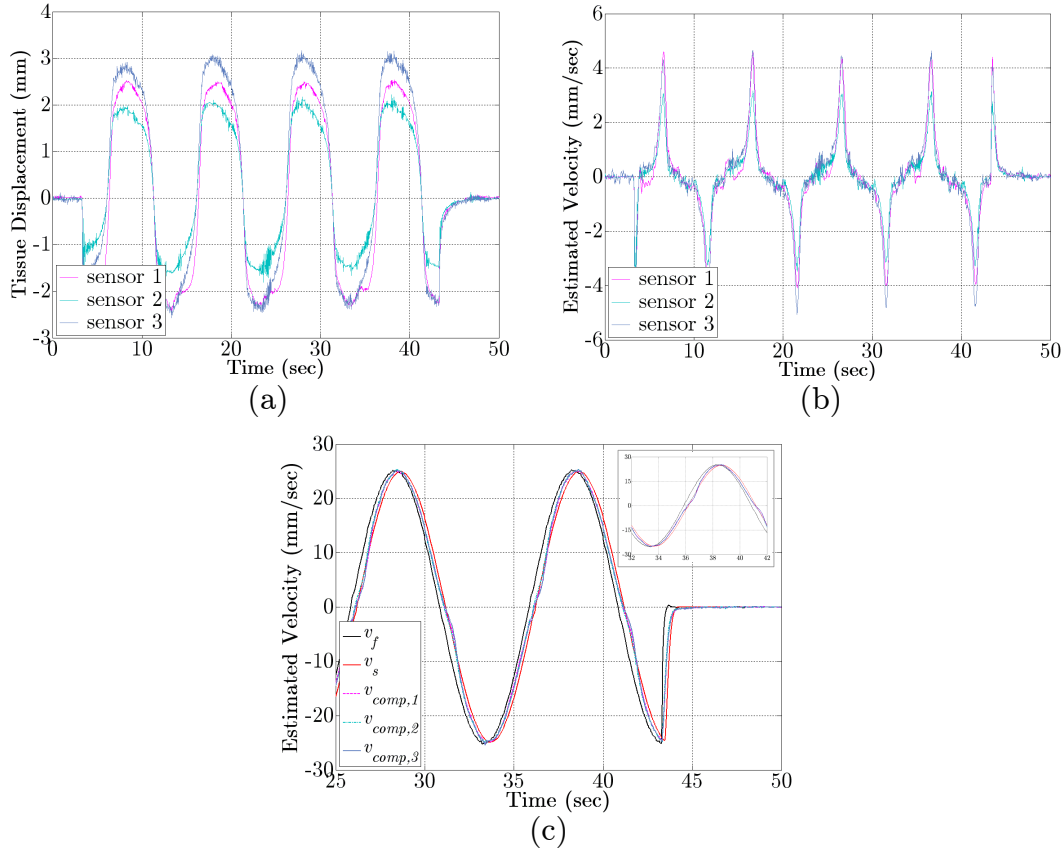
Figure 4.4: (a) Relative displacements with respect to initial condition in gelatin (b) estimated tissue axial velocity at sensor locations (c) approximated needle insertion rate and needle-tissue relative velocities extracted from the friction test and sensory measurements ($\tilde{h}$ =50mm).

tion using the EM tracker. Nevertheless, the method performed well in practice. Fig. 4.5 shows the estimated friction in the agar test in which tissue relative motion was compensated by setting α_{1s}=22 in the slow observer. As can be seen, the distributed friction was accurately predicted using the proposed mechanism. Due to space limitations, only this graph is included here.

Finally, to make a frequency-domain analysis, let us revisit $H(z)=\frac{\Psi(z;\underline{p}_s)}{\Psi(z;\underline{p}_f)}$ in (4.3) where $\underline{p}_f$ was set to $[40, 400]^T$ and $\underline{p}_s=f(\alpha_{1s})$ was subject to change depending on tissue properties. Fig. 4.6 shows the Bode plots of the transfer function H for three values of α_{1s} parameter. As shown, a smaller α_{1s} value, which is associated with a more deformable soft material, results in a higher amplitude attenuation as well as a greater phase lag with respect to the needle velocity. In this case, at f_{in}=0.1Hz (excitation frequency) in gelatin where α_{1s}=9,
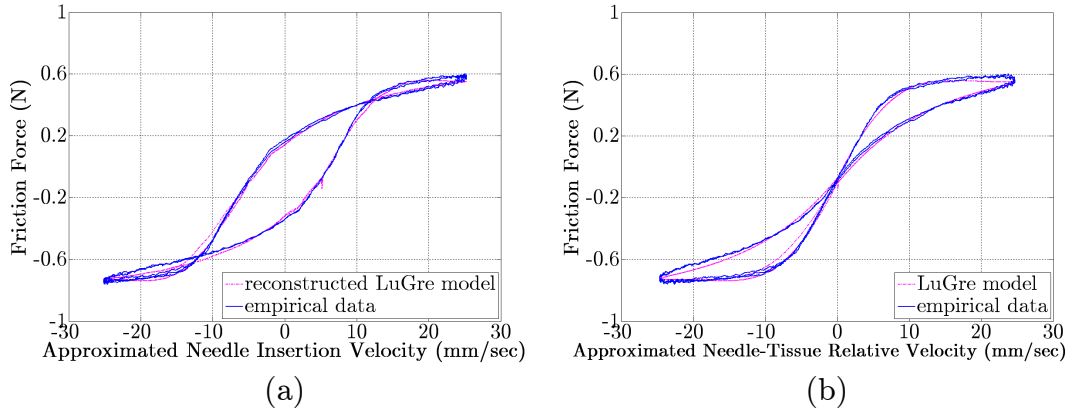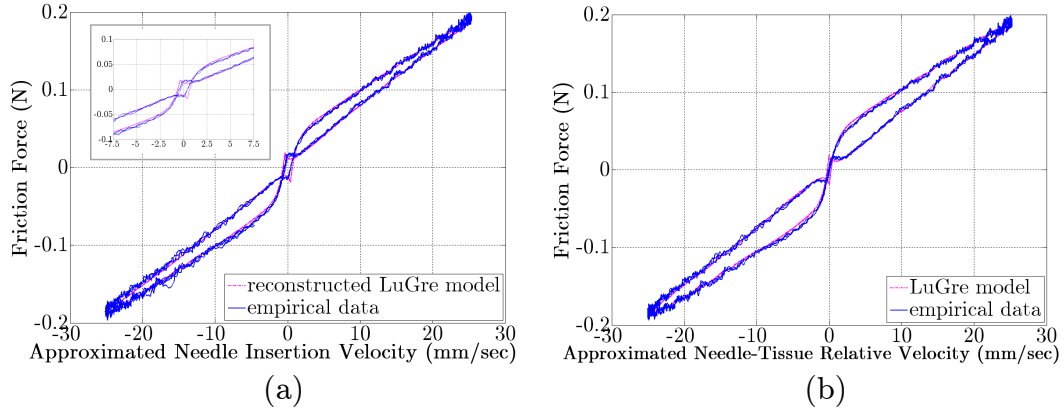
Figure 4.5: Experimental and identified friction-velocity cycle with needle-tissue motion compensation in agar versus (a) v_f (b) v_s using $\underline{p}_f = [40,\ 400]^T$ and $\underline{p}_s = [22,\ 121]^T$ ($\tilde{h}$ =50mm).
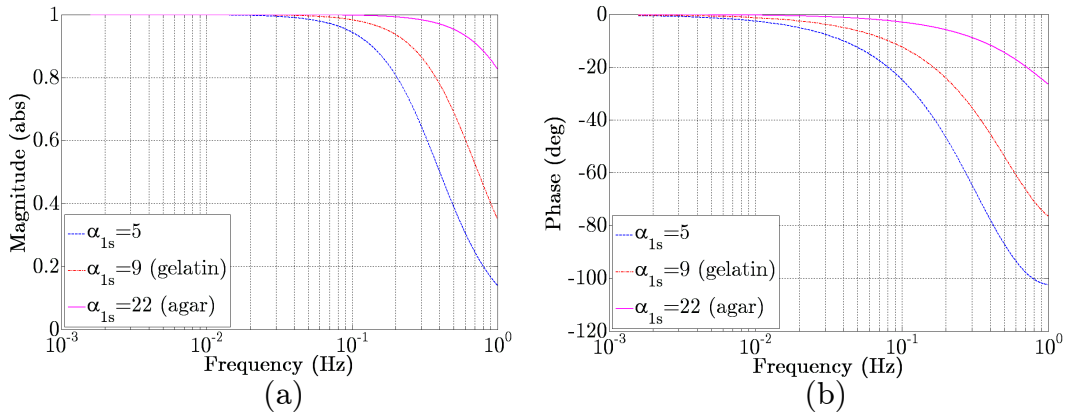
Figure 4.6: Bode plots of $H(z)$: (a) magnitude (b) phase.

signal attenuation and phase delay were respectively obtained as 1.67% and 12.36°. These quantities for the agar phantom were 0.19% and 2.99°, respectively. Note that based on Fig. 4.4(c), $v_{comp,3}$ lagged v_f by approximately 10.13°, implying that the key to accounting for tissue motion is to model and later introduce this phase delay into the reference velocity signal as we have done in this study.

4.4   Conclusions and Future Work

The main advantage of the proposed velocity estimator is its simplicity while preserving accuracy. This velocity observer now in conjunction with the previously developed friction

model can accommodate soft-tissue deformation. Thus, the entire scheme is more general and applicable to various needle-tissue combinations without excessive complexity or cost. In this application, no image-based technique was utilized; thus, imaging challenges, e.g., segmentation, artifact minimization, etc. were avoided. Nevertheless, recent advances in Graphic Processing Units (GPUs) have revolutionized computer vision and facilitated fast implementation of complex imaging algorithms.

One possible point to consider for future improvements of the relative-velocity model is to make it adaptive rather than to tune it preoperatively. Work is also in progress to validate the results via *ex-vivo* experiments using animal organs, e.g., liver, and lung. Ultimately, a full model of friction is expected to be incorporated into motion planners [3–5] in order to improve targeting accuracy in clinical practice. Ongoing research towards this goal is reported in [16] in which only viscous friction was involved to account for needle deflection. On the other hand, surgical simulators are gaining interest in medical and residency training programs. It is very likely that a novice trainee inserts and retracts a needle several times to accomplish a designated task. Thus, inclusion of a bilateral force model with the hysteresis loop which was studied here may enhance haptic perception.

Bibliography

[1] T.J. Carter, M. Sermesant, D.M. Cash, D.C. Barratt, C. Tanner, and D.J. Hawkes, "Application of Soft Tissue Modelling to Image-Guided Surgery," *Med. Eng. Phys.*, vol. 27, pp. 893-909, 2005.

[2] J. Ma, *et al.*, "Accuracy of Non-Linear FE Modelling for Surgical Simulation: Study Using Soft Tissue Phantom," *Comp. Biomec. Med.*, part 1, pp. 29-41, 2010.

[3] A. Haddadi, K. Hashtrudi-Zaad, "Development of a Dynamic Model for Bevel-Tip Flexible Needle Insertion into Soft Tissues," *In Proc. of 33rd IEEE EMBS Annu. Int. Conf.*, 2011, pp. 7478-7482.

[4] N.A. Wood, K. Shahrour, M.C. Ost, and C.N. Riviere, "Needle Steering System Using Duty-Cycled Rotation for Percutaneous Kidney Access," *In Proc. of 32nd IEEE EMBS Annu. Int. Conf.*, 2010, pp. 5432-5435.

[5] R. Alterovitz, M. Branicky, and K. Goldberg, "Motion Planning under Uncertainty for Image-Guided Medical Needle Steering," *Int. J. Rob. Res.*, vol. 27, no. 11-12, pp. 1361-1374, 2008.

[6] A. Majewicz, T.R. Wedlick, K.B. Reed, and A.M. Okamura, "Evaluation of Robotic Needle Steering in *ex vivo* Tissue," *In Proc. of IEEE Int. Conf. on Rob. Autom. (ICRA)*, 2010, pp. 2068-2073.

[7] S.P. DiMaio, S.E. Salcudean, "Needle Insertion Modeling and Simulation," *IEEE Trans. Robot. and Autom.*, vol. 19, 2003, pp. 864-875, 2003.

[8] J.R. Crouch, C.M. Schneider, J. Wainer, and A.M. Okamura, "A Velocity-Dependent Model for Needle Insertion in Soft Tissue," *In Proc. of Medical Image Computing and Computer Assisted Intervention (MICCAI)*, 2005, pp. 624-632.

[9] E. Dehghan, X. Wen, R. Zahiri-Azar, M. Marchal, and S.E. Salcudean, "Parameter Identification for a Needle-Tissue Interaction Model," *In Proc. of 29th IEEE EMBS Annu. Int. Conf.*, 2007, pp. 190-193.

[10] J.T. Hing, A.D. Brooks, and J.P. Desai, "A Biplanar Fluoroscopic Approach for the Measurement, Modeling, and Simulation of Needle and Soft-Tissue Interaction," *Med. Image Anal.*, vol. 11, pp. 62-78, 2007.

[11] Y. Kobayashi, T. Sato, and M.G. Fujie, "Modeling of Friction Force based on Relative Velocity between Liver Tissue and Needle for Needle Insertion Simulation," *In Proc. of 32nd IEEE EMBS Annu. Int. Conf.*, 2009, pp. 5274-5278.

[12] A.M. Okamura, C. Simone, and M.D. O'Leary, "Force Modeling for Needle Insertion into Soft Tissue," *IEEE Trans. Biomed. Eng.*, vol. 51, pp. 1707-1716, 2004.

[13] A. Asadian, R.V. Patel, and M.R. Kermani, "A Distributed Model for Needle-Tissue Friction in Percutaneous Interventions," *In Proc. of IEEE Int. Conf. on Rob. Autom. (ICRA)*, 2011, pp. 1896-1901.

[14] H. Khalil, "Adaptive Output Feedback Control of Nonlinear Systems Represented by Input-Output Models," *IEEE Trans. Autom. Control*, vol. 41, no. 2, pp. 177-188, 1996.

[15] H.S. Bassan, R.V. Patel and M. Moallem, "A Novel Manipulator for Percutaneous Needle Insertion: Design and Experimentation," *IEEE/ASME Trans. Mechatron.*, vol. 14, no. 6, pp. 746-761, 2009.

[16] A. Asadian, M.R. Kermani, and R.V. Patel, "An Analytical Model for Deflection of Flexible Needles During Needle Insertion," *In Proc. of IEEE/RSJ Int. Conf. on Intel. Rob. Sys. (IROS)*, 2011, pp. 2551-2556.

Chapter 5

An Analytical Model for Deflection of Flexible Needles During Needle Insertion

The material presented in this chapter has been published in the Proceedings of the IEEE/RSJ International Conference on Intelligent Robots and Systems (IROS), pp. 2551-2556, USA, 2011.

5.1   Introduction

Accurate minimally invasive interventions for medical diagnosis and therapeutic procedures using surgical needles is a challenging task. Flexible needles can be utilized for brachytherapy (primary application), anaesthesia, tissue/fluid sampling, ablation, neurosurgery, and deep brain stimulation particularly in regions that are difficult to access. The flexibility enables us to create curvatures along the path in order to avoid collisions with obstacles or anatomical structures. Any deviation of the needle tip from its intended targeted area can reduce the effectiveness of the therapy or biopsy and cause further complications, e.g., tissue damage, under/over dosing, and misdiagnosis [1].

There is not a defined tolerance for the accuracy of tip positioning in clinical practice, but, precise placement of the tip is a difficult task due to several reasons. Needle-tissue interaction leads to tissue deformation and needle deflection. On top of that, lack of adequate sensing and maneuverability impedes finding a straightforward planning solution. Thus, surgeons may require several steering attempts in order to accurately place the needle tip. To date, researchers have explored a number of methods to improve the process of insertion and steering in soft tissue using robotic systems, and sophisticated modeling or image-guided techniques [1–6, 11]. In this respect, deformation modeling is of interest in machine vision and surgical simulation. Soft tissue is inhomogeneous and exhibits non-linear and anisotropic behavior in general; therefore, its modeling is a common challenge for real-time applications that cannot afford significant computation time. Misra et al. [3] provided a comprehensive survey on tool-tissue interaction models in surgical simulations.

On the other hand, dynamic response analysis of beams on foundations under moving loads has been the subject of considerable research effort in transportation systems [7]. Bridges, rails and pipelines manifest important examples of beam-like structures that are designed to support moving loads. In the current work and borrowing from advanced modeling techniques utilized in vibration [8,9], we focus on a Green's function approach and develop a deflection model that is directly linked to the interaction forces experienced by the needle during insertion. This study is in connection with robot-assisted needle steering that is intended to guide the needle to specific targeted areas inside soft tissue.

5.2   Prior Work

Past work has shown that deflection of flexible long needles is affected by the beveled shape of the needle tip and the mechanical properties of soft tissue. In this regard, Abolhassani and Patel [10, 11] modeled an 18-gauge needle with a beveled tip as a cantilever beam, but ignored the vertical component of friction along the insertion depth. They solved the bending-moment equation in the static regime. However, their assumption is not valid when the needle is very flexible, or stiction affects bending. Goksel et al. [12], developed two models using Finite Element Modeling (FEM) and a series of rigid bars connected by angular springs. They simulated bending of a standard prostate brachytherapy needle by hanging scaling weights at the needle tip, and identified unknown spring constants and Young's modulus. Finally, it was concluded that the angular springs model demonstrated

a better accuracy and computational efficiency. One major challenge in utilizing FEM for intraoperative control is the large number of state variables which in turn contributes to an ill-conditioned control problem.

An extensively used model developed by Webster et al. [13] consists of experimental kinematic model for steering a flexible beveled-tip needle in a rubber-like plastic phantom (relatively rigid tissue). According to this "bicycle/unicycle" model and ignoring friction and tissue deformation, the needle tip acts like a bicycle with locked handlebars while it moves along a fixed arc. Misra et al. [14] presented an energy-based model influenced by macroscopic and microscopic observations of needle-gel interaction. They calculated the needle deflection, and compared the energy associated with each stage of the interaction. Their results indicate that the energy of the interaction stiffness dominates the total energy. Majewicz et al. [15] experimentally investigated the effect of insertion velocity, bevel angle, and shaft diameter on curvature of the bicycle model. They statistically showed that the curvature decreased as the diameter increased. They also found no significant trend for the tip angle possibly due to the high level of viscoelasticity of the examined tissue.

Developing a bending model, needle base manipulation mechanisms could be applied to steer a flexible needle inside soft tissue [4–6]. Steerability is provided by asymmetric forces acting at the needle tip, but the accuracy of a model-based planning strategy relies on the validity of the employed deflection model. In this regard, a mechanics-based model similar to the proposed approach is important in practical implementations since it can be easily integrated in a feedback system for real-time control. This fact has motivated the present study as a means of developing an accurate and feasible bending model for use in intraoperative tasks.

A possible extension of the current modeling studies is to take the impact of tissue elasticity and distributed friction simultaneously into account in a dynamic fashion. The present analysis is based on the theory of beams which is accurate for slender beams whose cross sections do not undergo extreme deformation during deflection. In this study, the effect of interaction stiffness is incorporated by assuming an elastic environment across the needle shaft. Elasticity is denoted by a large number of closely-spaced translational virtual springs that act as a continuous support to the beam. Static friction mapping is also included in the deflection equations in order to develop a novel bending model.

This chapter is organized as follows. Section 5.3 gives details of the proposed modeling
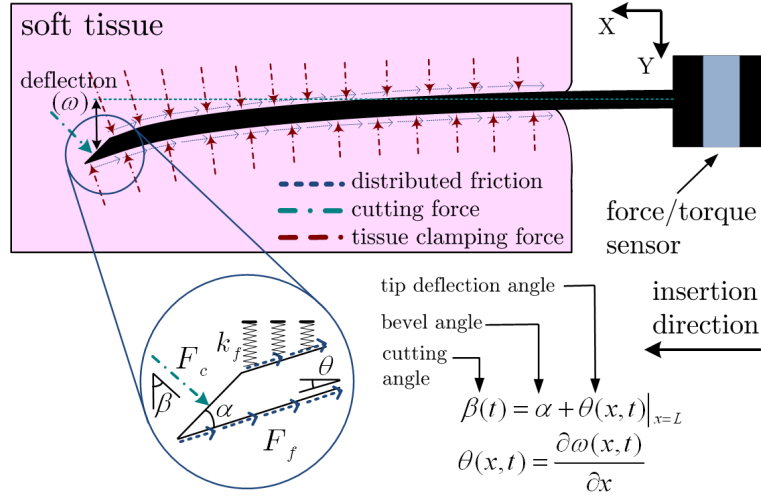
Figure 5.1: Effective forces acting on the curved shaft and 2D needle deflection with respect to its insertion depth.

scheme. In section 5.4, experimental results are discussed, and conclusions and suggestions for future work are presented in section 5.5.

5.3 The Proposed Dynamic Modeling Scheme for Planar Needle Deflection

In this section, an analytical method is proposed to study a cantilever beam with application in needle insertion. The simple static Euler-Bernoulli beam theory was studied in [10, 11]. In [10], the cutting force was modeled as a concentrated point load applied to the needle tip, and tissue resistance forces were assumed to cancel each other. In [11], tissue resistance force along the needle shaft was modeled as a triangularly distributed load with maximum intensity at the entry point. Using the method of superposition, the bending was then obtained. However, later on due to the use a pretty thick needle, the tissue resistance was found to be of little impact; thus, it was ignored from deflection calculations.

To describe the proposed scheme, Fig. 5.1 helps us to get more insight into the planar bending of a flexible needle surrounded by soft tissue. In this scheme, the compressive force exerted by tissue is perpendicular to the needle shaft, and acts as a normal force that yields tangential distribution friction F_f along the tube. Unbalanced tip force F_c applied

normal to the surface of the asymmetric tip is another bending factor that causes the flexible
structure to deflect in the direction of the asymmetry. Thus, the needle can be considered
as a partially loaded moving cantilever.

As a basis for the current analysis, let us assume that a single Euler-Bernoulli beam rests
on an elastic foundation, and it is subjected to a distributed external moving load. The
transversal load intensity is denoted by $f(x, t)$, and x stands for the axial distance from
the base holder, the origin of the coordinate frame. The partial differential equation (PDE)
governing the forced transverse motion of the neutral axis is given by [16]

$$\frac{\partial^2}{\partial x^2}(EI\frac{\partial^2\omega(x,t)}{\partial x^2}) + \rho A\frac{\partial^2\omega(x,t)}{\partial t^2} + k_f\omega(x,t) = f(x,t) \tag{5.1}$$

where $\omega(x, t)$ is the transversal displacement along the y direction. E and ρA are Young's
modulus and the mass per unit length of the beam, respectively. I is the cross-sectional
moment of inertia about the y-axis, and k_f is the load per unit length of the beam that
causes the foundation to deflect by a unit amount. This parameter is a function of tissue
elasticity.

Referring to Fig. 5.1, the needle can be split into a number of spans, and the needle
curvature can be approximated by a set of linear sub-beams. Toward this goal, it is re-
quired to find an appropriate spacing of the spans, associated support types as well as the
shape/direction of beam-environment contact force density functions or support stiffness
values.

As depicted Fig. 5.1, the first span can be part of the needle that lays outside of tissue.
The rest of the needle from the entry point to the tip point behaves as the second sub-
beam. Thus, the needle is comprised of two uniform beams connected together at the
entry point. Each sub-beam is itself an Euler-Bernoulli beam which satisfies (5.1). To find
sub-boundary conditions, we know that the first segment is clamped at the needle holder
whereas the second one has a free end, and it is subject to distributed interaction forces. On
the other hand and as a result of continuity, both segments undergo the same deflection and
slope, and they also experience the same amount of shear force and bending moment at the
connection point. Hence, the assumptions lead to the following sets of sub-conditions. For

the first section ($0 \leq x \leq l_1$), we have

$$\omega_1(0, t) = 0, \qquad \frac{\partial \omega_1}{\partial x}(0, t) = 0$$

$$\frac{\partial^2 \omega_1}{\partial^2 x}(l_1, t) = \frac{\partial^2 \omega_2}{\partial^2 x}(l_1, t), \qquad \frac{\partial^3 \omega_1}{\partial^3 x}(l_1, t) = \frac{\partial^3 \omega_2}{\partial^3 x}(l_1, t)$$

(5.2)

while for the second section ($l_1 \leq x \leq L = l_1 + l_2$),

$$\omega_1(l_1, t) = \omega_2(l_1, t), \qquad \frac{\partial \omega_1}{\partial x}(l_1, t) = \frac{\partial \omega_2}{\partial x}(l_1, t)$$

$$\frac{\partial^2 \omega_2}{\partial x^2}(L, t) = 0, \qquad EI \frac{\partial^3 \omega_2}{\partial x^3}(L, t) = F_c(t) cos\beta(t)$$

(5.3)

where the subscript i indicates the segment number, and l_i denotes the segment length. L is also the needle length, and $x = l_1$ corresponds to the skin entry point. Moreover, both sections start from rest thus ($i = 1, 2$)

$$\omega_i(x, 0) = 0, \qquad \frac{\partial \omega_i}{\partial t}(x, 0) = 0$$

(5.4)

Herein, $F_c(t)$ represents the estimated cutting force density that acts as a contact force at the tip and thereby playing as a bending factor. $\beta(t)$ is the effective angle of cutting that can be adjusted by adding the bevel angle α to the preceding instant of the tip deflection angle θ_{tip}. Initially, the needle is unbent thus $\theta_{tip}(t = 0) = \frac{\partial \omega_2}{\partial x}(L, 0) = 0$.

To complete the right-hand-side of equation (5.1), it is worth noting that in the absence of needle-tissue interaction, for instance in the first segment, the stiffness coefficient is set to zero. The external load is also formulated as (5.5) where F_f is the estimated friction force density. A separate procedure has been outlined to deal with distributed dynamic friction [17]. To ease the analysis, only the vertical component of the viscous term denoted by the viscous coefficient v_f is included in the present model.

$$f(x, t) = \begin{cases} 0 & 0 \leq x < l_1 \\ F_f sin\theta(x, t) & l_1 < x \leq L \end{cases}$$

(5.5)

For sufficiently small cutting angles, $sin\theta \approx \theta$, so this approximation simplifies the derivation of the solution to a great extent. For $\theta \leq 25^\circ$ that is the case, the error is at most 3% which is quite acceptable. In view of the small angle approximation, the force boundary

condition at the tip expressed by (5.3) is revised as below.

$$EI\frac{\partial^3 \omega_2}{\partial x^3}(L,t) = F_c(t)cos\alpha - F_c(t)sin\alpha\frac{\partial \omega_2}{\partial x}(L,t) \tag{5.6}$$

Replacing (5.5) into the main PDE (5.1), and using the small angle approximation result in the following PDEs in which F_f is replaced by $v_f v$ where v is the insertion velocity.

$$EI\frac{\partial^4 \omega_1(x,t)}{\partial x^4} + \rho A\frac{\partial^2 \omega_1(x,t)}{\partial t^2} = 0, \quad 0 \le x < l_1 \tag{5.7}$$

$$EI\frac{\partial^4 \omega_2(x,t)}{\partial x^4} + \rho A\frac{\partial^2 \omega_2(x,t)}{\partial t^2} + k_f\omega_2(x,t) = v_f v\frac{\partial \omega_2}{\partial x}(x,t), \quad l_1 < x \le L \tag{5.8}$$

As observed, direct inclusion of F_c and F_f into the sub-boundary conditions and the resulting PDEs incorporates the effect of interaction forces, i.e., cutting force and distributed friction, in the final solution. Knowing the value of v_f and estimating the preceding shape of the curvature, $F_c(t)$ can be directly related to the measured force in the axial direction. The term $k_f\omega(x,t)$ also takes tissue resistance into account, and models small tissue deformation in the direction of deflection. Therefore, the proposed approach is expected to be theoretically adequate to characterize the deflection of flexible needles in soft tissue in percutaneous interventions.

Due to the geometry of this problem and having moving boundary conditions, finding the solution is not as straightforward as standard beam-based forms extensively studied in text books [7, 16]. Applying the method of separation of variables as a common technique [16, 18] yields no time-independent modal solution for the second PDE (5.8); thus, this method is not applicable to this case. Instead, using a Green's function approach provides us the closed-form solution in an integral form in a computationally efficient manner [7–9]. In this method, the boundary conditions are embedded in Green's functions, and it is not necessary to solve the free vibration problem in order to obtain the eigenvalues and the corresponding eigenfunctions. In a truncated series solution, finding the eigenfunctions is required, and numerical convergence between two consecutive samples is not guaranteed in a moving variable-length beam.

To start, notice that a PDE with non-homogeneous boundary conditions, e.g., the second

Table 5.1: Coefficients of the Quasi-Static Solution

c_3	c_2	c_1	c_0
$\frac{cos\alpha}{6EI-3L^2F_c sin\alpha}$	$\frac{-3Lcos\alpha}{6EI-3L^2F_c sin\alpha}$	0	0

PDE (5.8), can always be converted to a non-homogeneous PDE with homogeneous bound-
ary conditions [18]. The key point here is to define a transformation from the original
equation to the new PDE that satisfies homogeneous boundary conditions. To this end, the
desired solution for instance for the second sub-beam, namely $\omega_2(x,t)$, can be rewritten as

$$\omega_2(x,t) = \tilde{\omega}(x,t) + \phi(x,t) \tag{5.9}$$

where $\phi(x,t)$ is the simplest function that satisfies the non-homogeneous boundary condi-
tions as its counterpart, $\omega_2(x,t)$, does. For this purpose and to satisfy four existing con-
straints, a third-order polynomial can be chosen as below

$$\phi(x,t) = (c_3x^3 + c_2x^2 + c_1x + c_0)F_c(t) = C(x)F_c(t) \tag{5.10}$$

The coefficients of $C(x)$ are calculated such that $\phi(x,t)$ satisfies the non-homogeneous
boundary condition implied by (5.6). Table 5.1 lists the coefficients obtained in this way.
Considering the fact that both $\omega_2(x,t)$ and $\tilde{\omega}(x,t)$ satisfy the same boundary conditions,
it is easy to show that $\tilde{\omega}(x,t)$ satisfies a set of homogeneous boundary conditions that are
identical to (5.3) when $F_c(t)cos\alpha$ is set to 0 in (5.6). Thus, (5.8) is rewritten in terms of
$\tilde{\omega}(x,t)$ as

$$EI\frac{\partial^4\tilde{\omega}(x,t)}{\partial x^4} + \rho A\frac{\partial^2\tilde{\omega}(x,t)}{\partial t^2} - v_f v\frac{\partial\tilde{\omega}}{\partial x}(x,t) + k_f\tilde{\omega}(x,t) = v_f v\frac{dC(x)}{dx}F_c(t)$$
$$-k_fC(x)F_c(t) - \rho AC(x)\frac{d^2F_c(t)}{dt^2} = \tilde{f}(x,t), \quad l_1 < x \le L \tag{5.11}$$

Note that the above procedure is also followed for the first segment. As obtained for
$x \in [0,l_1)$, the effective force term is $-\rho AC(x)\frac{d^2F_c(t)}{dt^2}$, but as the needle penetrates tis-
sue, $\tilde{f}(x,t)$ comes into practice, and the governing equation for $x \in (l_1,L]$ switches to
(5.11). $\tilde{f}(x,t)$ denotes the right-hand-side of equation (5.11).

Now, the dynamic Green's function method can be utilized to find the solution of the con-

verted PDEs whose boundary conditions are homogeneous. A Green's function, named
$g(x, \tilde{x}; \phi)$, is the beam response at x produced by a unit concentrated force that acts at an
arbitrary position $\tilde{x}$ along the beam, and contains a single frequency component ϕ. Briefly,
assuming the state variable transformation of $\tilde{\omega}(x, t) = Re\{z(x)e^{i\phi t}\}$, and taking (5.11)
into account, z satisfies the next relationship that will give us g for $x \in (l_1, L]$. Here, δ is
the Dirac delta function and $i = \sqrt{-1}$.

$$EI\frac{d^4z}{dx^4} - v_f v\frac{dz}{dx} + (k_f - \rho A\phi^2)z = \delta(x - \tilde{x}) \tag{5.12}$$

To find the unknown Green's function, we employed an analogous method to what was
adopted in [8] in the Laplace domain. To this end, applying Laplace transforms to (5.12)
with respect to x, $G(s)$ for the second segment is derived as

$$G_2(s) = \frac{1}{L_2(s)} \times \left[e^{-s\tilde{x}} + (EIs^3 - v_f v)g_2(0) + EI\left(s^2 g_2'(0) + sg_2''(0) + g_2'''(0)\right)\right],$$

$$l_1 < x \leq L$$

$$\tag{5.13}$$

where $L_2(s) = EIs^4 - v_f vs + k_f - \rho A\phi^2$, and $g_2(0)$ and its derivatives are related to
the beam conditions at $x = l_1$. Similarly, for the first sub-beam, the counterpart transfer
function turns out to be (5.14) in which $L_1(s) = EIs^4 + k_f - \rho A\phi^2$, and $g_1(0)$ and the
derivatives are evaluated at $x = 0$.

$$G_1(s) = \frac{1}{L_1(s)} \times \left[e^{-s\tilde{x}} + EI\left(s^3 g_1(0) + s^2 g_1'(0) + sg_1''(0) + g_1'''(0)\right)\right], \quad 0 \leq x < l_1$$

$$\tag{5.14}$$

Finally, to calculate the g function over the entire beam, boundary conditions expressed
earlier in this section should be transformed to the g domain [8,9]. In general, only two out
of the four initial conditions stated in (5.13) and (5.14) are explicitly known. But, equiv-
alently we can presume that the needle is fixed, and the tissue is moving in the opposite
direction. As a result, continuity conditions on g and its derivatives at $x = l_1$ as the front
edge of the moving load should be satisfied [7]. This set of new constraints provide us with
the missing part of the information required to find the inverse Laplace transforms of $G_1(s)$
and $G_2(s)$. Due to the complexity of the G elements, all calculations were performed using

computer-aided techniques and MATLAB® symbolic toolbox.

The homogenous solution of the system can be eventually represented in terms of the convolution of the derived Green's function and the known external force [7, 9]. Finally, by adding the quasi-static solution introduced by $\phi(x, t)$ to the homogenous solution obtained using the residue theorem, the complete dynamic response of the beam can be derived. For example, for the second sub-beam

$$\omega_2(x, t) = \frac{1}{2\pi i} \int_{-\infty}^{+\infty} \left(\int_{l_1}^{L} g(x, \tilde{x}; \phi) \tilde{f}(\tilde{x}, t) d\tilde{x} \right) e^{i\phi t} \, d\phi + C(x) F_c(t), \quad l_1 < x \leq L$$

(5.15)

For more details on the mathematical method explained in brief, readers can refer to [7–9].

5.4 Implementation and Experiments

5.4.1 Setup Description

Experimental studies of the proposed method were carried out using the state-of-the-art robotic system [19] described in Appendix A. Experiments were carried out on an artificial phantom made from Gelrite Gellan Gum (Sigma-Aldrich) with two concentration rates in water: 4% (tissue A) and 6% (tissue B). This material simulates a uniform elastic environment, and mimics the frictional effects of biological tissues better than rubber phantoms. For the tests, the cannula of an 22-gauge stainless steel needle of length L=203mm was used. Imaging the needle tip by a trinocular microscope (Madell Technology Corp.), the bevel angle was estimated on the image as α=24.8º. The needle also had outer and inner diameters of 0.718mm and 0.413mm respectively.

5.4.2 Experimental Results

The aim of the experiments was to validate the model proposed in section 5.3. For this purpose, the estimated curve was compared with the measured deflection using the electro-

magnetic tracker. Furthermore, to investigate the effect of velocity, insertion through each phantom was performed at two different velocities which were far from the stiction.

Using a simple compression test [20], k_f was measured from the force-deformation mapping of samples of the examined phantoms with known geometries. Based on this, k_f was therefore set to 3.87kN/m^2 for tissue A and 7.65kN/m^2 for tissue B. Furthermore, the values of v_f for phantoms A and B were respectively set to 123.9Ns/m^2 and 166.7Ns/m^2 using a cone-tip version of the needle [17]. Other numerical parameters were selected as follows: ρ=8000Kg/m^2, A=2.709$\times$10^{-7}m^2, E=200GPa, and I=1.162$\times$10^{-14}m^4.

The needle tip was initially placed in contact with the phantom so that $l_1 = L - vt$. Generating a constant-velocity trajectory, it was discretized into a series of steps, and numerical integration using Gaussian quadrature rule was calculated over the length of the sub-beams at each step. Running the pivoting algorithm resulted in 9.3mm as the average distance between the tip and the coil center [21]. The position of the coil center is the actual reference point for comparison so the bending was evaluated at x_{coil}=L-9.3mm. In the conducted experiments, the maximum insertion forces for tissues A and B were measured to be 0.232N and 0.276N respectively at v=15mm/s. It was also observed that during the very first portion of insertion, the deflection curve did not follow the beam model. This discrepancy can be justified by the presence of rupture as an unmodelled phenomenon so it was taken into account when analyzing the results.

Fig. 5.2 demonstrates the empirical and the estimated deflection curve at x_{coil} for an 80mm insertion, and Table 5.2 summarizes the numerical results obtained. In the plotted graphs, the origin has been assumed to be located at the tissue entry point. As seen in Fig. 5.2, the suggested method in general exhibits acceptable performance. Taking estimation error into account, the first interpretation at this point is that the model slightly outperforms for tissue B. For tissue A, as shown in Figs. 5.2(a) and 5.2(c), there exists a gradually increasing error with increasing depth. Despite this, the maximum error that occurred at the tip area in Fig. 5.2(a) was confined to 0.374mm which is acceptable. As another result, we conclude that inserting the needle with a higher velocity or in a phantom with a lower stiffness results in a smaller radius of curvature, and thereby providing greater needle steerability. The stiffness effect agrees with the simulation results reported in [14].

Assuming a fixed radius of curvature throughout the entire intervention corresponds to the bicycle model introduced in [13], and later on widely exploited for control [4, 5, 10].
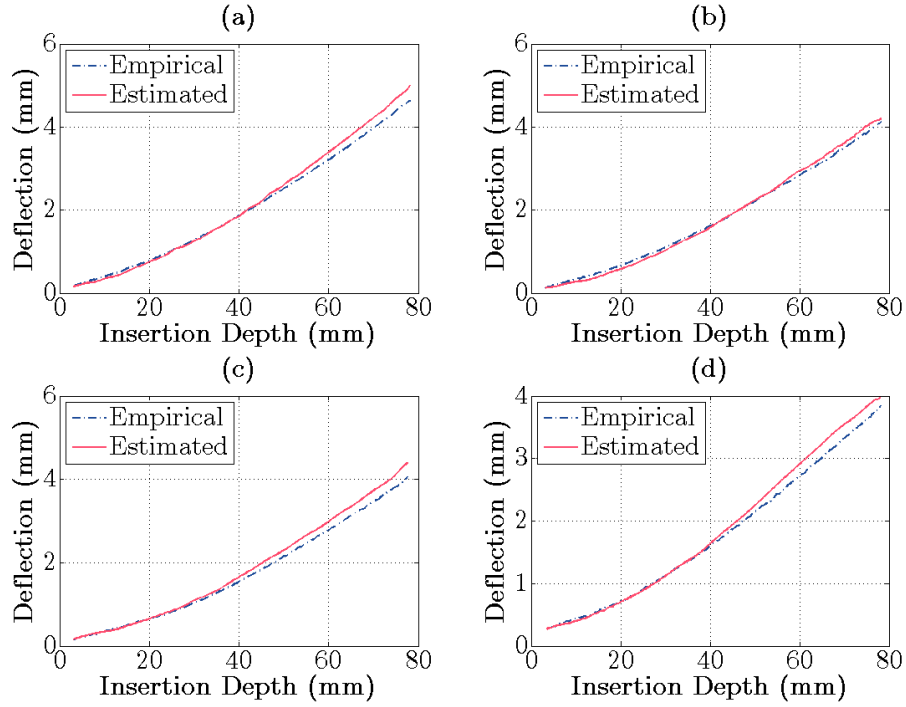
Figure 5.2: Deflection versus insertion depth: (a) v=10mm/s, tissue A; (b) v=10mm/s, tissue B; (c) v=15mm/s, tissue A; (d) v=15mm/s, tissue B.

Thus, it is an important benchmark for comparison. We utilized a least-squares method to fit a circle to each curve in order to determine the radius of curvature. Referring to Table 5.2, this parameter was underestimated by the model in the four studied cases, and its percentage error varied from 8.7% (case c) to 18.72% (case d). The percentage error is defined as the absolute prediction error divided by the measured value. Note that variation of each curvature during intervention can be related to the complex behavior of soft tissue, and entails a comprehensive biomechanical investigation. It is visible in the last 20mm and 10mm of the insertion depths in Figs. 5.2(b) and 5.2(d), respectively.

In the next test, robustness in the presence of uncertainty was assessed. The parameters k_f and v_f are the two that are most likely to be erroneous. In other words, finding or estimating their values requires further modeling simplification. Thus, it is worth finding out how the model performs when it encounters parametric uncertainty. The outcome imposes a limit on the confidence in the model response.

For this study, a $\pm$20% deviation from the nominal values was introduced in both k_f and v_f, and the deviation of the estimated radius of curvature was calculated. The results are

Table 5.2: Numerical Results of Deflection Estimation

	v=10mm/s		v=15mm/s	
	tissue A	tissue B	tissue A	tissue B
Average of absolute error (mm)	0.108	0.091	0.121	0.094
Maximum of absolute error (mm)	0.374	0.201	0.351	0.236
Measured radius of curvature (mm)	1357.6	1495.9	1247.8	1441.5
Estimated radius of curvature (mm)	1165.5	1292.7	1139.2	1171.7

Table 5.3: Percentage Error in the Radius of Curvature in the Presence of Parametric Uncertainty

	v=10mm/s		v=15mm/s	
	tissue A	tissue B	tissue A	tissue B
$\Delta k_f = +20\% k_f$	12.29	8.60	9.01	11.58
$\Delta k_f = -20\% k_f$	24.61	19.22	12.75	27.84
$\Delta v_f = +20\% v_f$	15.07	14.39	12.51	21.76
$\Delta v_f = -20\% v_f$	13.80	8.85	8.97	16.53

listed in Table 5.3. To highlight the main trends, we can say that the model was more robust to overestimation of the value of k_f rather than to underestimation of this parameter since there was less change in the amount of percentage error. In addition, the model was less sensitive to the overestimation of v_f compared with the underestimation of k_f at the examined velocities. They both have the same impact on the estimated curvature. As indicated, a 20% stiffness increase or a 20% viscosity decrease could improve the estimation performance by almost 5% for tissue B at 10mm/s. Note that due to the experimental limitation in terms of lack of versatile phantom types needed to expose a wide range of friction properties and elasticity, no general conclusion can be inferred here.

Overall, the acceptable results presented in this work proves the capability of this model to deal with needle-tissue interaction causing the needle to flex. Part of the existing discrepancy can possibly be attributed to the simplified force diagram depicted in Fig. 5.1. For example, we presumed that (1) the cutting force has a single concentrated component at the tip face; (2) the needle-tissue interaction can be described by linear elasticity with a

constant parameter k_f. However, the cutting mechanism in practice is not yet well formulated, and the interaction is influenced by complex factors, e.g., tissue inhomogeneity and viscoelasticity. On top of that, inaccurate approximation of interaction-related parameters such as k_f and v_f can lead to more deviation from reality.

5.5 Conclusions and Future Work

Flexible needles are frequently employed in clinical practice. They have a great potential to improve targeting accuracy. Work has been ongoing to develop robotic systems that can accomplish needle-based interventions. Finding an accurate model is the first step toward precise control thus the deflection model will be part of the control design. In the past bending studies [10, 11], friction as a major component present in needle-tissue interaction has been disregarded, notwithstanding that its impact on bending could be considerable in some applications. In this study, friction along the insertion depth as well as the mechanical properties of the elastic medium and insertion velocity were integrated into the Euler-Bernoulli beam element. The geometry of the studied problem led to a set of PDEs for two sub-beams with coupled non-homogeneous moving boundary conditions. Green's functions were utilized as a sophisticated means to find the sought analytical solution. Theoretical results were validated using experiments, and the experimental results confirmed that the suggested technique could open up new possibilities for deflection modeling.

For the sake of simplicity, the uniform elastic foundation was assumed to be linear in the discussion. However, nonlinear viscoelasticity and nonhomogeneity will be studied in the future to represent a more realistic behavior of needle-tissue interaction. It will enable us to extend the proposed model to biological tissues, and predict the needle path during clinical interventions. Thorough robustness tests and statistical analysis are subjects of ongoing research. Investigating the impact of dynamic friction [17] is also left for future study. Ultimately, this analytical approach is aimed at robot-assisted needle steering to improve targeting accuracy in percutaneous therapies and biopsies.

Bibliography

[1] N. Abolhassani, R. Patel, and M. Moallem, "Needle Insertion into Soft Tissue: A Survey," *Med. Eng. Phys.*, vol. 29, pp. 413-431, 2007.

[2] S.P. DiMaio, S.E. Salcudean, "Needle Insertion Modeling and Simulation," *IEEE Trans. Robot. Autom.*, vol. 19, no. 5, pp. 864-875, 2003.

[3] S. Misra, K.T. Ramesh, and A.M. Okamura, "Modeling of Tool-Tissue Interactions for Computer-Based Surgical Simulation: A Literature Review," *Presence-Teleop. Virt.*, vol. 17, no. 5, pp. 463-491, 2008.

[4] R. Alterovitz, A. Lim, K. Goldberg, G.S. Chirikjian, and A.M. Okamura, "Steering Flexible Needles under Markov Motion Uncertainty," *In Proc. of IEEE/RSJ Int. Conf. on Intel. Rob. Sys. (IROS)*, Canada, 2005, pp. 120-125.

[5] A. Asadian, M.R. Kermani, and R.V. Patel, "Robot-Assisted Needle Steering Using a Control Theoretic Approach," *J. Intell. Robot. Syst.*, vol. 62, no. 3-4, pp. 397-418, 2011.

[6] V. Duindam, J. Xu, R. Alterovitz, S. Sastry, and K. Goldberg, "Three-Dimensional Motion Planning Algorithms for Steerable Needles Using Inverse Kinematics," *Int. J. Rob. Res.*, vol. 29, pp. 789-800, 2010.

[7] L. Fryba, Vibration of Solids and Structures Under Moving Loads, Thomas Telford Ltd.; 1997.

[8] M. Abu-Hilal, "Forced Vibration of Euler-Bernoulli Beams by Means of Dynamic Green Functions," *J. Journal Sound Vibrat.*, vol. 267, pp. 191-207, 2003.

[9] S.Y. Lee, H.Y. Ke, and Y.H. Kuo, "Analysis of Non-Uniform Beam Vibration," *J. Journal Sound Vibrat.*, vol. 142(1), pp. 15-29, 1990.

[10] N. Abolhassani, R.V. Patel, and F. Ayazi, "Minimization of Needle Deflection in Robot-Assisted Percutaneous Therapy," *Int. J. Med. Robotics Comput. Assist. Surg.*, vol. 3, pp. 140-148, 2007.

[11] N. Abdolhassani, R.V. Patel, "Deflection of a Flexible Needle During Insertion into Soft Tissue," *In Proc. of 28th IEEE EMBS Annu. Int. Conf.*, USA, 2006, pp. 3858-3861.

[12] O. Goksel, E. Dehghan, and S.E. Salcudean, "Modeling and Simulation of Flexible Needles," *Med. Eng. Phys.*, vol. 31, pp. 1069-1078, 2009.

[13] R.J. Webster III, J.S. Kim, N.J. Cowan, G.S. Chirikjian, and A.M. Okamura, "Nonholonomic Modeling of Needle Steering," *Int. J. Rob. Res.*, vol. 25, no. 5/6, pp. 509-525, 2006.

[14] S. Misra, K.B. Reed, B.W. Schafer, K.T. Ramesh, and A.M. Okamura, "Observations and Models for Needle-Tissue Interactions," *In Proc. of IEEE Int. Conf. on Rob. Autom. (ICRA)*, Japan, 2009, pp. 2687-292.

[15] A. Majewicz, T.R. Wedlick, K.B. Reed, and A.M. Okamura, "Evaluation of Robotic Needle Steering in Ex Vivo Tissue," *In Proc. of IEEE Int. Conf. on Rob. Autom. (ICRA)*, USA, 2010, pp. 2068-2073.

[16] S.S. Rao, Vibration of Continuous Systems, John Wiley and Sons Inc.; 2007.

[17] A. Asadian, R.V. Patel, and M.R. Kermani, "A Distributed Model for Needle-Tissue Friction in Percutaneous Interventions," *In Proc. of IEEE Int. Conf. on Rob. Autom. (ICRA)*, China, 2011, pp. 1896-1901.

[18] R. Haberman, Elementary Applied Partial Differential Equation with Fourier Series and Boundary Value Problems, Prentice Hall; 1987.

[19] H.S. Bassan, R.V. Patel, and M. Moallem, "A Novel Manipulator for Percutaneous Needle Insertion: Design and Experimentation," *IEEE/ASME Trans. Mechatron.*, vol. 14, no. 6, pp. 746-761, 2009.

[20] K.A. Ross, M.G. Scanlon, "Analysis of the Elastic Modulus of Agar Gel by Indentation," *J. Texture Stud.*, vol. 30, no. 1, pp. 17-27, 1999.

[21] http://www.ndigital.com/medical/aurora.php

Chapter 6

Robot-Assisted Needle Steering Using a Control Theoretic Approach

The material presented in this chapter has been published in the Journal of Intelligent and Robotic Systems (Springer Verlag), vol. 62, no. 3-4, 2011, pp. 397-418. A part of this work has also been published in the Proceedings of the IEEE American Control Conference (ACC), pp. 2785-2790, USA, 2010.

6.1 Introduction

Medical intervention using flexible needles has become a common minimally invasive procedure. Facilitating curved trajectories, flexible needles could be utilized for localized drug delivery, radioactive seed placement or tissue biopsy especially in dealing with deep zones or regions that are difficult to access. Thinner needles cause less damage and trauma to the tissue. Consequently, less serious complications occur with the fine needles compared with standard coarse ones. But, it is notable that a major obstacle to use the flexible needles although having greater mobility than straight rigid needles is that they are very difficult to control and do not lend themselves to intuitive steering. Therefore, robotics-assisted needle steering, which is intended to guide the needle to specific targets inside soft tissue,

has become an active research area. To this end, a robot can be used to control the base of a flexible bevel-tip needle [1]. A desired trajectory for the needle tip is then planned such that the needle does not penetrate delicate structures such as nerves and blood vessels or collide with bones, which might lie between feasible entry points and potential targets. In this respect, targeting inaccuracy stems from complex factors such as (1) organ deformation; (2) asymmetric needle bending as a result of tissue-needle interaction forces; (3) inhomogeneity, nonlinear viscoelasticity, and anisotropy of real tissue; (4) target movement due to respiration, heartbeat or similar artifacts; (5) tiny anatomic structures which cannot be easily identified with common imaging modalities such as ultrasound or MRI.

On account of the fact that open-loop execution of model-based trajectory plans may not be feasible in most cases, extracting a model which captures the tissue-needle characteristics has to be done in advance. Thus, doing a thorough study of biophysical aspects of the problem and finding a model to describe the needle curvature are the first steps toward control. Several researchers have attempted to simplify the problem and to find a computationally efficient solution through numerical models, though such models can never perfectly mimic tissue complexities [2]. Eventually, the model is used either in fully-autonomous steering or in a teleoperation scheme as a surgeon assistant or as a training simulator [3]. In the semi-autonomous scheme, the surgeon's expertise exists in the loop, and a force control approach allows the slave system to insert the needle to the desired depth of penetration. It also gives the operator a realistic sense of the tissue so that the operator can take further actions.

With regard to modeling, mechanics-based approaches consider the kinematics of the needle through analyzing the needle geometry and the measured force/torque signals at the needle holder. Abdolhassani and Patel [4] modeled an 18Ga bevel-tip needle as a cantilever beam and estimated the amount of static deflection using Euler-Bernoulli beam theory. Ignoring tissue displacement, Webster et al. [5] developed "bicycle" and "unicycle" models for experimentally steering a flexible bevel-tip needle in relatively stiff materials, and described this motion as a nonholonomic kinematic system with Pfaffian constraints. Accordingly, tissue material can be chosen such that the needle tip acts like a small bicycle with locked handlebars while the needle moves along an arc of approximately fixed radius which is independent of velocity. None of the existing models in this category, integrate mechanical properties of soft tissue. On the other hand, most of biophysics-based models, which incorporate monitoring of elastic medium properties, may not be amenable

to real-time control or be applicable to *in vivo* tests even if a fast Finite Element Method (FEM)-based method is used. Hing et al. [6] developed a system to predict soft tissue movement and involved forces using a linear elastic FEM and ABAQUS software. Two C-ARM Fluoroscopes were used to image fiducial markers and the needle bending. Misra et al. [7] summarized a rich literature review on tool-tissue interaction modeling with application in surgical simulations. Generally speaking, FEM is accurate for small linear elastic deformations. But, its numerical efficiency relies highly on the development of effective pre and post-processing, the material parameters, and the algorithm employed for solving the equations of continuum mechanics. Several studies have looked at alternative modeling methods. Viscoelastic properties of soft tissues can be represented by rheological models, which are obtained by connecting elastic and viscous elements in serial or parallel combinations. Mass-spring-damper or spring-beam-damper models are the most common noncontinuum mechanics-based technique used in this regard. However, they exhibit limited accuracy, they may work fine for real-time simulations or robotic-assisted surgeries. In [8], two models were compared to simulate the bending of a standard brachytherapy needle. The first FEM-based model took the geometric nonlinearity into account, while the second one comprised a series of rigid bars connected by angular springs. The parameters including Young's modulus for the first model and spring constants for the second model were identified to fit each model to the experimental data. The authors concluded that the angular springs model demonstrated the highest accuracy and computational efficiency compared to the introduced versions of FEM.

Several other important issues on modeling are still open for future research. The constant challenge is to develop a computationally efficient model that can concurrently describe the behavior of organs with an acceptable accuracy. On the other hand, path planning for bevel-tip needles has been studied in several ways, most of which are applicable only to a planar situation. Steerability and needle bending are provided by asymmetric forces acting at the needle tip and tissue deformation is usually disregarded. Note that accurately planning for such steerable needles is complex, and requires solving inverse kinematics for a nonholonomic system or deriving a perfect model to capture the interaction features.

Using the idea of Dubins car, Duindam et al. [9] presented a novel 3D motion planner for rigid tissues based on explicit geometric inverse kinematics. Taking advantage of the "bicycle" model developed in [5], Alterovitz et al. [10] formulated planar needle steering as a Markov Decision Process (MDP) and applied Dynamic Programming (DP) to find

a simulation-based optimal planner. They also proposed a planning framework based on a Stochastic Motion Roadmap (SMR) that computes the path that is most likely to succeed [11]. As a basis for the current study, this method is reviewed in the next section. Reed et al. [12] utilized the same SMR planner as a high-level controller inside an integrated system. Concurrently, an image-based low-level planner was employed as an observer to estimate the pose of the needle in 2D. To enhance steerability and decreasing the curvature value, a pre-bent wire was used in the experiments. Other methods of steering have been addressed in the literature with more emphasis on the preoperative or the biophysical side of the problem rather than the control strategy. Dehghan and Salcudean [13] developed a path planning method for insertion of a rigid and straight needle into deformable tissue using FEM. The insertion point, needle heading, and needle depth were optimized by minimizing the distance between the needle and a number of target points inside the tissue. At each iteration, the best 3D line fitted to the displaced targets in the deformed tissue was employed as a candidate for the new insertion line. Incorporating soft tissue motion, needle flexibility and a linear elastostatic FEM-based model, DiMaio and Salcudean [14] introduced a manipulation Jacobian relating the base motion to the tip motion for 2D steering and then applied potential fields technique to demonstrate the tip placement and obstacle avoidance. In another study, Glozman and Shoham [15] presented a path planar using virtual springs and inverse kinematics based on the assumption of quasi-static motion. They modeled tissue-needle interaction by a combination of lateral springs distributed along the needle. As the needle shape changes, the location and orientation of the virtual springs change accordingly, and the tissue elastic modulus alters as a function of strain.

Note that even in the simplest experimental case with no external artifacts, the needle motion is governed by a nonlinear dynamics. Thus, nonlinear control or nonlinear optimization as it is proposed in this chapter is a remedy to steer the needle. To have a feasible control strategy, biophysical aspects of the problem as highlighted in the previous paragraphs should be incorporated in the solution. In this respect, some of the associated features can be described mathematically, and the rest are ignored for simplicity. Clearly, a more accurate solution requires a more complex interaction model leading to a less feasible planner. Once an efficient steering method is developed, it will be implemented on an experimental setup to (1) guide the needle inside living tissue; (2) hit the predetermined goal points; and then (3) drop the radioactive seeds at the targeted locations for brachytherapy treatment.

In order to obtain an efficient steering method in the context of control theory, this work

builds on the novel method presented by Alterovitz et al. [10, 11], and the pure theoretical framework introduced by Wingate and Seppi [19–21]. The "bicycle" model, which was originally suggested in [5], is formalized as an MDP, and the path planning task as the corresponding DP solution. In this case, the curse of dimensionality poses a major hurdle for solving the optimization problem using common numerical solvers, e.g., the value iteration. This issue is exacerbated especially in a large state space in terms of the number of states where high spatial or angular resolution is employed for better modeling. Therefore, the performance of the value iteration can be effectively improved by removing redundant states or by updating them in a proper order. In the conventional value iteration as addressed in the literature, updating states close to the start point, based on a simple inference, might not be computationally optimal since the corresponding successors are far from the correct values. On the other hand, updating states in the vicinity of the goal would not help either because their values have converged properly. Thus, some regions between the start and goal points are supposed to have the maximum productivity in terms of the required number of updates for a single solution. This idea is effectively realized using partitioning and then prioritization in the current work. Briefly, instead of solving DP over the entire state space, which is computationally expensive, it is solved within a specified partition and a flow metric is used between partitions to jump to the next partition. This strategy reduces computational effort while maintaining an optimal solution for the optimization problem. We will show how steering performed within a partitioned space can be more efficient than that in a standard non-partitioned version. This computational advantage, which is particularly important in the context of efficient planning in a realistic problem, comes at the cost of some extra memory and overhead to represent the partitioned system. As expected, the proposed method suggests a nonlinear optimal solution in the presence of stochastic deflection that will allow us focus more on the control-related issues. Although at the current stage this approach is a globally off-line solution and can not be directly applied for the real-time purposes, it is considered as an enhanced pre-planner which is employed preoperatively.

This chapter is organized as follows. Section 6.2 briefly reviews the stochastic "bicycle" model used for needle steering. Section 6.3 briefly describes the conventional value iteration solver and its counterpart in partitioned state space. In section 6.4, simulation results are given to compare the efficiency of the new version, and in section 6.5, experimental results are discussed. Finally, section 6.6 presents conclusions and suggestions for future work.

6.2   A Stochastic Framework for Steering Model

The goal of motion planning is to obtain a set of control actions that guides the needle to a predetermined target while avoiding obstacles and satisfying probable user-defined criteria. To explore a model-based control approach, first we need to model tissue-needle interaction. For this purpose, a discrete version of the bicycle-like model initially developed by Webster et al. [5] and widely used in other work (e.g., [10–12]) is proposed. Torsion compensation will be added to this model in section 6.5. Note that choosing a rigid material to represent tissue and ignoring distributed friction may not be realistic [5]; however, it is acceptable for preliminary experiments and to study the effect of needle deflection during steering without the complexities arising from tissue behavior. It is also presumed in this work that the tip position is measured by an imaging modality or an electromagnetic tracker, and the workspace boundaries and the obstacle arrangement are known parameters. Therefore, this path planner is only concerned with steering the needle inside this imaging plane. We believe that this simplified scheme will contribute in better understanding of the modeling and control issues in more generic path-following cases.

It is assumed that the rotation of the needle at the base leads to reorientation of the tip and hence control of the trajectory of the needle. This is the method based on which the needle is manipulated inside the tissue. One DOF actuated at the needle base is a pure insertion of length δ while the second DOF is a pure tip rotation of 180°. Under this condition and regardless of the insertion velocity, the needle moves along an arc of approximately constant radius ρ in the direction of the bevel. A 180° rotation of the needle causes the bevel at the tip to point in the opposite direction of the preceding arc of deflection. Thus, the entire motion of the needle is fully described by the motion of the needle tip and a number of circular segments with the radius ρ. The value of ρ is dependent on the tissue-needle interaction properties, which includes tissue elasticity, needle geometry, friction, and clamping forces during insertion. If one can determine the aforementioned turning points inside the tissue, the planning problem becomes straightforward since the rest of the actions are merely pure insertions. Moreover, it should be noted that the proposed control action that is a bang-bang strategy is applied at discrete time intervals using digital controllers. Therefore, investigating a proper strategy for discretization is studied as a part of the modeling. In this regard, the scheme proposed in [10, 11] is outlined next.

At any points of discretized workspace, a binary control action represented by u_k is applied.

One control action is a pure insertion of length δ and the other one is 180° rotation followed by an insertion of the same length. Tracking circular segments, the needle state at instant k is defined as $S_k = (x_k \ y_k \ \theta_k \ b_k)^T$ where the tip position $t_k = (x_k \ y_k)^T$ and the tip orientation angle θ_k are rounded values to the nearest points on corresponding projection planes. In this representation, we overlay a control circle with radius ρ on a Δ-grid plane consisting of horizontal and vertical Δ spacing. Each control circle is also divided into N_r discrete arcs of the same length of δ where,

$$\delta = \frac{2\pi\rho}{N_r} = \rho\alpha$$

Δ and α are spatial and angular resolutions, respectively. $\Delta \times \left[\frac{\delta}{\Delta}\right]$ is the insertion length projected on horizontal or vertical axes in each step. At each position on the Δ-grid network, the needle may be in any of the N_r orientation states and in any of the two clockwise or counter-clockwise directions. Each direction corresponds to two control circles that are tangent to each other at t_k. The bevel direction or b_k is a binary variable which keeps the history of the previous arc and switches at turning points. The tip angle or θ_k is the tangent angle of the current control circle. From an initial value, the tip angle increments or decrements by α depending on the instantaneous control action and the current circular segment. Fig. 6.1 demonstrates the projected needle motion on the imaging plane through segmented arcs. Consequently, this selection results in a model with n discrete states as given by,

$$n = \frac{4\pi\rho x_{max} y_{max}}{\Delta^2 \delta}$$

where x_{max} and y_{max} are the depth and the height of the imaging plane. Accordingly, a better resolution implies a larger discrete model which results in more computational burden demanded by the motion planner.

As mentioned earlier, the tip curvature may be deflected from its intended path as a result of unpredictable tissue-needle interaction, local tissue displacements, system noise or any other unknown artifacts. To incorporate any motion artifacts stemming from this complex behavior, θ_k and the value of ρ have to be updated during the operation. Since the value of ρ seems to be more deterministic in this case, it is set to a fixed value. It is worth noting that in some cases, applying a constant ρ for the entire operation may not be feasible unless tissue properties and needle geometry remain consistent. Also, more deviation may be introduced when a rotation is accompanied by an insertion rather than just a pure insertion.
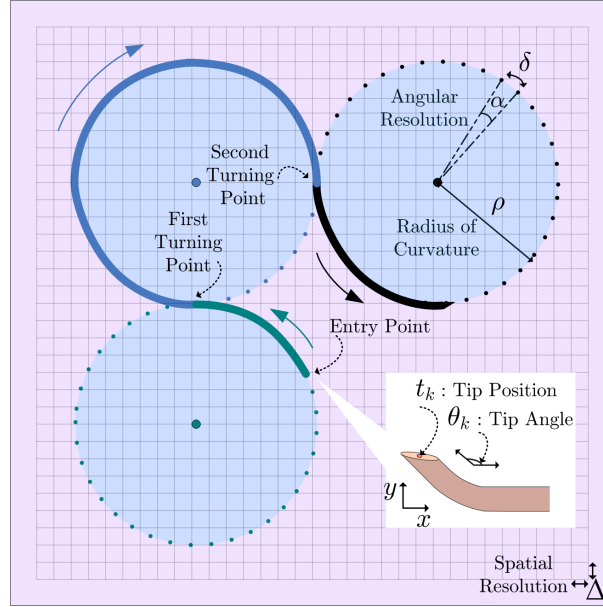
Figure 6.1: Circular segments projected on the Δ-grid network.

Incorporating all these complex uncertainties has been ignored in the current work.

Finally, deflection from circular segments was modeled using a discrete Gaussian distribution as defined in (6.1). In this definition, β_i $(1 \leq i \leq 3)$ specifies statistical properties of the tip deviation, and at the end of each iteration, correction is made by simply adding $\tilde{\beta}_k$ to θ_k. Here, $\tilde{\beta}_k = 0$ corresponds to the deterministic motion with no deviation.

$$P\{\tilde{\beta}_k = m\alpha\} = \begin{cases} \beta_1 & if \quad m = 0 \\ \beta_2 & if \quad m = \pm 1 \\ \beta_3 = \frac{1}{2}(1 - \beta_1 - 2\beta_2) & if \quad m = \pm 2 \end{cases} \qquad (6.1)$$

6.3 Dynamic Programming and A Partitioning-based Solution

As shown by Alterovitz et al. [10, 11], MDP and DP can be employed to yield an optimal path planner for the needle steering problem. Since the current study applies a partitioned version of this algorithm, a brief introduction to generic MDP and DP is in order [17].

MDP is a four-tuple (S, U, T, C), where S is the set of states that describes the system at a

given time. We consider the system over a sequence of discrete time instants when only one event is allowed to take effect. At any stage k, each state has an associated set of applicable actions U_k, and the effect of applying any action is to make the system change from the current state to the next state at stage $k + 1$. The Markov property requires that the effects of an action taken at one state depend only on that state and not on the prior history. The transition function for each action, $T : S \times U \times \acute{S} \to [0\ 1]$, specifies the probability of changing to state $\acute{s}$ after applying u in state s, and $C : S \times U \times \acute{S} \to R$ determines the immediate transition cost. Given an MDP, we define a policy or $\pi : S \to U$ as a mapping from states to actions. An optimal policy determines how actions at different states are chosen in order to minimize the expected cost. Value function or V, $V : S \to R$, gives the minimum value of the total expected cost from being in a state s as,

$$V_\pi(s) = E\left[\sum_{k=0}^{\infty} \gamma^k C(s^k, u_k, s^{k+1})|s_0 = s\right] \tag{6.2}$$

where E is the expected value operator and $\gamma \in [0\ 1]$ is a forgetting factor. $\pi \in U = \{u_0, u_1, ...\}$ is the set of applied control actions. For infinite-horizon problems, the cost is accumulated over an infinitely long path.

An MDP with known probability transition and cost function matrices can be solved optimally using DP. Starting from any estimate, value iteration as a numerical solver sweeps through the state set of the MDP according to (6.3) and updates the value functions iteratively. The Bellman Optimality Equation also gives the expected value of a policy through (6.4).

$$V_k(s) = min_u \sum_{\acute{s}} [C(s, u, \acute{s})T(s, u, \acute{s}) + \gamma T(s, u, \acute{s})V_{k-1}(\acute{s})] \tag{6.3}$$

$$V^*(s) = min_{u \in U(s)} \sum_{\acute{s} \in S} [C(s, u, \acute{s})T(s, u, \acute{s}) + \gamma T(s, u, \acute{s})V^*(\acute{s})] \tag{6.4}$$

where,

$$V^*(s) = min_\pi V_\pi(s) \tag{6.5}$$

The Bellman residual of a state s is defined to be the difference between the value functions in two consecutive iterations. When the maximum residual of the states is less than a

threshold λ, it is concluded that the algorithm has converged sufficiently. Thereafter, an optimal policy is given by,

$$\pi^*(s) = arg\ min_u \sum_{\acute{s}} [C(s,u,\acute{s})T(s,u,\acute{s}) + \gamma T(s,u,\acute{s})V^*(\acute{s})] \tag{6.6}$$

In the case of a flat MDP, with n states and a maximum of m admissible actions for any state, the standard value iteration requires at most $O(mn)$ and $O(mn^2)$ operations in deterministic and stochastic cases, respectively. In light of this fact, the convergence rate becomes very low when high spatial or angular resolution and as a result a large number of states is required. The main drawback of the generic value iteration is that at each iteration, the value function of every state is updated, even if such an update does not or cannot contribute to the convergence. Roughly speaking, the value of the state s depends on the values of its successor states, and if the values of the successor states are incorrect, updating $V^*(s)$ will not move the value function any closer to $V_\pi(s)$. On the other hand, a DP-based method can take into account the realistic assumption of uncertainty in the execution of actions, i.e., stochastic transitions. In this case, the uncertainties account for the biological variations and unpredictable tissue-needle interaction, though biophysical experiments are required to estimate the transition matrix. Furthermore, this approach allows straightforward inclusion of various cost factors other than pure traveled distance such as the number of turns for the entire space. Thus, the resulting policy is globally optimal and fairly realistic.

Several approaches have been proposed for solving large MDPs, and thus for proper allocation of CPU resources. Hierarchical dynamic programming and optimally clustering the entire space using geometric graphs and topological maps is remedy to increase efficiency [18]. Based on this algorithm, the best backup sequence of state space is extracted using graphical features of the MDPs. The use of subtasks to compress the scales of the state space and to identify maximally productive regions is another way proposed by Wingate and Seppi [19]. They upgraded their initial work by proposing a prioritized version of the partitioned model to yield an efficient computation [20, 21] and avoid redundant updates in a deterministic mode. The current study takes advantage of this method so as to circumvent the computational problem in high resolution environments, and to find a fast solver for stochastic needle steering.

To this end, instead of basic sweeping over the entire states and updating value functions,

Table 6.1: Basic Definitions and Notations

state dependents of a state ($\forall s \in S$): $SDS(s) = \{\acute{s} \mid \exists_{u \in U} : T(\acute{s}, u, s) \neq 0\}$
state dependents of a partition ($\forall p \in P$): $SDP(p) = \bigcup_{s \in p} SDS(s)$
partition dependents of a state ($\forall s \in S$): $PDS(s) = \{\acute{p} \mid \exists_{u \in U} \exists_{\acute{s} \in \acute{p}} : T(\acute{s}, u, s) \neq 0\}$
partition dependents of a partition ($\forall p \in P$): $PDP(p) = \{\acute{p} \mid \exists_{u \in U} \exists_{s \in \acute{p}} \exists_{\acute{s} \in p} : T(\acute{s}, u, s) \neq 0\}$

a new approach is used. The idea is to correct the estimated value functions for the current state s, and then for all other states depending on s. Similar to the traditional version, the Bellman error can characterize the usefulness of any given update, while metrics constructed based on the Bellman error are employed as priority measures in a priority queue. In this way, the computation is more focused in the regions with maximum productivity. Assuming that P denotes a set of partitions, which tessellates S, the partition-based method can be described using the definitions and notations as listed in Table 6.1 [21]. Each partition or p may be a single state or a set of states including the entire space as the extreme cases.

The Potential Information Flow (PIF) is a numerical metric which determines the amount of information that could flow when an update is executed.

$$B_k(s) = max_u \sum_{\acute{s}} [C(s, u, \acute{s})T(s, u, \acute{s}) + \gamma T(s, u, \acute{s})V_k(\acute{s})] - V_k(s) \qquad (6.7)$$

This selection is equivalent to the first metric $H1_k(s)$ introduced in [20], and represents the potential change that an update could lead to. Note that this prediction is not the same as the actual difference between the value functions of two consecutive samples. For problems with a limited amount of time to be solved, setting PIF as $H1_k(s)$ is a good choice that changes the value function estimation by the largest possible amount toward its optimal value. Another selection as the second prioritization metric or $H2_k(s)$ is defined as,

$$H2_k(s) = \begin{cases} B_k(s) + V_k(s) & if \quad V_k(s) > 0 \\ 0 & if \quad V_k(s) \leq 0 \end{cases} \qquad (6.8)$$

Compared with $H1_k(s)$, $H2_k(s)$ exhibits a different behavior and outperforms in some

examples. Using $H1_k$ or $H2_k$ as H_k, priority between two partitions and priority of a single partition are respectively defined as follows where the partition with the highest priority is chosen from the queue at the end of each iteration.

$$HPP_k(p, \acute{p}) = max_{s \in \{p \cap SDP(\acute{p})\}} H_k(s) \tag{6.9}$$

$$HP_k(p) = max_{\acute{p}} HPP_t(p, \acute{p}) \tag{6.10}$$

The question as to which metric should be employed naturally arises, but it is not straight-forward to find topological features which accurately mimic the performance of each metric. Therefore, the efficiency of both metrics will be investigated in section 6.4. Note that this method relies on the assumption that the MDP describing system's transition is positively bounded, i.e., $C(s, u) = \sum_{\acute{s}} C(s, u, \acute{s}) T(s, u, \acute{s}) > 0$. For this to be realized, scaling of the cost function, which does not change the optimal solution, is a good option to be performed. Finally, the pseudocode of Prioritized-Partitioned Value Iteration (PPVI) is as follows.

Initialization:

(1) $k = 0$

(2) $\forall s \in S$:

- $V_0(s) = 0$
- $H_0(s) = min_{u \in U(s)} \sum_{\acute{s} \in S} C(s, u, \acute{s}) T(s, u, \acute{s})$

(3) $\forall p \in P, \forall \acute{p} \in P \ (\acute{p} \neq p)$:

- $HP_0(p) = max_{s \in p} H_0(s)$
- $HPP_0(p, \acute{p}) = 0$

(4) $p_0 = arg \ min_{\acute{p}} HP_0(\acute{p})$.

Main loop of PPVI:

(1) Solve regular value iteration and update value functions over p_k until convergence.

(2) $\forall \acute{p} \in PDP(p_k)$, update partition priorities for all dependant partitions as below.

- $h_k = 0$

- $\forall \acute{s} \in \{SDP(p_k) \bigcap \acute{p}\}$:

    – Update $H_k(\acute{s})$ using the flow metric.

    – $h_k = max(h_k, H_k(\acute{s}))$

- $HPP_k(\acute{p}, p_k) = h_k$

- $HP_k(\acute{p}) = max_{\alpha \in P} HPP_k(\acute{p}, \alpha)$

(3) Select next partition with the highest priority as $p_k = arg\ max_{\alpha \in P} HP_k(\alpha)$.

(4) $k \leftarrow k + 1$

(5) Repeat the main loop until one of stopping criteria becomes satisfied, i.e., $\|B_k(s)\|_\infty < (1 - \gamma)\lambda$.

Inside each main loop of PPVI, there is another iterative loop of a regular value iterator, which is realized by (6.4) to (6.6). This loop solves the Bellman equation on a single partition rather than the entire space that is computationally less expensive. Once $e_{k,p} = max(\triangle V_{k,p}) - min(\triangle V_{k,p})$ drops below λ, the convergence of the inner loop is satisfied. $V_{k,p}$ is defined as the value function over members of p_k. Thereafter, the flow metric and the priorities of local partitions are updated and the algorithm transitions to the next candidate partition selected from the local queue.

Note that the first step of implementation, is partitioning. In the current study, it was performed by overlaying a regular grid on the described $\triangle$-grid network so all subsets introduced in Table 6.1 were computed and saved in the memory prior to simulation. Using this scheme, it is easy to evaluate the impact of partition size on the planner's performance.

6.4 Implementation Details and Simulation Results

In the experiments, the workspace is defined as a 2D rectangle with dimensions $x_{max} = 12$ and $y_{max} = 8$. Obstacles are represented by nonconvex polygons, and the target region is defined by a circle with radius 0.2 located at point $t_{goal} = (10\ 5)^T$. All dimensions are in

centimeter. We assume that $\rho = 4$, $\Delta = 0.1$, and $N_r = 60$ leading to $n = 1,176,120$ as the number of discrete states. For simplicity as addressed earlier, grids of $n_x \times n_y$ represent partitions in the implementation where n_x and n_y are the number of equally spaced lines along x and y axes, respectively. By some trial and error, we set $\gamma = 0.95$ and $\lambda = 0.01$. Noise parameters are selected as depicted in Fig. 6.2. Thus, $\beta_1 = 0.466$, $\beta_2 = 0.24$, and $\beta_3 = 0.027$ resulting in $\mu_{\tilde{\beta}\backslash\alpha} = 0$ and $\sigma_{\tilde{\beta}\backslash\alpha} = 0.85$.

In this problem, failure is defined as colliding with an obstacle, exiting the feasible workspace, or reaching a state in which one of the two former incidents is negligible at the next state. Target states transition to themselves with probability 1 and zero cost regardless of u_k. Obstacle states transition to a termination state with probability 1 since the needle can not go further. Transition probabilities for the rest of the states are determined by non-linear kinematics of needle motion discussed in section 6.2. The control action has a binary behavior. Thus, two matrices of $T(s, -1, \acute{s})$ and $T(s, +1, \acute{s})$ appear in the solver, each of which contains n^2 entries in general. Since each successor state or $\acute{s}$ lies within a spatial distance of δ from s, each row of transition matrices has only $\acute{n}$ non-zero elements where $\acute{n} \ll n$. In the current study, in view of (6.2), $\acute{n} = 5$. Therefore, to save time and memory, each $T_{n \times n}$ sparse transition matrix is reshaped into an $n \times 5$ matrix whose row elements refer to the index of successive states. For this to work, a coding procedure was employed to encode each four-tuple $(x_k \; y_k \; \theta_k \; b_k)^T$ to an indexing integer ranging from 1 to n, and vice versa to decode the index. Note that all references to a state are done through its index.

The next step determines the cost function. Thus, p_k is compared to the boundaries of the target, obstacles, and imaging plane to detect each of corresponding incidents. As mentioned earlier, if s is a target state, then the successor state $\acute{s}$ must be a target state with 0 associated cost. Considering the fact that an insertion results in some trauma to living tissue, C_i is applied for every unit length of the inserted needle. A similar damage but with more intensity occurs when the needle is rotated so C_r is incurred after each rotation while $C_r > C_i$. Prohibitive costs of C_o and C_w are also added when the tip collides with an obstacle or exits the specified workspace. A summation of all these individual costs gives the associated cost matrices or $C(s, \pm 1, \acute{s})$. Initially, it is assumed that $C_i = 10$, $C_r = 40$, $C_0 = 200$, and $C_w = 100$. Due to the large size of matrices, another important factor reducing the computational load is a proper definition of the variable types. $T(s, \pm 1, \acute{s})$ are defined as 'int32' or 'int16' depending on the partition size. $C(s, \pm 1, \acute{s})$ are also set to be 'int16' while the rest of the variables are declared as 'single'. By default, we use $H1_k$.
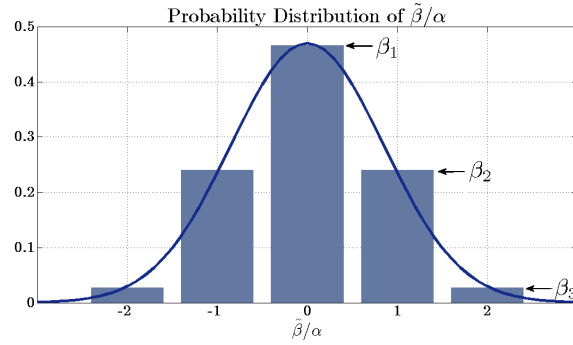
Figure 6.2: Deviation of the tip orientation from the "bicycle" model.

According to these assumptions, the T and C matrices and then all the values of $SDS()$, $SDP()$, $PDS()$, $PDP()$ mappings are obtained in advance. The planner was evaluated using MATLAB® on a desktop computer with 512MB RAM and a single core 2.4GHz Pentium IV 32 Bit processor.

As the first test, a grid of 12×8 is employed to construct partitions. Fig. 6.3 demonstrates the order at which partitions were processed, and also dependencies of a sample partition. Inside each square, the number on the right hand side represents partition number while the number located on the left stands for the order of process. The latter number is set when a partition is processed for the iteration for the first time. In this graph, the red square depicts partition number 26 whereas its surrounding cyan area stands for $sdp(26)$. At one glance, five partitions seem to be unprocessed. It is a boon to the solver to ignore a portion of the workspace which has no beneficial information. Logically, there is no possibility for the needle to penetrate an obstacle thus it is wise not to include these regions in the optimization. This idea is automatically realized by PPVI by focusing on only informative regions.

Starting from the initial point selected as $t_0 = (0 \ 2)^T$ and $\theta_0 = -30°$, PPVI steers the needle toward the goal after 26 steps, which is shown in Fig. 6.4. Compared to the deterministic case as expected from [10], uncertain planning with the described parameters leads to a greater clearance from the obstacles with the larger number of turnings. For deterministic motion, β_1 is set to one and the rest of the noise coefficients are set to zero. By changing C_r from 40 to 100, more emphasis is put on the maximum number of needle turns. The results are shown in Fig. 6.5. Turn points are represented by green circles. Although the path shown in Fig. 6.5(a) does not maintain a good clearance from the closest obstacle to the entry point, the turning number reduces from 11 to 9 compared to Fig. 6.5(b). By
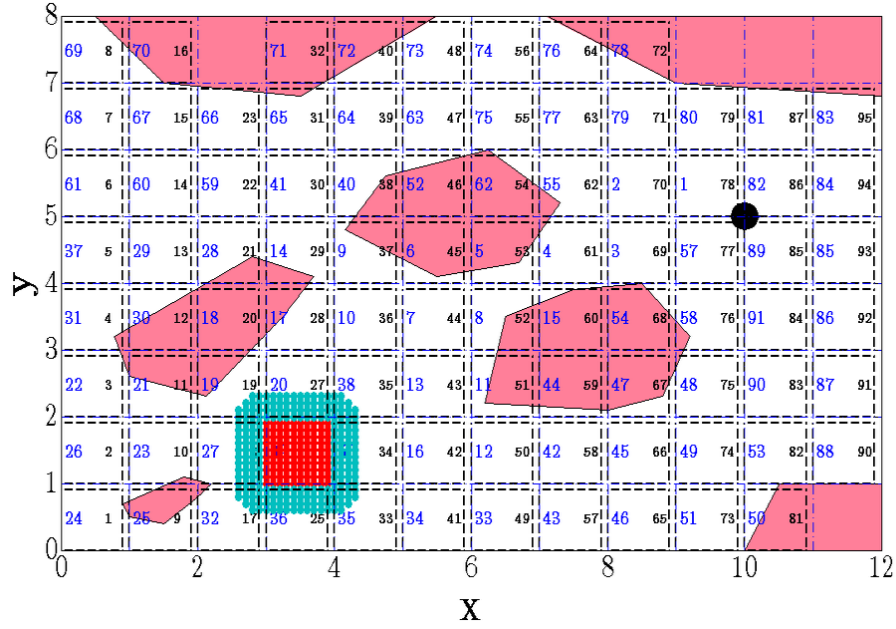
Figure 6.3: Sequence of computations when $(n_x, n_y) = (12, 8)$ plus dependencies of partition number 26.

(a)   (b)

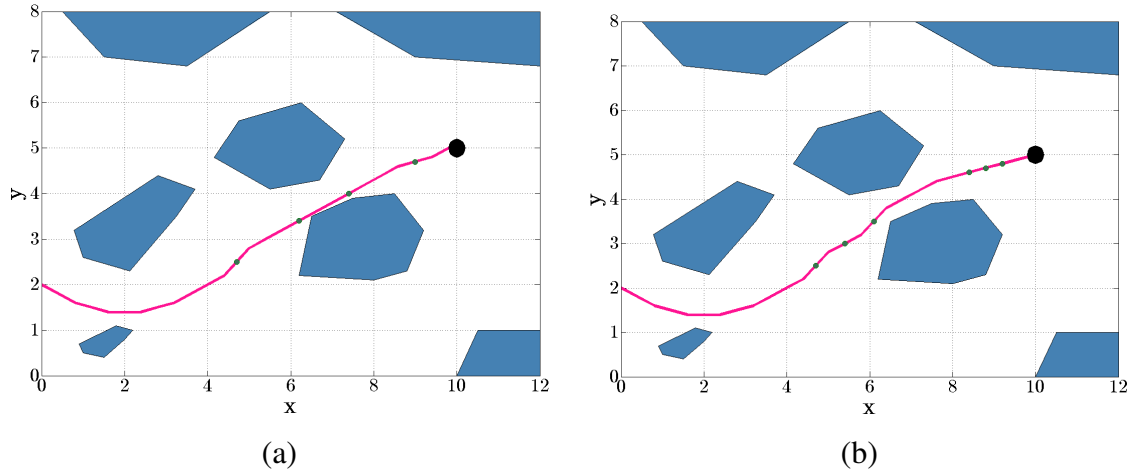Figure 6.4: Motion plan comparison (a) deterministic steering with 4 turns (b) stochastic steering with 6 turns.

setting C_i to 1 instead of 10, the results shown in Fig. 6.5(c) are obtained where the needle steers along a longer path and turns around the obstacles. In this test, the initial deflection was set to zero.

The main evaluation of PPVI is performed by measuring the amount of time needed to find
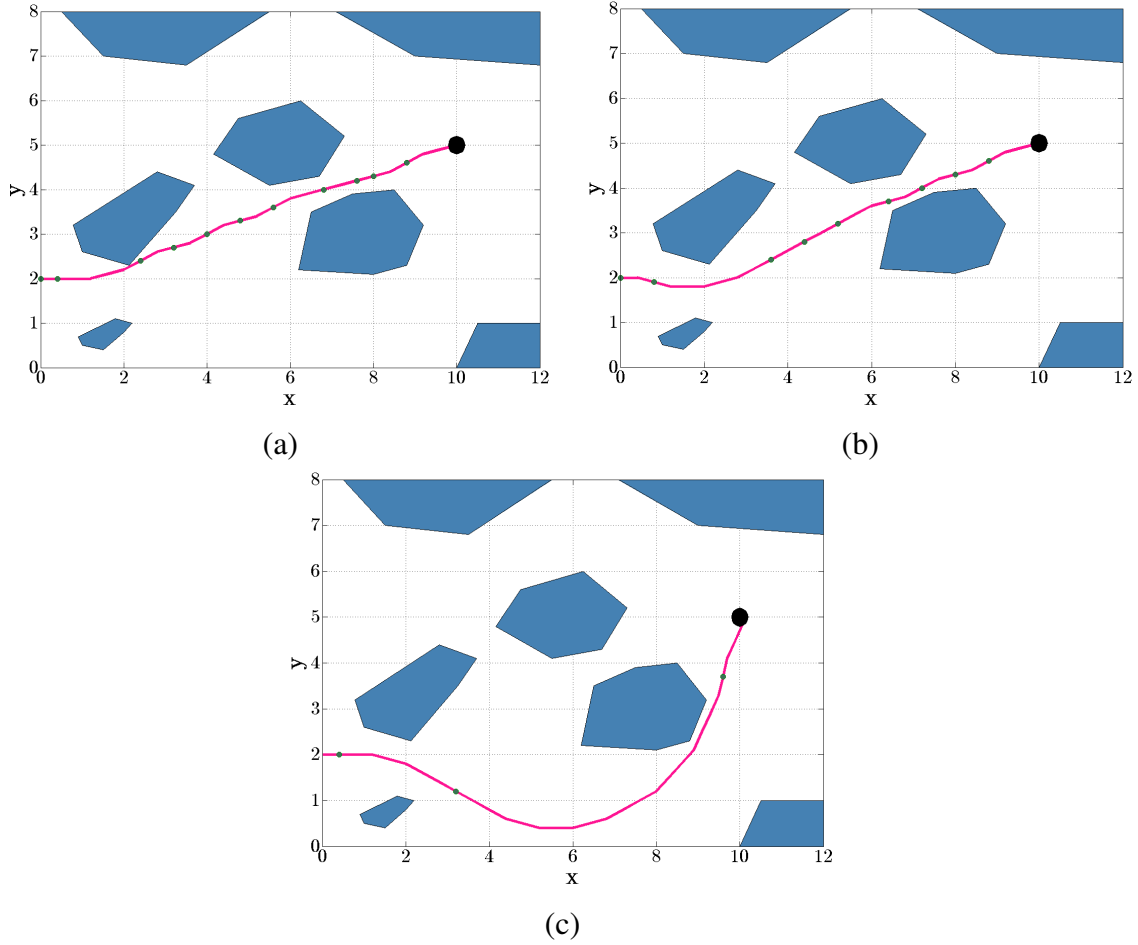
Figure 6.5: Motion plan comparison in the stochastic case (a) $C_i = 10$ and $C_r = 40$ with 11 turns (b) $C_i = 10$ and $C_r = 100$ with 9 turns (c) $C_i = 1$ and $C_r = 100$ with 3 turns.

the optimal policy. Compared to the generic value iteration, PPVI exhibits a similar performance from the point of the resultant policy, but there is a considerable difference in terms of timing. Using smaller partitions, it is possible to exclude a portion of centrally located obstacles from the planner's effective workspace unlike the case in Fig. 6.3. Generally, PPVI saves more time by this selection as a result of dealing with a smaller workspace; however, the trend demonstrating the behavior of PPVI performance with respect to either the number or the size of the partitions or the selected flow metric is too complex to be captured [21]. The numerical results for six studied cases and the sequence of process for $(n_x, n_y) = (24, 16)$ are respectively given in Table 6.2, Table 6.3 and Fig. 6.6. The numbers in Fig. 6.6 have the same meaning as in Fig. 6.3.

Roughly speaking, the computational burden for PPVI is $O(mk_1 p(\frac{n}{p})^2) + O(k_2 p)$. The first
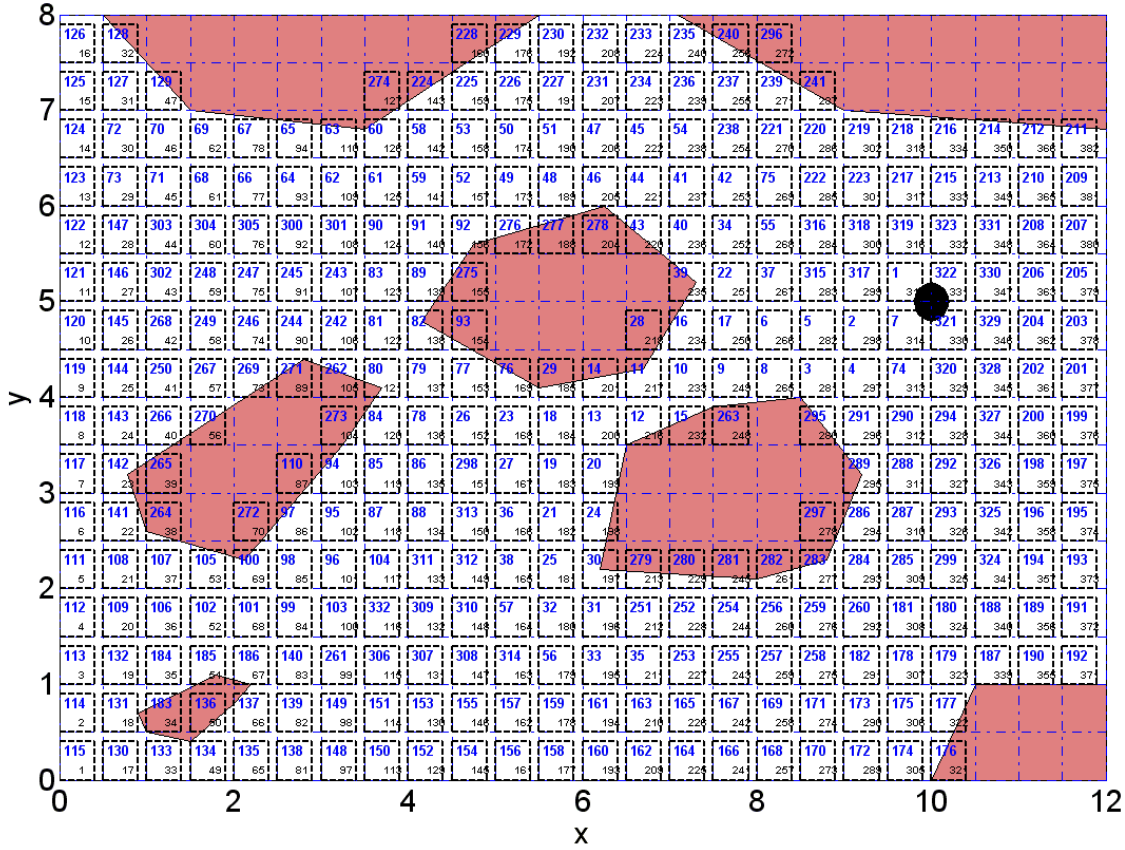
Figure 6.6: Sequence of computations when $(n_x, n_y) = (24, 16)$.

Table 6.2: Numerical Results: Timings

partition size	flow metric	t_s (sec)	t_c (sec)	total time (sec)
$(n_x, n_y) = (6, 4)$	$H1$	2443.2	269.4	2712.6
$(n_x, n_y) = (6, 4)$	$H2$	2317.0	259.9	2576.9
$(n_x, n_y) = (12, 8)$	$H1$	1115.1	690.5	1850.6
$(n_x, n_y) = (12, 8)$	$H2$	812.2	552.3	1363.5
$(n_x, n_y) = (24, 16)$	$H1$	700.8	1612.1	2312.9
$(n_x, n_y) = (24, 16)$	$H2$	522.4	1663.8	2186.2

term shows the total complexity required for the individual partitions to be solved and the second term indicates the complexity of cross transitions. In Table 6.2, the notations t_s and t_c stand for the total time spent on solving the partitions and updating the transition priorities, respectively. As per section 6.3, $m = 2$. Moreover, k_1 and k_2 are two other parameters whose values are determined by the number that a partition is referred to for being iterated and for the flow metric being updated, respectively.

Table 6.3: Numerical Results: Partitions and States

partition size	number of partitions	number of processed partitions	number of processed states
$(n_x, n_y) = (6, 4)$	24	24	1152000
$(n_x, n_y) = (12, 8)$	96	91	1092000
$(n_x, n_y) = (24, 16)$	384	332	996000

In contrast with PPVI, the generic value iteration as implemented in [11] took around 8 hours and 4 minutes to converge after 196 full or 230,519,520 single updates. Accordingly, the update rate becomes roughly 7928.5 updates per second in the planner PC. A relatively high number of partitions, as shown by the last two rows of Table 6.2, leads to an absolute drop in the effective update rate. This fact is justified as a result of the increased number of travels between the partitions that occupies more system overhead although leading to a smaller number of effective or processed states as listed in Table 6.3. According to the results, changing the flow metric will change the sequence of information propagation and also timing with no discernible effect on the optimal policy. In this problem, $H2$ slightly outperforms $H1$. Another factor affecting the timing performance is the partition size. In this respect, there is no solid theory to benefit from. Each partition contains $n_s = \frac{n}{n_x \times n_y}$ members. In the beginning, we do not know how to predict the optimal value of n_s, except to observe the outcome using a range of values for n_x and n_y. We examined three sets as listed in Table 6.2, and consequently the second selection for (n_x, n_y) accompanied by $H2$ tends to yield the best timing results.

Note that the absolute timings, listed in Table 6.2, depend very much on the technique by which the algorithm is implemented. Developing a fast method to access the planner's data base, memory management and designing an efficient way to check a collision are amongst the programming skills that enable us to accelerate PPVI more. Furthermore, building the entire planner in C++ as in [11] results in an inherently better performance. Although in the current study PPVI was implemented using MATLAB® built-in functions, it is expected to outperform the generic value iteration using any other programming language.

6.5   Experimental Test

An experimental implementation of the proposed methodology was carried out on the state-of-the-art robotic system [22] described in Appendix A. Positional data from the tracker are acquired at the rate of 40Hz, and the pivoting algorithm resulted in 10.87mm as the

average distance between the tip and the coil center after 5 trials [23]. It is worth noting that this system is capable of implementing more advanced steering approaches; however, it is employed here to validate the performance of PPVI.

In this test-bed, the cannula of the 18GA stainless steel needle (Cook Medical) has a bevel angle of 22º with outer and inner diameters of 1.270mm and 0.838mm, respectively. Experiments were carried out on a Gelrite Gellan Gum (Sigma-Aldrich) with a uniform weight concentration rate of 5% in water. This simple and stiff environment allows us to study the impacts of needle bending without the complications of tissue deformation. The insertion and the rotation trajectories were LSPB with maximum velocities of 12mm/sec and 3rpm, respectively. A twisting torque was used to compensate for torsional lag as proposed in [16]; otherwise, after a few turns, poor performance was observed as a result of the bevel flip when switching to an opposite control circle. In the experiments, the torsional lag never exceeded 4.22º.

Note that PPVI is a model-based approach that entails the radius of curvature to be properly approximated. Thus, 5 pure insertions were carried out in advance, and the deflection information with respect to the insertion depth was logged. A least-squares method was then applied to fit a circle to the curve that led to 646.83mm as the average value of ρ_{actual}. A grid with $(n_x, n_y) = (32, 6)$ accompanied by $H2$ was employed to construct PPVI, and N_r and (Δ_x, Δ_y) were set to 1800 and $(3, 0.15)$, respectively. The initial cost function as well as the statistical deviation model proposed in section 6.4 were also applied to the planner.

Starting from the initial point selected as $t_0 = (0\ 1)^T$ and $\theta_0 = -5\alpha$, PPVI introduces a turning point located at $x = 9$mm and $y = 0.75$mm. Due to a relatively big radius of curvature ($\rho_{actual} \gg \rho$), the workspace needed to be redesigned in order to accommodate the slight bending. A practical workspace and the solution proposed by PPVI for the first experiment are shown in Fig. 6.7. According to the results, the maximum deviation from the intended path in practice is 0.176mm and occurs at the target location. The turn points are represented by blue circles along the calculated path.

In the next test, the initial point was set to $t_0 = (0\ 1.5)^T$ with no change in the orientation angle. As shown in Fig. 6.8(a), in the first run the proposed path is similar to the solution obtained in the first experiment. Then, C_r was set to 40 instead of 100, and the desired path was recalculated. Three more turns as well as a shorter path were introduced by the planner
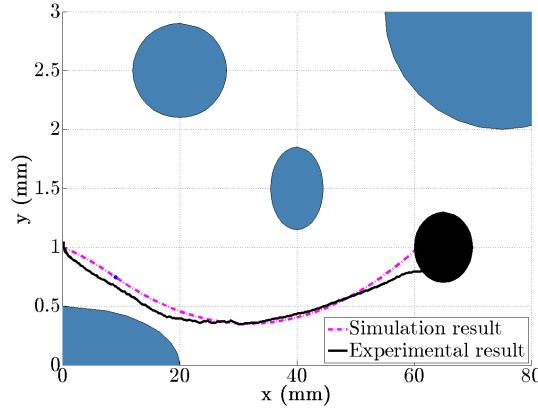
Figure 6.7: Comparison of simulation and experimental results in experiment 1.

as shown in Fig. 6.8(b). In the next run, θ_0 was set to 5α, and as is clear in Fig. 6.8(c), the planner was unable to guide the needle to the exact target location. In this case, the tip position lies within 0.248mm of the target's edge. Therefore, an error bound shown by a dotted circle is defined to depict the targeting error.

In reality, as is apparent in the plots, the needle curvature is not in full agreement with the "bicycle" model. This model is not a perfect model; however, PPVI is robust enough to guide the needle to the vicinity of the target. Although the concentration rate of the gelatin in the experiments was chosen to be high, it did not result in an absolutely rigid tissue and therefore could not enforce the needle body to follow the exact expected curvature. This discrepancy may lead to collisions in a denser environment as simulated in section 6.4. The results presented in this section serve to validate those obtained in the previous section for needle steering in surgical procedures.

For the next experiment, the initial point was set as $t_0 = (0\ 1.8)^T$ with the same upward initial orientation angle used in the last run. It was observed that there existed no paths leading to the target area or even to the vicinity of it as opposed to the previous experiment. In this case, a collision with the closest obstacle to the entry point is unavoidable, and it is due to the constraint applied by the curvature. In an extreme case, one can assume a very big value of ρ_{actual} representing the lack of steerability and a dense environment used as the obstacle/target configuration. Using a planner based on the "bicycle" model and regardless of the manipulation mechanism, a collision is likely to occur, and the probability of success is next to zero. In order to find a collision-free path, the value of θ_0 was gradually decreased. It was observed that by setting $\theta_0 = 3\alpha$, the needle hit the target after 2 turns as shown in
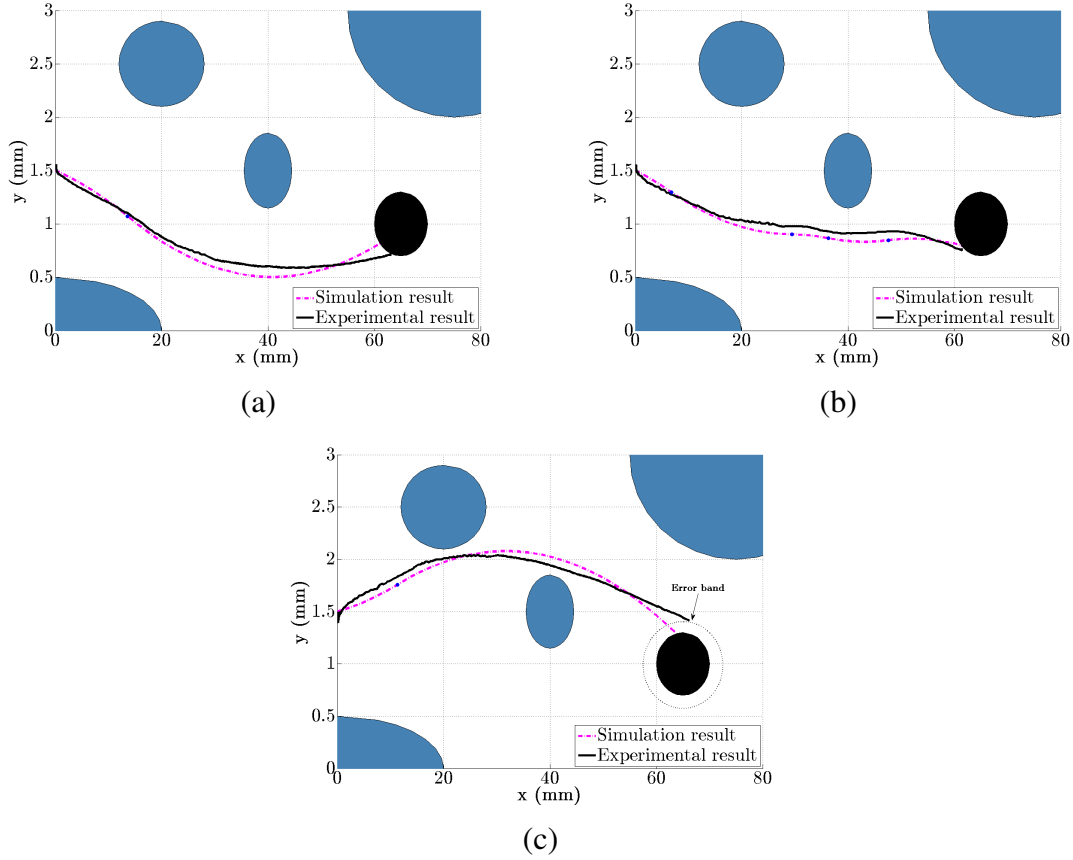
Figure 6.8: Comparison of simulation and experimental results in experiment 2 (a) $\theta_0 = -5\alpha$ and $C_r = 100$ with 1 turn (b) $\theta_0 = -5\alpha$ and $C_r = 40$ with 4 turns (c) $\theta_0 = 5\alpha$ and $C_r = 100$ with 1 turn.

Fig. 6.9(a). It is also possible to find the globally optimal path with respect to the initial orientation angle by searching over the entire look-up table provided by PPVI. Following this strategy, the optimal solution for the initial insertion point located at $(0 \ 1.8)^T$ has been demonstrated in Fig. 6.9(b). Accordingly, $\theta_0(optimal) = -16\alpha$.

Future experiments will be conducted on animal tissue phantoms using a 22GA needle whose outer and inner diameters are 0.7176mm and 0.413mm, respectively. Utilizing such a highly flexible needle, which provides more steerability and therefore more compatibility with the "bicycle" model, demands more sophisticated technology. To this end, employing an ultra thin electromagnetic sensor coil whose prototype is intended to come to the market in the near future is under development. In summary, technological limitations impede the arrangement of a complex obstacle/target configuration for experimental tests.
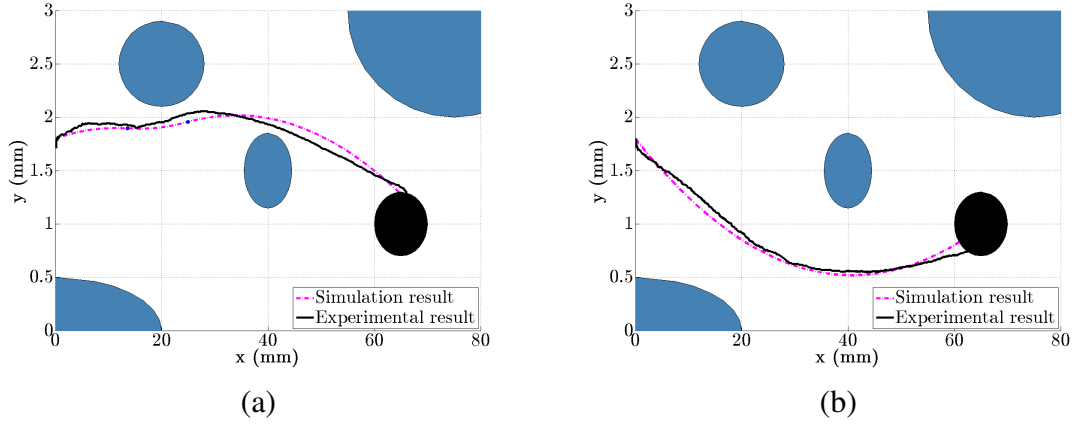
Figure 6.9: Comparison of simulation and experimental results in experiment 3 (a) $\theta_0 = 3\alpha$ with 2 turns (b) $\theta_0(optimal) = -3.2^\text{o}$ with no turning point.

6.6 Conclusions and Future Work

The results presented in this chapter have shown the feasibility and advantages of the prioritized partitioning-based value iteration (PPVI) for needle steering in relatively stiff materials. In this model-based control strategy, the needle is steered on a discretized 2D plane and reaches a target without any collisions with obstacles. This optimal approach showed significant savings in terms of the time required for the convergence of the modified value function in contrast with the non-partitioned value iteration. Compared to the other existing methods, it is worth noting that the presented approach is a globally off-line optimization algorithm which solves the Bellman equation throughout the entire workspace, and creates a look-up table. Once the table is obtained, it can be applied to any initial insertion position or orientation to guide the needle toward the target. In other words, pre-planning is time-consuming, but intraoperative control is instantaneous with no need to do any further processing. This is the key point of this research. On the other hand, one of the limiting factors of almost all DP-based methods applied to large-scale systems is the requirement of a large hardware memory to store the data. By partitioning and solving the Bellman equation as we did in this chapter, it is merely necessary to store information of local states and corresponding dependencies. Therefore, as long as the data describing the partitions and cross transitions can be saved into a computer's RAM, the problem is solvable. Moreover, another advantage of this method is that inaccessible regions of the problem will remain unprocessed, which is another reason for improving computational efficiency. Although

this method still requires more enhancements in terms of the timing in order to make it applicable for a real-time planning, it is a good macro approach for pre-planning tasks. To this end, integrating PPVI with a fast micro solution and testing the entire planner on the brachytheraphy setup is the next step.

For future developments, initial information can help with the curse of dimensionality and better partitioning of the entire space. In this regard, finding an optimal scheme compared to the simple version utilized in this chapter will yield a better solution as a direct result of (1) minimized cross-partition transitions; and (2) reduced overhead. In the absence of *a priori* scheme, on-line partitioning may enhance the work. Note that the performance of PPVI is different from one case to another. In other words, counter-examples may be found to give unfavorable results unless all parameters are set properly which can be a complicated task. Stability analysis, using a hybrid flow metric and employing other solvers in addition to finding a better implementation framework are other aspects that will be investigated in the future. Clearly, more theoretical work is needed to guide the enhancements of PPVI. Apart from DP-related issues, it may be possible to develop an automated method to estimate the needle curvature and the variance properties from medical images and force/torque data for updating the planner's parameters intraoperatively. A simple deflection model, which is based on beam theory and force/torque readings, can be integrated with PPVI to have a better estimate of the needle curvature during the procedure. At the very least, all these efforts will need to be validated through appropriate experiments with animal tissue phantoms rather than uniform artificial phantoms.

Bibliography

[1] S. Susanto, S. Chauhan, "A Hybrid Control Approach for Non-Invasive Medical Robotic Systems," *J. Intell. Robot. Syst.*, vol. 60, no. 1, pp. 83-110, 2010.

[2] N. Abolhassani, R. Patel, and M. Moallem, "Needle Insertion into Soft Tissue: A Survey," *Med. Eng. Phys.*, vol. 29, pp. 413-431, 2007.

[3] C. Casadei, S. Martelli, and P. Fiorini, "A Workcell for the Development of Robot-Assisted Surgical Procedures," *J. Intell. Robot. Syst.*, vol. 28, no. 4, pp. 301Ű324, 2000.

[4] N. Abolhassani, R.V. Patel, and F. Ayazi, "Minimization of Needle Deflection in Robot-Assisted Percutaneous Therapy," *Int. J. Med. Robotics Comput. Assist. Surg.*, vol. 3, pp. 140-148, 2007.

[5] R.J. Webster III, J.S. Kim, N.J. Cowan, G.S. Chirikjian, and A.M. Okamura, "Non-holonomic Modeling of Needle Steering," *Int. J. Rob. Res.*, vol. 25, no. 5/6, pp. 509-525, 2006.

[6] J.T. Hing, A.D. Brooks, and J.P. Desai, "Reality-based Estimation of Needle and Soft Tissue Interaction for Accurate Haptic Feedback in Prostate Brachytherapy Simulation," *Springer Tracts in Advanced Robotics*, vol. 28, pp. 34-48, 2007.

[7] S. Misra, K.T. Ramesh, and A.M. Okamura, "Modeling of Tool-Tissue Interactions for Computer-based Surgical Simulation: A Literature Review," *Presence-Teleop. Virt.*, vol. 17, no. 5, pp. 463-491, 2008.

[8] O. Goksel, E. Dehghan, and S.E. Salcudean, "Modeling and Simulation of Flexible Needles," *Med. Eng. Phys.*, vol. 31, pp. 1069-1078, 2009.

[9] V. Duindam, R. Alterovitz, S. Sastry, K. Goldberg, "Screw-based Motion Planning for Bevel-Tip Flexible Needles in 3D Environments with Obstacles," *In Proc. of IEEE Int. Conf. on Rob. Autom. (ICRA)*, 2008, pp. 2483-2488.

[10] R. Alterovitz, A. Lim, K. Goldberg, G.S. Chirikjian, and A.M. Okamura, "Steering Flexible Needles under Markov Motion Uncertainty," *In Proc. of IEEE/RSJ Int. Conf. on Intel. Rob. Sys. (IROS)*, 2005, pp. 120-125.

[11] R. Alterovitz, M. Branicky, and K. Goldberg, "Motion Planning under Uncertainty for Image-Guided Medical Needle Steering," *Int. J. Rob. Res.*, vol. 27, no. 11-12, pp. 1361-1374, 2008.

[12] K.B. Reed, V. Kallem, R. Alterovitz, K. Goldberg, A.M. Okamura, and N.J. Cowan, "Integrated Planning and Image-Guided Control for Planar Needle Steering," *In Proc. of 2nd Biennial IEEE/RAS-EMBS Int. Conf. on Biomedical Robotics and Biomechatronics*, 2008, pp. 819-824.

[13] E. Dehghan, S.E. Salcudean, "Needle Insertion Parameter Optimization for Brachytherapy," *IEEE Trans. Rob.*, vol. 25, no. 2, pp. 303-315, 2009.

[14] S. DiMaio, S.E. Salcudean, "Needle Steering and Motion Planning in Soft Tissues," *IEEE Trans. Biomed. Eng.*, vol. 52, no. 6, pp. 965-974, 2005.

[15] D. Glozman, M. Shoham, "Image-Guided Robotic Flexible Needle Steering," *IEEE Trans. Rob.*, vol. 23, no. 3, pp. 459-467, 2007.

[16] K.B. Reed, A.M. Okamura, and N.J. Cowan, "Modeling and Control of Needles with Torsional Friction," *IEEE Trans. Biomed. Eng.*, vol. 56, no. 12, pp. 2905-2916, 2009.

[17] D.P. Bertsekas, Dynamic Programming and Stochastic Control, New York: Academic Press, 1976.

[18] Z. Zivkovic, B. Bakker and B. Krose, "Hierarchical Map Building and Planning based on Graph Partitioning," *In Proc. of IEEE Int. Conf. on Rob. Autom. (ICRA)*, 2006, pp. 803-809.

[19] D. Wingate, K.D. Seppi, "Efficient Value Iteration Using Partitioned Models," *In Proc. of Int. Conf. on Machine Learning (ICML)*, 2003, pp. 53-59.

[20] D. Wingate, K.D. Seppi, "P3VI: A Partitioned, Prioritized, Parallel Value Iterator," *In Proc. of Int. Conf. on Machine Learning (ICML)*, 2004, pp. 863-870.

[21] D. Wingate, K.D. Seppi, "Prioritization Methods for Accelerating MDP Solvers," *Journal of Machine Learning Research*, vol. 6, pp. 851-881, 2005.

[22] H.S. Bassan, R.V. Patel, and M. Moallem, "A Novel Manipulator for Percutaneous Needle Insertion: Design and Experimentation," *IEEE/ASME Trans. Mechatron.*, vol. 14, no. 6, pp. 746-761, 2009.

[23] http://www.ndigital.com/medical/aurora.php

Chapter 7

Conclusions and Future Work

This chapter explains the key contributions of the dissertation and presents conclusions and suggestions for future work in the area of needle insertion/steering based on the current research.

7.1   Conclusions

The main contributions described in this thesis are as follows:

1. In Chapter 2, an asynchronous joint-EKF was developed in order to find an explicit mapping between the inserted length of needle and the measured force signals during needle-tissue interaction. The main motivation for seeking such a non-physics-based method was the sheer complexity of the physics behind needle-tissue interaction which prevents its successful implementation in operating conditions with real-time performance. This study presented a method that was particularly important for robotics-assisted needle-based interventions where no image-based technique is available during the procedure. Accordingly, the axial interaction force was described by a category of nonlinear state-space models whose parameters were intraoperatively identified by the use of Kalman filtering. Successful parameter identification from the data stream during a conventional needle insertion is a remarkable advantage of this approach. Thus, as the needle interacts with soft tissue, force-depth profile provides a useful means to characterize needle-tissue interaction. From this

point of view, it is possible to make an atlas for a variety of needle-tissue combi-
nations, and then take advantage of the proposed scheme to have an approximation
of the total translational force. Hence, explicit knowledge of the biomechanics of
needle-tissue interaction is not required in advance to building the model. Another
important achievement is the capability to model the total axial force without splitting
the insertion/retraction forces into the constituent force components including rup-
ture, friction, and cutting forces. We can, therefore, say that the proposed modeling
strategy holds appeal due to its simplicity, feasibility and real-time implementation.

2. As is known, the interaction between the needle and soft tissue involves frictional
effects, and exhibits hysteresis loops to a great extent. In Chapter 3, a sophisticated
technique was introduced in order to identify and model full features of translational
friction including the Stribeck effect during needle insertion. This approach was in-
spired by the famous LuGre point friction model, and its extension to the case of
friction in the presence of a moving contact patch with a time-varying size. Based on
empirical observations, we showed that static friction mappings were unable to cap-
ture the dynamic nature of translational friction in this application. On the other hand,
the developed family of dynamic structures as suggested alternatives were capable of
replicating the dynamic behavior of the distributed friction along the needle shaft
as it is inserted or retracted. In summary, the introduced friction models performed
well in a number of organic and artificial phantoms such as agar, gelatin, and beef
liver, while capturing static and dynamic frictional effects properly. In addition, the
proposed approach facilitated estimating the cutting force in an intraoperative man-
ner by simply deducting the approximated friction and inertial term from the totally
measured interaction force at the needle base. As highlighted in Chapter 3, friction
compensation is believed to be crucial for automating needle steering, and the cur-
rent technique enables us to improve the bending models in which frictional effects
are neglected. A quick review of simplified models and related issues were given in
section 1.4.1. Even for simulation purposes, it is notable that novice clinicians will
likely have to slow down the insertion and rotate the needle handle several times with
variable insertion rates before accomplishing designated actions. Frictional features
depend on the relative velocity between moving contacts so ignoring frictional ef-
fects and hysteresis cycles in the simulator will certainly make the haptic perception
(sense of touch) nonintuitive. On the other hand, to make the friction model com-
prehensive and applicable to various needle-tissue combinations, a velocity observer

was developed in Chapter 4 to take care of soft tissue deformation in the direction of needle insertion. As a result, the combination of the velocity estimator and friction model was able to accommodate soft-tissue motion and compensate for it without excessive computational complexity or cost.

3. Accurate deflection modeling is the first step toward precise model-based control. Thus, developing a deflection model will be part of a journey towards model-based needle steering. In Chapter 5, mechanical properties of the needle structure, elasticity of the elastic medium, friction along the insertion depth as well as insertion velocity were considered and integrated for modeling. Finally, the proposed deflection model consisted of two Euler-Bernoulli beam elements, whereas the geometry of the moving needle led to a set of PDEs for two sub-beams with coupled non-homogeneous moving boundary conditions. Green's functions were employed as a sophisticated tool to find the sought analytical solution. Theoretical results were validated using experimental studies, and the empirical results confirmed that the suggested technique could open up new possibilities for deflection modeling. The proposed method demonstrated acceptable performance, notwithstanding that a gradually increasing error with respect to insertion depth was observed. As another result, it was found that inserting the needle with a higher velocity or in a phantom with a lower stiffness resulted in a smaller radius of curvature, thereby generating greater needle steerability. This observation agreed with the simulation results; however, it contradicted the very basic assumption in the *bicycle* model based on which the needle curvature was expected to be independent of the insertion rate. The model also exhibited robustness in the presence of uncertain tissue elasticity and viscous friction coefficient. In this scheme, the entire model was built and updated based on force information without using any imaging modality.

4. Using the well-known *bicycle* model [1], prioritized partitioning-based value iteration was applied for needle steering in Chapter 6. As a result, inaccessible regions of the workspace representing delicate organs, e.g., nerves, or impenetrable areas such as bones, remained unprocessed which was one reason for improving computational efficiency. According to this model-based control strategy, the needle was steered on a discretized 2D plane and reached the desired target without any collisions with obstacles while minimizing the path length as well as the number of full needle rotations. Clinically speaking, the outcome led to less tissue trauma which was desirable

in practice. This optimal approach showed significant savings in terms of the time required for the convergence of the modified value function in contrast with the conventional value iteration. Although this method still requires further improvement in terms of process time in very large-scale systems as well as inclusion a time-varying curvature in the planner, it can be considered as an efficient macro approach for pre-planning. However, under some conditions and depending on the nature of needle-tissue interaction, this strategy can be employed as part of an intraoperative planner. Promising results on the brachytheraphy setup proved the feasibility and advantages of this planar steering technique. However, prostate brachytheraphy is not the best application to show the capabilities of needle steering in general. Steering techniques turn out to be more helpful in applications such as brain surgery in which finer needles are employed, and therefore more curved trajectories are possible.

7.2 Suggestions for Future Work

There are several directions in which the research described in this thesis can be continued in the future. Some suggestions are given below:

1. The large variations in the acquired interaction forces at different insertion paths specially in biological tissues should be quantitatively analysed. Toward this goal, thorough robustness and statistical analysis using a wider range of needle-tissue combinations on artificial and/or organic phantoms in a more clinical setting are subjects of ongoing research.

2. The performance of the proposed schemes for modeling or control should be fully evaluated using a multi-layer artificial phantom which generates the behavior of realistic organic tissues during interventional procedures. To this end, the phantom can be fabricated such that each layer consists of a thin membrane plus a deformable body. In the case of multi-layer phantoms, the dynamics of tissue puncture may have considerable effect on the entire needle-tissue interaction. In the extended insertion experiments performed, significant differences were observed between artificial phantoms and animal organs in terms of:

   - force-insertion depth or force-velocity dynamics

- maximum force range
- viscosity

Note that elasticity of biological tissues can be easily replicated by mixing appropriate amounts of ingredients. Considering all these empirical observations, exploring a new artificial phantom as a combination of chemicals that produces a more realistic force pattern would be demanding. It will certainly ease and speed up the process of developing and validating new modeling and steering mechanisms. In addition, mimicking inhomogeneity and nonlinear viscoelasticity by artificial tissues is another topic that should be investigated in future research. For the sake of simplicity, the needle structure as an elastic foundation was assumed to be uniformly linear in the modeling discussion in Chapter 5.

3. As is apparent, managing an *ex-vivo* experiment on biological tissue under controlled or repeatable conditions is challenging and requires solving some practical issues such as:

   - storage and contamination
   - precise cutting and fitting the sample into its container
   - tissue immobilization

   That is why artificial phantoms are usually preferred during the first steps in assessing a new approach. As mentioned earlier, an ideal artificial phantom is expected to preserve the typical range of elasticity, viscosity and tissue deformation of living tissue as well as mimick its force-velocity or force-insertion depth dynamics. However, lack of vascular pressure and temperature effects changes interaction dynamics when compared with *in-vivo* tests. Moreover, in the *ex-vivo* experiments on fresh muscle, e.g., chicken breast, beef, and ham, dynamics of the force-velocity loops was found to be different from those of beef liver and artificial phantoms. For example, it was observed in muscle tests that the equivalent Stribeck effect in friction analysis appeared very slowly, and viscous damping turned out to be negative (or zero), which were not justifiable by classic friction theories. This suggests that the mechanics of translational friction in muscle-like materials deserves more theoretical work in the area of materials science, mechanics of contacts, and fluid mechanics. It is likely that we need to investigate the problem at a molecular level in order to identify and then classify the tissue structure of specific organs in order to develop organ-specific models.

4. One practical issue that can arise from needle steering along curved paths is possible tissue damage during needle withdrawal. This is an important aspect of needle steering. As is obvious, interaction forces during insertion and retraction phases differ so there is no guarantee that the needle moves along the same insertion path during withdrawal. Developing a mechanism for safe needle retraction to minimize tissue damage is an open problem, and should be carefully considered.

5. In an extended test as reported in Chapter 4, insertions were performed at multiple heights of an artificial phantom. Prior to this experiment, the tissue sample was placed in its container and clamped such that the bottom and edges of the sample were firmly fixed, leaving the sides free to move and unobstructed for needle insertion. Different magnitudes of tissue deformation and insertion force were observed; so it was concluded that as a result of dissimilar boundary conditions experienced by the needle during each insertion, the measurements were different. In general, organ geometry and boundary conditions imposed by the connective surrounding tissue are the factors that influence the accuracy of surgical intervention. In [2], mathematical clues on modeling boundary constraints and anatomical geometries have been provided, and as a case study, the procedure of needle insertion into the prostate has been studied. Due to the complexity of the trends, investigating the practical issues of incision location and tissue boundary conditions on needle-tissue interaction dynamics is recommended for future work.

6. Static needle deflection solutions have been widely exploited in the literature for the sake of simplicity and ease of implementation [1, 3–7]. The frictional effect are usually neglected [1,3] although translational friction is the most essential force component of needle-tissue interaction. To take one step forward and enhance the current study, it is proposed as future work to integrate the full ODE exhibiting friction characteristics suggested in Chapter 3 with the PDE associated with the dynamic bending introduced in Chapter 5. Later, to simplify the structure and find the closed-form solution, model reduction using approximate ODEs instead of an accurate PDE should be examined. In [8], a model reduction method was investigated in order to reduce the computational effort needed to evaluate PDE-based models. Applying transform methods may ease this procedure [9].

7. Some advanced topics on dynamic modeling of flexible structures may improve the suggested modeling work. In case of considerable needle flexibility, either *Timo-*

shenko's or *Rayleigh's* beam theory can replace the basic *Euler-Bernoulli* beam theory so that the effect of rotary inertia or shear deformation of the needle cross section is fully taken into account [10]. However, solving the resultant equations of motion with moving boundary conditions is still challenging. In another modification, the horizontal component of distributed friction can be introduced in the bending equations. The extra term required to represent this additional effect in the governing PDEs consists of the second derivative of $\omega(x,t)$, i.e., vertical displacement of a beam element, with respect to x, i.e., axial distance of the beam element from the needle's base holder.

8. It is pointed out that existing steering methods usually require predefined parameters prior to insertion. For example, applying a constant curvature value for the bevel-tip needle path as a simple but practical model is mandatory in many steering algorithms [11–21]. In fact, this is not a strong assumption, and can be easily violated for various reasons such as unknown or uncompensated uncertainties or time-varying interaction characteristics. Based on the empirical observations, the actual path of a bevel-tip needle in a homogeneous artificial phantom follows an oval shape rather than a full circular curvature. Under some conditions, the oval curvature can be approximated by a circle that is represented by the *bicycle* model. Once an extended version of the *bicycle* model, which enables us to accommodate uncertainties either implicitly or explicitly, is achieved, various methods are applicable to perform path planning. Controllability and optimal path planning for car-like robots such as *Dubins* car as a specific case of mobile robots, have been discussed in [22,23]. These can be applicable to the needle steering problem. Accordingly, even in the absence of obstacles, planning nonholonomic motions in the presence of uncertainty is not an easy task. There is no general algorithm to plan motions for any nonholonomic system so that the system is guaranteed to exactly reach a given goal. The only existing results are for approximate methods, which guarantee only that the system reaches a neighborhood of the goal, or exact methods for special classes of nonholonomic systems. Soueres and Boissonnat [24] explained the same concepts from a different viewpoint. They solved the shortest path problem for car-like robots using *Pontryagin's Maximum Principle* (PMP) which constituted a generalization of *Lagrange's* problem of the calculus of variation. While this method provided a necessary condition for the solution to be optimal for various kinds of cost functions, *Boltyanskii's* sufficient condition was introduced to maintain the necessary conditions for the trajectories to

be optimal. A geometric approach based on partitioning was then proposed to provide a collision-free admissible path in the configuration space of the mobile robot. Obstacle avoidance usually adds a second level of difficulty to this problem. In [23] some advanced ideas, for example, *virtual adaptive control* or *state feedback control*, have been discussed which are closely related to this case and may be applicable to the needle problem as a nonholonomic or a car-like robot system.

9. Generally speaking, as the needle penetrates tissue, more local information is gathered by the sensory system so the most recent measurements provide a useful guide to re-characterize the interaction if required. Thus, it is recommended to update the existing deflection model, and thereafter the controller, toward achieving a more *robust* and *accurate* solution. This strategy will allow us to predict variations of needle-tissue interaction, and then compensate for them. To this end, implementing a feasible computer-assisted planner that benefits from an *adaptive* control rule and automatically adds a *learning* capability to the system can be considered as the ultimate goal. Following this strategy, physiological variations associated with needle-tissue interaction and varying tissue properties can be sufficiently taken into account with no need to employ a complex FEM-based method which can be computationally expensive. Other geometric or mechanical nonlinearities that are usually ignored or linearized in FEM may also be tracked and accommodated by this strategy.

10. Another approach to deal with needle steering is to directly control the PDEs associated with needle flexion and needle-tissue interaction. In contrast to ODEs, no general methodology exists for PDEs. However, motion planning, trajectory generation, state-feedback and output-feedback design for a class of PDEs as well as *Lyapunov* stability have been discussed in [25]. Backstepping control design and optimal control of a category of nonlinear PDEs have also been offered in the same reference. Note that the shortcoming of these solutions is the fact that these techniques are problem-specific, and are not generalizable to any class of PDEs. Also it is important to note that model reduction plays an important role in most methods for control design for PDEs. A reduced-order model can be written as a set of ODEs for which well-developed control theory is available.

11. The study presented in this thesis is particularly important for robotics-assisted needle-based interventions where no imaging data is available throughout the operation. It holds appeal due to its feasibility, simplicity and real-time implementation. However,

one exciting area for further extension is concerned with integration of image-based techniques with the modeling or steering mechanisms in order to provide more accuracy and robustness. To this end, recent advances in computer graphics and the use of GPUs have facilitated real-time or close to real-time implementation of even complex imaging algorithms. Techniques to directly integrate images pre- and/or intraoperatively with robotic systems are currently under investigation. They include approaches for image visualization, registration, navigation, and on-line image-based adaptation to deformations and interactions that occur throughout needle insertion.

Bibliography

[1] R.J. Webster III, J.S. Kim, N.J. Cowan, G.S. Chirikjian, and A.M. Okamura, "Non-holonomic Modeling of Needle Steering," *Int. J. Rob. Res.*, vol. 25, no. 5-6, pp. 509-525, 2006.

[2] S. Misra, K.J. Macura, K.T. Ramesha, and A.M. Okamura, "The Importance of Organ Geometry and Boundary Constraints for Planning of Medical Interventions," *Med. Eng. Phys.*, vol. 31, pp. 195-206, 2009.

[3] N. Abdolhassani, R.V. Patel, "Deflection of a Flexible Needle During Insertion into Soft Tissue," *In Proc. of 28th IEEE EMBS Annu. Int. Conf.*, USA, 2006, pp. 3858-3861.

[4] S. Misra, K.B. Reed, B.W. Schafer, K.T. Ramesh, and A.M. Okamura, "Observations and Models for Needle-Tissue Interactions," *In Proc. of IEEE Int. Conf. on Rob. Autom. (ICRA)*, Japan, 2009, pp. 2687-292.

[5] O. Goksel, E. Dehghan, and S.E. Salcudean, "Modeling and Simulation of Flexible Needles," *Med. Eng. Phys.*, vol. 31, pp. 1069-1078, 2009.

[6] S. Misra, K.B. Reed, B.W. Schafer, K.T. Ramesh, and A.M. Okamura, "Mechanics of Flexible Needles Robotically Steered through Soft Tissue," *Int. J. Rob. Res.*, vol. 29, 2010, pp. 1640-1660.

[7] R.J. Roesthuis, Y.R.J. van Veen, A. Jahya, and S. Misra, "Mechanics of Needle-Tissue Interaction," *In Proc. of IEEE/RSJ Int. Conf. on Intel. Rob. Sys. (IROS)*, 2011, pp. 2557-2563.

[8] D. Onck, "Reduction and Control for PDE Models of Manufacturing Systems," *Master Thesis*, Department of Mechanical Engineering Systems Engineering Group, Eindhoven University of Technology, 2006.

[9] D.G. Duffy, "Transform Methods for Solving Partial Differential Equations," Chapman and Hall/CRC; 2004 (second edition).

[10] S.S. Rao, Vibration of Continuous Systems, John Wiley and Sons Inc.; 2007.

[11] R. Alterovitz, A. Lim, K. Goldberg, G.S. Chirikjian, and A.M. Okamura, "Steering Flexible Needles under Markov Motion Uncertainty," *In Proc. of IEEE/RSJ Int. Conf. on Intel. Rob. Sys. (IROS)*, 2005, pp. 120-125.

[12] R. Alterovitz, M. Branicky, and K. Goldberg, "Motion Planning under Uncertainty for Image-Guided Medical Needle Steering," *Int. J. Rob. Res.*, vol. 27, no. 11-12, pp. 1361-1374, 2008.

[13] V. Kallem, N. Cowan, "Image-Guidance of Flexible Tip-Steerable Needles," *IEEE Trans. on Robotics*, vol. 25, no. 1, pp. 191-196, 2009.

[14] K.B. Reed, V. Kallem, R. Alterovitz, K. Goldberg, A.M. Okamura, and N.J. Cowan, "Integrated Planning and Image-Guided Control for Planar Needle Steering," *In Proc. of 2nd Biennial IEEE/RAS-EMBS Int. Conf. on Biomedical Robotics and Biomechatronics*, 2008, pp. 819-824.

[15] V. Duindam, J. Xu, R. Alterovitz, S. Sastry, and K. Goldberg, "Three-Dimensional Motion Planning Algorithms for Steerable Needles Using Inverse Kinematics," *Int. J. Rob. Res.*, vol. 29, pp. 789-800, 2010.

[16] M.C. Bernardes, B.V. Adorno, P. Poignet, N. Zemiti, and G.A. Borges, "Adaptive Path Planning for Steerable Needles Using Duty-Cycling," *In Proc. of IEEE/RSJ Int. Conf. on Intel. Rob. Sys. (IROS)*, USA, 2011, pp. 2545-2550.

[17] M.C. Bernardes, B.V. Adorno, P. Poignet, and G.A. Borges, "Semi-Automatic Needle Steering System with Robotic Manipulator," *In Proc. of IEEE Int. Conf. on Rob. Autom. (ICRA)*, 2012, pp. 1595-1600.

[18] N. Abolhassani, R.V. Patel, and F. Ayazi, "Minimization of Needle Deflection in Robot-Assisted Percutaneous Therapy," *Int. J. Med. Robotics Comput. Assist. Surg.*, vol. 3, pp. 140-148, 2007.

[19] R. Alterovitz, K. Goldberg, and A. Okamura, "Planning for Steerable Bevel-Tip Needle Insertion Through 2D Soft Tissue With Obstacles," *In Proc. of IEEE Int. Conf. on Rob. Autom. (ICRA)*, 2005, pp. 1640-1645.

[20] D. Minhas, J. Engh, M. Fenske, and C. Riviere, "Modeling of Needle Steering via Duty-Cycled Spinning," *In Proc. of 29th IEEE EMBS Annu. Int. Conf.*, France, 2007, pp. 2756-2759.

[21] N.A. Wood, K. Shahrour, M.C. Ost, and C.N. Riviere, "Needle Steering System Using Duty-Cycled Rotation for Percutaneous Kidney Access," *In Proc. of 32nd IEEE EMBS Annu. Int. Conf.*, 2010, pp. 5432-5435.

[22] J.P. Laumond, S. Sekhavat, and F. Lamiraux, "Guidelines in Nonholonomic Motion Planning for Mobile Robots, Robot Motion Planning and Control," *Lect. Notes Contr. Inf.*, vol. 229, pp. 1-53, Springer Berlin Heidelberg; 1998.

[23] S.S.Ge, Autonomous Mobile Robots: Sensing, Control, Decision Making and Applications, Taylor and Francis Group; 2006.

[24] P. Soueres, J.D. Boissonnat, "Optimal Trajectories for Nonholonomic Mobile Robots, Robot Motion Planning and Control," *Lect. Notes Contr. Inf.*, vol. 229, pp. 93-170, Springer Berlin Heidelberg; 1998.

[25] M. Krstic, A. Smyshlyaev, "Boundary Control of PDEs: A Course on Backstepping Designs," SIAM Advances in Design and Control; 2008.

Appendix A

Experimental Setup

Experimental implementations of the methodologies described in this thesis were carried out on a state-of-the-art robotic system which was designed and constructed in-house for the primary application of prostate brachytherapy.

The 5-DOF needle insertion manipulator shown in Fig. A.1 can perform orientation, insertion and rotation of the needle as well as linear motion of the stylet to drop radioactive seeds with an acceptable accuracy. It also maintains an RCM about the needle tip. The robot is controlled using a PID controller in joint space at a servo rate of 1kHz. In order to reduce noise perturbation that is dominant at low velocities which is the case in real interventions, a high-gain observer has been implemented to estimate velocity from encoder measurements. Fig. A.2 also shows the hardware block diagram and a general view of the full robotic system. A Nano43 6-DOF force/torque sensor (ATI Industrial Automation) is attached to the needle holder to measure the force signals acting on the needle shaft. High frequency content of the force/torque signal is eliminated by averaging its five recent samples using a moving average filter at the rate of 200Hz. The robotic system has been instrumented with an Aurora electromagnetic tracker (Northern Digital Inc.) that measures the position of its sensor coil(s) with respect to the device's global frame. An Aurora 5-DOF sensor coil is secured inside the needle shaft and very close to the tip in order to track the tip position at the rate of 40Hz.

Two desktop computers for control (client) and data capturing (server) have been interfaced through a User Datagram Protocol (UDP) connection over ethernet. A multi-threaded application for real-time position/velocity control, sensor readings, data logging and com-
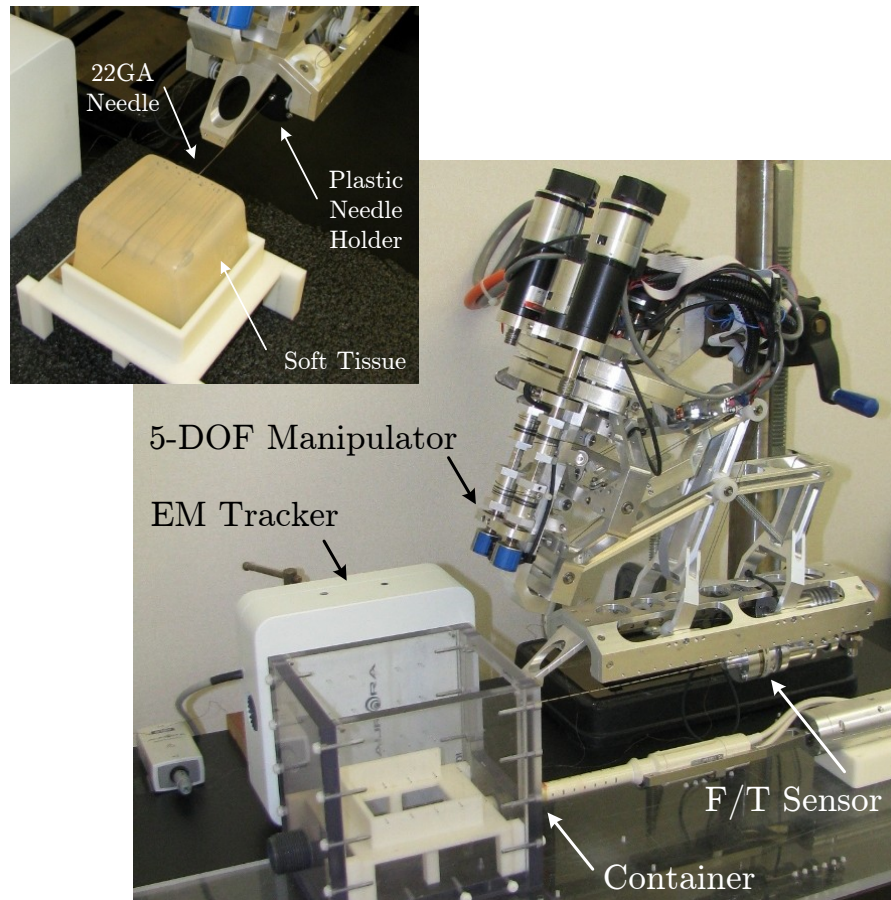
Figure A.1: A view of the needle insertion manipulator.

munication was developed using Microsoft® C++, MATLAB® and the QuaRC® Toolbox (Quanser Inc.). An Aloka SSD-1000 ultrasound system accompanied by an EPOS digital motion controller (Maxon Motor), and a PHANTOM Omni® haptic device (SensAble Technologies) are other available devices in the experimental system, and are employed for further developments.

Before using the robotic system, all hardware components are registered to a fixed coordinate frame. For this purpose, several approaches have been reported in the literature.
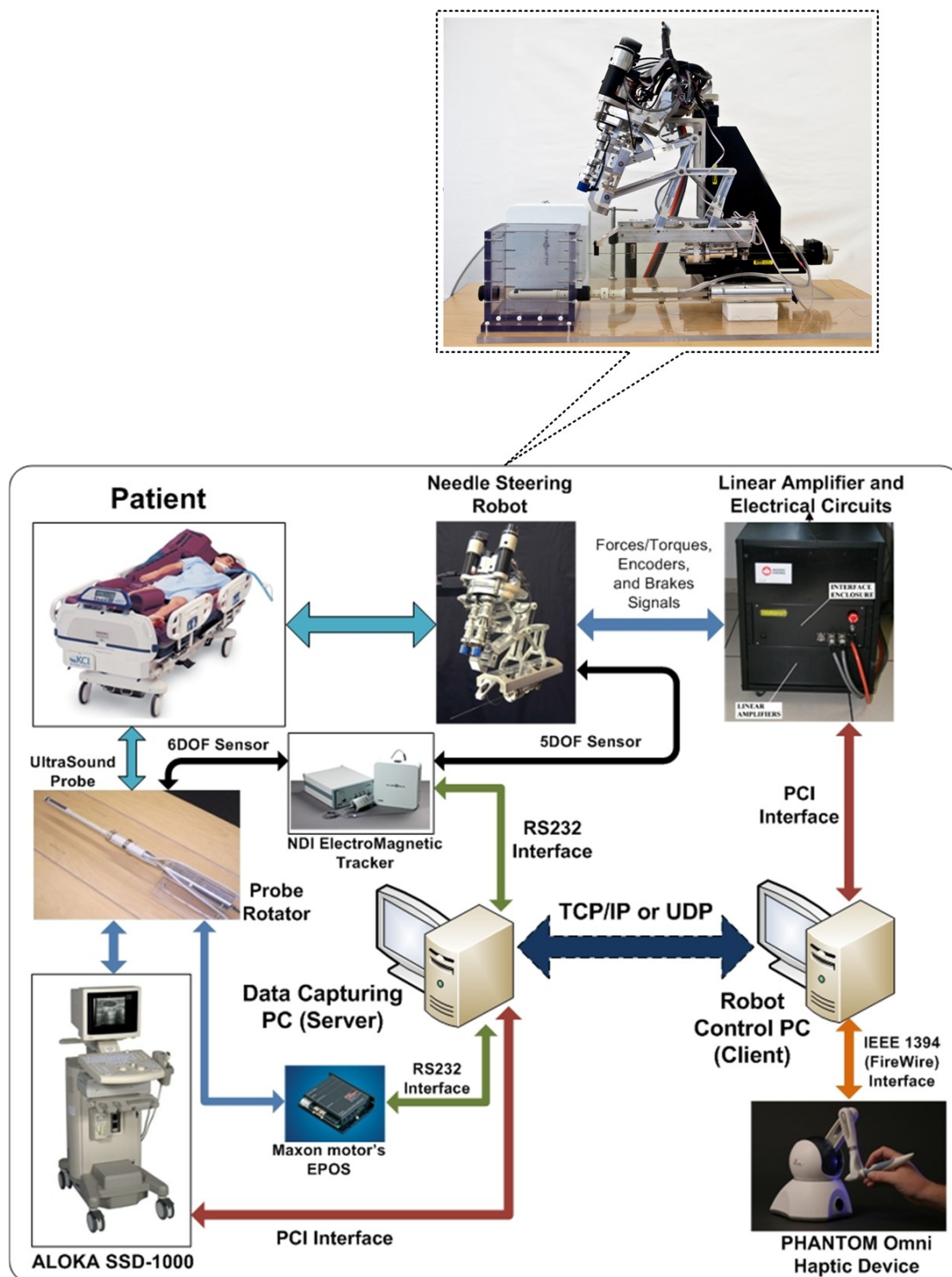
Figure A.2: Hardware block diagram of the robotic system and a view of the 5-DOF manipulator.

Appendix B

Reprint Permissions

Subject: print permission
From: Ali Asadian
Sent: Friday, February 01, 2013 4:24 PM
To: Magic Admin
Subject: Contact Varian: print permission Cancer treatment facility:
Country: Canada

I am a PhD student in Western University (The University of Western Ontario) in Canada. For my PhD dissertation, I have found a nice image about dosimetry planning in prostate cancer on the web with your affiliation. I, hereby, ask for permission to copy this figures in my PhD thesis and give reference to your website. I took the image from the following link.

http://www.varian.com/us/oncology/brachytherapy/treatment-planning-systems.html#.UQwtZx2Zkrp

Thanks.

Sincerely,

Ali Asadian,
* PhD Student, Western University (The University of Western Ontario)
** NSERC CREATE Scholar in Computer-Assisted Medical Intervention [CAMI]
Canadian Surgical Technologies and Advanced Robotics [CSTAR]
Lawson Health Research Institute, University Hospital

Ali, thanks for your interest in Varian Brachytherapy. For use of Varian images, please review the following legal notice:

Use of VARIAN Visual Materials

The Varian Medical Systems ("VARIAN") Visual Materials (individually and collectively, "Visual Materials") may consist of Microsoft Office PowerPoint(r) documents, animation clips, video clips, graphic representations, images and the like and are a valuable business assets and these terms are intended to protect them.

By downloading and/or using the VARIAN Visual Materials, you acknowledge the rights of VARIAN in its Visual Materials, that you have read and understood these terms, and that you agree to comply with these guidelines in using the VARIAN Visual Materials.

In consideration of VARIAN permitting you to use the Visual Materials, you agree to comply with the terms described herein. VARIAN gives you the personal, non-transferable, revocable right to use the Visual Materials provided herein only in connection with your Radiation Therapy practice and will not use these Visual Materials in any activity that might in any way hurt the VARIAN reputation. You agree not to use the Images in any manner that would deceive or mislead the public, including as to sponsorship or affiliation. Any goodwill accruing to any VARIAN trademark by virtue of your use of the Images shall inure to the benefit of VARIAN.

VARIAN does not warrant that the marketing materials comply with local law, regulations or policy.

You will use the following language as a credit and notice:

Varian Medical Systems, Inc. All rights reserved.

Should VARIAN ask you to stop using these Visual Materials or to change that use in any way, you agree to comply with that request.

These terms and your use of the VARIAN Visual Materials do not constitute a partnership, joint venture, or agency relationship between you and VARIAN. This is the only agreement between you and VARIAN concerning the VARIAN Visual Materials, and it may not be changed except by a signed written agreement.

If you have any questions or any proposed use that is not covered by these guidelines, please contact the VARIAN Marketing Department. VARIAN may change these guidelines at any time without prior notice, and may for any reason whatsoever withdraw this permission.

This is a License Agreement between ali asadian ("You") and Elsevier ("Elsevier") provided by Copyright Clearance Center ("CCC"). The license consists of your order details, the terms and conditions provided by Elsevier, and the payment terms and conditions.

All payments must be made in full to CCC. For payment instructions, please see information listed at the bottom of this form.

Supplier	Elsevier Limited The Boulevard,Langford Lane Kidlington,Oxford,OX5 1GB,UK
Registered Company Number	1982084
Customer name	ali asadian
Customer address	CSTAR, London, ON N6A 5A5
License number	3107630229593
License date	Mar 14, 2013
Licensed content publisher	Elsevier
Licensed content publication	Medical Image Analysis
Licensed content title	Robotic assistance for ultrasound-guided prostate brachytherapy
Licensed content author	Gabor Fichtinger,Jonathan P. Fiene,Christopher W. Kennedy,Gernot Kronreif,Iulian Iordachita,Danny Y. Song,Everette C. Burdette,Peter Kazanzides
Licensed content date	October 2008
Licensed content volume number	12
Licensed content issue number	5
Number of pages	11
Start Page	535
End Page	545
Type of Use	reuse in a thesis/dissertation
Intended publisher of new work	other
Portion	figures/tables/illustrations
Number of figures/tables/illustrations	2

INTRODUCTION

1. The publisher for this copyrighted material is Elsevier. By clicking "accept" in connection with completing this licensing transaction, you agree that the following terms and conditions apply to this transaction (along with the Billing and Payment terms and conditions established by Copyright Clearance Center, Inc. ("CCC"), at the time that you opened your Rightslink account and that are available at any time at http://myaccount.copyright.com).

GENERAL TERMS

2. Elsevier hereby grants you permission to reproduce the aforementioned material subject to the terms and conditions indicated.

3. Acknowledgement: If any part of the material to be used (for example, figures) has appeared in our publication with credit or acknowledgement to another source, permission must also be sought from that source. If such permission is not obtained then that material may not be included in your publication/copies. Suitable acknowledgement to the source must be made, either as a footnote or in a reference list at the end of your publication, as follows:

"Reprinted from Publication title, Vol /edition number, Author(s), Title of article / title of chapter, Pages No., Copyright (Year), with permission from Elsevier [OR APPLICABLE SOCIETY COPYRIGHT OWNER]." Also Lancet special credit - "Reprinted from The Lancet, Vol. number, Author(s), Title of article, Pages No., Copyright (Year), with permission from Elsevier."

4. Reproduction of this material is confined to the purpose and/or media for which permission is hereby given.

5. Altering/Modifying Material: Not Permitted. However figures and illustrations may be altered/adapted minimally to serve your work. Any other abbreviations, additions, deletions and/or any other alterations shall be made only with prior written authorization of Elsevier Ltd. (Please

contact Elsevier at permissions@elsevier.com)

6. If the permission fee for the requested use of our material is waived in this instance, please be advised that your future requests for Elsevier materials may attract a fee.

7. Reservation of Rights: Publisher reserves all rights not specifically granted in the combination of (i) the license details provided by you and accepted in the course of this licensing transaction, (ii) these terms and conditions and (iii) CCC's Billing and Payment terms and conditions.

8. License Contingent Upon Payment: While you may exercise the rights licensed immediately upon issuance of the license at the end of the licensing process for the transaction, provided that you have disclosed complete and accurate details of your proposed use, no license is finally effective unless and until full payment is received from you (either by publisher or by CCC) as provided in CCC's Billing and Payment terms and conditions. If full payment is not received on a timely basis, then any license preliminarily granted shall be deemed automatically revoked and shall be void as if never granted. Further, in the event that you breach any of these terms and conditions or any of CCC's Billing and Payment terms and conditions, the license is automatically revoked and shall be void as if never granted. Use of materials as described in a revoked license, as well as any use of the materials beyond the scope of an unrevoked license, may constitute copyright infringement and publisher reserves the right to take any and all action to protect its copyright in the materials.

9. Warranties: Publisher makes no representations or warranties with respect to the licensed material.

10. Indemnity: You hereby indemnify and agree to hold harmless publisher and CCC, and their respective officers, directors, employees and agents, from and against any and all claims arising out of your use of the licensed material other than as specifically authorized pursuant to this license.

11. No Transfer of License: This license is personal to you and may not be sublicensed, assigned, or transferred by you to any other person without publisher's written permission.

12. No Amendment Except in Writing: This license may not be amended except in a writing signed by both parties (or, in the case of publisher, by CCC on publisher's behalf).

13. Objection to Contrary Terms: Publisher hereby objects to any terms contained in any purchase order, acknowledgment, check endorsement or other writing prepared by you, which terms are inconsistent with these terms and conditions or CCC's Billing and Payment terms and conditions. These terms and conditions, together with CCC's Billing and Payment terms and conditions (which are incorporated herein), comprise the entire agreement between you and publisher (and CCC) concerning this licensing transaction. In the event of any conflict between your obligations established by these terms and conditions and those established by CCC's Billing and Payment terms and conditions, these terms and conditions shall control.

14. Revocation: Elsevier or Copyright Clearance Center may deny the permissions described in this License at their sole discretion, for any reason or no reason, with a full refund payable to you. Notice of such denial will be made using the contact information provided by you. Failure to receive such notice will not alter or invalidate the denial. In no event will Elsevier or Copyright

Clearance Center be responsible or liable for any costs, expenses or damage incurred by you as a result of a denial of your permission request, other than a refund of the amount(s) paid by you to Elsevier and/or Copyright Clearance Center for denied permissions.

LIMITED LICENSE

The following terms and conditions apply only to specific license types:

15. **Translation**: This permission is granted for non-exclusive world **English** rights only unless your license was granted for translation rights. If you licensed translation rights you may only translate this content into the languages you requested. A professional translator must perform all translations and reproduce the content word for word preserving the integrity of the article. If this license is to re-use 1 or 2 figures then permission is granted for non-exclusive world rights in all languages.

16. **Website**: The following terms and conditions apply to electronic reserve and author websites:
Electronic reserve: If licensed material is to be posted to website, the web site is to be password-protected and made available only to bona fide students registered on a relevant course if:
This license was made in connection with a course,
This permission is granted for 1 year only. You may obtain a license for future website posting,
All content posted to the web site must maintain the copyright information line on the bottom of each image,
A hyper-text must be included to the Homepage of the journal from which you are licensing at http://www.sciencedirect.com/science/journal/xxxxx or the Elsevier homepage for books at http://www.elsevier.com , and
Central Storage: This license does not include permission for a scanned version of the material to be stored in a central repository such as that provided by Heron/XanEdu.

17. **Author website** for journals with the following additional clauses:

All content posted to the web site must maintain the copyright information line on the bottom of each image, and the permission granted is limited to the personal version of your paper. You are not allowed to download and post the published electronic version of your article (whether PDF or HTML, proof or final version), nor may you scan the printed edition to create an electronic version. A hyper-text must be included to the Homepage of the journal from which you are licensing at http://www.sciencedirect.com/science/journal/xxxxx . As part of our normal production process, you will receive an e-mail notice when your article appears on Elsevier's online service ScienceDirect (www.sciencedirect.com). That e-mail will include the article's Digital Object Identifier (DOI). This number provides the electronic link to the published article and should be included in the posting of your personal version. We ask that you wait until you receive this e-mail and have the DOI to do any posting.

Central Storage: This license does not include permission for a scanned version of the material to be stored in a central repository such as that provided by Heron/XanEdu.

18. **Author website** for books with the following additional clauses:

SPRINGER LICENSE
TERMS AND CONDITIONS

Feb 28, 2013

This is a License Agreement between ali asadian ("You") and Springer ("Springer") provided by Copyright Clearance Center ("CCC"). The license consists of your order details, the terms and conditions provided by Springer, and the payment terms and conditions.

All payments must be made in full to CCC. For payment instructions, please see information listed at the bottom of this form.

License Number	3097820792013
License date	Feb 28, 2013
Licensed content publisher	Springer
Licensed content publication	Journal of Intelligent and Robotic Systems
Licensed content title	Robot-Assisted Needle Steering Using a Control Theoretic Approach
Licensed content author	Ali Asadian
Licensed content date	Jan 1, 2010
Volume number	62
Issue number	3
Type of Use	Thesis/Dissertation
Portion	Full text
Number of copies	1
Author of this Springer article	Yes and you are the sole author of the new work
Order reference number	
Title of your thesis / dissertation	Robotics-Assisted Needle Steering with Application in Percutaneous Therapies and Biopsies
Expected completion date	Mar 2013
Estimated size(pages)	180
Total	0.00 CAD

Terms and Conditions

Introduction
The publisher for this copyrighted material is Springer Science + Business Media. By clicking "accept" in connection with completing this licensing transaction, you agree that the following terms and conditions apply to this transaction (along with the Billing and Payment terms and conditions established by Copyright Clearance Center, Inc. ("CCC"), at the time that you opened your Rightslink account and that are available at any time at http://myaccount.copyright.com).

Example 2: Springer Science + Business Media makes no representations or warranties with respect to the licensed material and adopts on its own behalf the limitations and disclaimers established by CCC on its behalf in its Billing and Payment terms and conditions for this licensing transaction.

Indemnity
You hereby indemnify and agree to hold harmless Springer Science + Business Media and CCC, and their respective officers, directors, employees and agents, from and against any and all claims arising out of your use of the licensed material other than as specifically authorized pursuant to this license.

No Transfer of License
This license is personal to you and may not be sublicensed, assigned, or transferred by you to any other person without Springer Science + Business Media's written permission.

No Amendment Except in Writing
This license may not be amended except in a writing signed by both parties (or, in the case of Springer Science + Business Media, by CCC on Springer Science + Business Media's behalf).

Objection to Contrary Terms
Springer Science + Business Media hereby objects to any terms contained in any purchase order, acknowledgment, check endorsement or other writing prepared by you, which terms are inconsistent with these terms and conditions or CCC's Billing and Payment terms and conditions. These terms and conditions, together with CCC's Billing and Payment terms and conditions (which are incorporated herein), comprise the entire agreement between you and Springer Science + Business Media (and CCC) concerning this licensing transaction. In the event of any conflict between your obligations established by these terms and conditions and those established by CCC's Billing and Payment terms and conditions, these terms and conditions shall control.

Jurisdiction
All disputes that may arise in connection with this present License, or the breach thereof, shall be settled exclusively by arbitration, to be held in The Netherlands, in accordance with Dutch law, and to be conducted under the Rules of the 'Netherlands Arbitrage Instituut' (Netherlands Institute of Arbitration).**OR:**

All disputes that may arise in connection with this present License, or the breach thereof, shall be settled exclusively by arbitration, to be held in the Federal Republic of Germany, in accordance with German law.

Other terms and conditions:

v1.3

If you would like to pay for this license now, please remit this license along with your payment made payable to "COPYRIGHT CLEARANCE CENTER" otherwise you will be invoiced within 48 hours of the license date. Payment should be in the form of a check or money order referencing your account number and this invoice number RLNK500967440. Once you receive your invoice for this order, you may pay your invoice by credit card.

Please follow instructions provided at that time.

Make Payment To:
Copyright Clearance Center
Dept 001
P.O. Box 843006
Boston, MA 02284-3006

For suggestions or comments regarding this order, contact RightsLink Customer Support: <u>customercare@copyright.com</u> or +1-877-622-5543 (toll free in the US) or +1-978-646-2777.

Gratis licenses (referencing $0 in the Total field) are free. Please retain this printable license for your reference. No payment is required.

CURRICULUM VITAE

ALI   ASADIAN

EDUCATION

2008-2013   **Western University (The University of Western Ontario)**

Ph.D. in Electrical Engineering   **London, Canada**

Thesis Title: Robotics-Assisted Needle Steering for Percutaneous Interventions: Modeling and Experiments

Advisors: Dr. R.V. Patel and Dr. M.R. Kermani

2002-2005   **University of Tehran**

M.Sc. in Electrical Engineering (Control Systems)   **Tehran, Iran**

Thesis Title: Assessment of Conventional and Intelligent Data Fusion Approaches in a Land Navigation System

Advisors: Dr. B. Moshiri and Dr. A. Khaki-Sedigh

1997-2002   **Sharif University of Technology**

B.Sc. in Electrical Engineering (Control Systems)   **Tehran, Iran**

Project Title: Identification and Control of a PMDC Motor at Very Low Velocities: Design and Implementation

Advisor: Dr. M. Haeri

HONORS AND AWARDS

- Best Presentation Award in Control and Robotics Division, ECE Annual Graduate Symposium, Western University, 2012.

- Ontario Graduate Scholarship (OGS), 15,000CAD$ per annum, 2011-2012, 2012-2013.

- Western Graduate Thesis Research Award (GTRA), 2012.

- NSERC CREATE Program Supplementary Funding, 10,000CAD$ per annum, 2010-2012.

- Western Graduate Research Scholarship (WGRS), 10,500CAD$ per annum, 2008-2012.

- Ranked 1st in the province and ranked 72nd among 250,000 high school attendants in nation-wide university entrance exam for undergraduate education (Iran's Ministry of Science, Research and Technology), 1997.

JOURNAL PAPERS

- **Ali Asadian**, Rajni V. Patel, and Mehrdad R. Kermani, "Dynamics of Translational Friction in Needle-Tissue Interaction During Needle Insertion," *Submitted to the the Annals in Biomedical Engineering (Springer Verlag)*, 2013.

- **Ali Asadian**, Mehrdad R. Kermani, and Rajni V. Patel, "A Novel Force Modeling Scheme for Needle Insertion Using Multiple Kalman Filters," IEEE Transactions on Instrumentation and Measurement, vol. 61, no. 2, 2012, pp. 429-438.

- **Ali Asadian**, Mehrdad R. Kermani, and Rajni V. Patel, "Robot-Assisted Needle Steering Using a Control Theoretic Approach," Journal of Intelligent and Robotic Systems (Springer Verlag), vol. 62, no. 3-4, 2011, pp. 397-418.

- **Ali Asadian**, Rajni V. Patel, and Mehrdad R. Kermani, "Curvature Control of Flexible Bevel-Tip Needles via a Time-Varying Insertion Rate," *Under Preparation*.

REFEREED CONFERENCE PAPERS (* indicates presentation by Ali Asadian)

- Ran Xu, **Ali Asadian**, Anish Naidu, and Rajni V. Patel, "Position Control of Concentric-Tube Continuum Robots Using a Modified Jacobian-Based Approach," *Accepted for Presentation in IEEE Int. Conf. on Robotics and Automation (ICRA)*, Germany, 2013.

- **Ali Asadian***, Rajni V. Patel, and Mehrdad R. Kermani, "Compensation for Relative Velocity between Needle and Soft Tissue for Friction Modeling in Needle Insertion," In Proc. of the 34th Annual Int. Conf. of IEEE Engineering in Medicine and Biology Society (EMBS), pp. 960-963, USA, 2012.

- **Ali Asadian***, Mehrdad R. Kermani, and Rajni V. Patel, "An Analytical Model for Deflection of Flexible Needles During Needle Insertion," In Proc. of IEEE/RSJ Int. Conf. on Intelligent Robots and Systems (IROS), pp. 2551-2556, USA, 2011.

- **Ali Asadian**, Rajni V. Patel, and Mehrdad R. Kermani, "A Distributed Model for Needle-Tissue Friction in Percutaneous Interventions," In Proc. of IEEE Int. Conf. on Robotics and Automation (ICRA), pp. 1896-1901, China, 2011.

- **Ali Asadian**, Mehrdad R. Kermani, and Rajni V. Patel, "A Compact Dynamic Force Model for Needle-Tissue Interaction," In Proc. of the 32nd Annual Int. Conf. of IEEE Engineering in Medicine and Biology Society (EMBS), pp. 2292-2295, Argentina, 2010.

- **Ali Asadian**[*], Mehrdad R. Kermani, and Rajni V. Patel, "Accelerated Needle Steering Using Partitioned Value Iteration," In Proc. of IEEE American Control Conf. (ACC), pp. 2785-2790, USA, 2010.

- **Ali Asadian**[*], Behzad Moshiri, and Javad Rezaie, "Robustness Assessment of Intelligent Information Fusion Techniques in Navigation Systems Encountering Satellite Outage," In Proc. of the 4th IEEE Conf. on Innovations in Information Technology (IIT), pp. 46-50, UAE, 2007.

- Javad Rezaie, Behzad Moshiri, Babak N. Araabi, and **Ali Asadian**, "GPS/INS Integration Using Nonlinear Blending Filters," In Proc. of IEEE SICE Annual Conf. 2007, pp. 1674-1680, Japan, 2007.

- **Ali Asadian**, Behzad Moshiri, and Ali K. Sedigh, "A Novel Data Fusion Approach in an Integrated GPS/INS System Using Adaptive Fuzzy Particle Filters," In Proc. of the 5th IEEE Conf. on Technology and Automation (ICTA), pp. 125-130, Greece, 2005.

- **Ali Asadian**, Behzad Moshiri, Ali K. Sedigh, and Caro Lucas, "GA-based Data Fusion Approach in an Intelligent Integrated GPS/INS System," In Proc. of IFAC/AAAI Int. Conf. on Informatics on Control, Automation and Robotics (ICINCO), vol. 1, pp. 216-221, Spain, 2005.

- **Ali Asadian**, Behzad Moshiri, Ali K. Sedigh, and Caro Lucas, "Optimized Data Fusion in an Intelligent Integrated GPS/INS System Using Genetic Algorithm," In Proc. of Int. Conf. of Artificial Intelligence and Computer Science, vol. 5, pp. 221-224, Turkey, 2005.

TALKS

- "Needle-Tissue Interaction and Deflection Modeling of Flexible Needles in Needle Insertion," Workshop on Pathways to Clinical Needle Steering: Recent Advances and Future Applications, IEEE International Conference on Robotics and Automation (ICRA), St. Paul, USA, May 2012.

- "Dynamic Modeling of Distributed Friction in Needle-Tissue Interaction with Applications to Needle Steering," 4th Semi-Annual Workshop on Control Systems, Concordia University, Canada, April 2011.

SCIENTIFIC REVIEWS AND ACTIVITIES

- Reviewer of IEEE Transactions on Biomedical Engineering, 2011-2013.

- Reviewer of Journal of Intelligent and Robotic Systems (Springer Verlag), 2011-2013.

- Reviewer of Medical Physics, 2012.

- Reviewer of IEEE Transactions on Instrumentation and Measurement, 2010-2012.

- Reviewer of IEEE Engineering in Medicine and Biology Society (EMBS), 2010-2013.

- Reviewer of IEEE International Conference on Robotics and Automation (ICRA), 2011, 2013.

- Reviewer of IEEE/RSJ International Conference on Intelligent Robots and Systems (IROS), 2011, 2012.

- Reviewer of Medical Engineering and Physics (Elsevier), 2011.

- Reviewer of the 4th, 5th and 6th Canadian Student Conference on Biomedical Computing and Engineering (CSCBCE), Canada, 2009-2011.

- Member of Organizing Committee (*Vice Chair of Industry and Applications*)/Session Chair and Reviewer of the 9th Iranian Student Conference on Electrical Engineering (ISCEE), University of Tehran, Tehran, Iran, September 2006.

- Reviewer of World Academy of Science, Engineering and Technology (WASET), IEEE Vehicular Technology Conference, IEEE Innovations in Information Technology, IEEE Symposium on Mechatronics and its Applications, and several other conferences, 2005-2008.

PROFESSIONAL WORK EXPERIENCES

2008-2013   **Canadian Surgical Technologies and Advanced Robotics**

Position: **Research Assistant**   **London, Canada**

2005-2007   **TurnUp Pardazesh Engineering Company**

Position: **Design Engineer**   **Tehran, Iran**

2003-2004   **Mahsar Abnieh Industries Group**

Position: **Control and Automation Engineer**   **Tehran, Iran**

TEACHING EXPERIENCES

2008-2013   **Western University**

Position: **Teaching Assistant**   **London, Canada**

2003-2007   **University of Tehran**

Position: **Lab Assistant/Instructor/Teaching Assistant**   **Tehran, Iran**